**The Role of Microstructural Variability on the Very High Cycle Fatigue Lifetime Variability of the $\alpha + \beta$ Titanium Alloy, Ti-6Al-2Sn-4Zr-6Mo**

**by**

**Christopher J. Szczepanski**

A dissertation submitted in partial fulfillment
of the requirements for the degree of
Doctor of Philosophy
(Materials Science and Engineering)
in The University of Michigan
2008

Doctoral Committee:

Professor J. Wayne Jones, Chair
Professor Tresa M. Pollock
Professor Jwo Pan
Dr. James M. Larsen, Air Force Research Laboratory

# DEDICATION

*To Mom, Dad, Matt, and Anna.*

# ACKNOWLEDGEMENTS

The list of those who have inspired, supported and advised me through my educational journey is substantial. The support of family and friends spans the spectrum of those who have contributed technical advice to those who have graciously lent an ear or appropriate words of encouragement at a critical time. I am indebted to all those who have enriched my life by giving of themselves.

Firstly, I must thank my advisor, Professor Wayne Jones for his technical insight and guidance, without which this thesis would not have been possible. Furthermore, and perhaps more importantly, I appreciate his patience and enduring support throughout the past few years in helping me to develop as a researcher. I would also like to thank the other members of my thesis committee for enriching my education both in the classroom and in my research. I appreciate the support of Professor Tresa Pollock for her advice and her habit of asking guiding questions which have helped to define various aspects of this thesis. Thanks to Dr. James Larsen, whose true passion for materials research is infectious and whose ability to see the "big picture" have helped ensure this thesis maintained a practical aspect. I would like to thank Professor Jwo Pan, who was able to bring a unique perspective through his suggestions and insightful questions along the way.

In addition to my committee, I have benefitted tremendously from the interactions with numerous people within the Jones and Pollock research groups and across the University. Like the graduate students that have preceded me, I too feel tremendously indebted to Mr.

Chris Torbet for all of his assistance and guidance with experimental equipment in this thesis. His knack for developing creative solutions to experimental obstacles has both expedited this work and led to the acquisition of otherwise unattainable results. I would like to thank my office mates, Jon Madison, Jiashi Miao, and Nick Saddock for their contributions of personal support and suggestions in technical matters. I have enjoyed our time together and look forward to continuing relationships with all of you in both personal and professional capacities for many years to come. To all of the many graduate students and post-doctoral researchers that have passed through the Pollock and Jones groups over the past few years, I extend my appreciation for enriching my experience.

I have had the good fortune of spending a portion of my graduate studies at the Air Force Research Laboratory. It has been a great experience to work with a number of truly exceptional researchers and their advice and experimental support has substantially enhanced the quality of this thesis. Specifically, I would like to acknowledge the contributions of Dr. Sushant Jha, who has been both an excellent resource on research issues and has become a close friend in helping to ease my transition to Dayton. I am also deeply appreciative of the support of Dr. Mike Caton, Dr. Andy Rosenberger, and others within the Behavior and Life Prediction section for their assistance with technical matters and their hospitality.

Funding for this project was provided through the Air Force Office of Scientific Research Metallic Materials Program (Project # F49620-03-1 -0069). Additional funding was provided through the STEP program at the AFRL Materials and Manufacturing Directorate.

# TABLE OF CONTENTS

# LIST OF TABLES

# LIST OF FIGURES

# ABSTRACT

The fatigue behavior of structural components in the regime of very high cycle fatigue (VHCF) ($10^6$ – $10^9$ cycles) has been attracting increased commercial interest as components are increasingly being called upon to perform in this regime of lifetimes. In VHCF, the applied stresses relative to the yield stress are very low. Therefore, it is presumed that a substantial portion of fatigue lifetime is consumed by the fatigue crack initiation process, and that cyclic plasticity only accumulates in microstructural neighborhoods that are susceptible to fatigue damage accumulation. Thus, microstructural heterogeneity is believed to significantly effect the fatigue lifetime variability.

The very high cycle fatigue behavior of Ti-6246 has been investigated using ultrasonic fatigue techniques, and lifetimes ranging from $10^6 - 10^9$ cycles have been observed. Fatigue cracks initiate by facet formation within $\alpha_p$ grains. It has been found that the facets form in grains that are slightly larger than average and that the facets appear to form by a process of slip since the facet plane normals are oriented approximately 35-55° with respect to the tensile axis. Three characteristic fatigue crack initiation sites have been identified. These initiation sites, ranked in order of increasing fatigue resistance are: surface, subsurface with isolated facets, and subsurface with contiguous transgranular faceting. The texture of the material in these initiation regions is favorable for basal and prism slip. This texture is derived from the prior $\beta$ texture, and a mechanism of fatigue crack initiation resulting from strain incompatibility has been proposed.

Fatigue crack growth experiments have been completed to measure the influence of local texture on the ease of fatigue crack initiation and the resulting fatigue crack growth rates. These experiments have found that the controlling microstructural dimension is on the order of 20-25$\mu$m. The texture appears to affect initiation of fatigue cracks from notches as well. For notches placed within neighborhoods favorably oriented for basal slip, fatigue crack initiation will be encouraged. However, for notches placed within microstructural regions unfavorably oriented for basal slip, fatigue crack initiation will be inhibited.

# Chapter 1

# Introduction

## *1.1 Background and Objectives*

As the systems-level reliability of transportation and power generation systems continues to improve, components are being driven to the limits of material performance capabilities. As a result, the fatigue behavior of components such as automobile cylinder heads, engine blocks, and turbine engine components in the fatigue regime of $10^6 - 10^9$ cycles is a major design criterion. Therefore, the successful application of safe-life design practices requires the understanding of fatigue behavior in the regime of high cycle (HCF) and very high cycle fatigue (VHCF), with the lifetimes in these regimes being defined as $10^5 - 10^7$, and $10^7 - 10^9$ cycles, respectively.

Additional motivation to develop more accurate understanding of the VHCF behavior of components comes from fleet maintenance and sustainment concerns. The US Air Force, for example, owns approximately 20,000 turbine engines, and the maintenance and sustainment of this fleet consumes a substantial portion of their multi-billion dollar annual budget. Many of these aircraft are already operating beyond their designed lifetimes due to the reduction in aircraft acquisitions over the past 15-20 years. By some estimates, [1] outright replacement of these aircraft would cost somewhere in the range of $300 billion, which is not a feasible sustainment plan. Therefore, for safe-life extension of these legacy components, more accurate models of material behavior in the VHCF regime are needed.

These two examples are representative of a larger number of cases throughout the transportation and power generation sectors in which components are expected to remain in service into the very high cycle fatigue regime, either by design or through safe life extension practices. In this regime of fatigue behavior, the scatter in lifetimes can be substantial. If one considers the fatigue lifetimes of a number of specimens as a distribution rather than a deterministic value, the resulting retirement practice shown in Figure 1.1 schematically illustrates the statistically unused lifetimes. The current lifing approach used by the Air Force for fracture critical turbine engine components is to retire components at the point where the probability of failure is equal to 0.1%. For example, in the case where lifetimes range from $10^6 - 10^9$ cycles, all components would be retired after approximately $10^6$ cycles. Aerospace turbine engine manufacturers use similar approaches in which probabilities of failure are fit to experimental data and extrapolated to acceptably low risk levels such as -3$\sigma$. Thus, the components that would have survived for $10^9$ cycles have been retired very early relative to their full safe life potential as illustrated in the probability of failure plot in Figure 1.1, which is applicable to low cycle fatigue (LCF) behavior. The Department of Defense has also outlined guiding principles that are to be employed in testing and validation of fracture critical structural engine components with the handbook on the Engine Structural Integrity Program (ENSIP) [2]. This handbook provides distinctions between low and high cycle fatigue behavior and has separate guidelines for lifing components in each of these regimes of fatigue behavior. Further, this handbook stipulates that fatigue testing should be completed for lifetimes as long as $10^9$ cycles to accurately life these components. From these motivations, there is a practical desire to understand the HCF and VHCF behavior of these structural materials.

In the VHCF regime, the applied loads are nominally elastic, and cyclic damage accumulation is presumed to occur only in localized areas where the microstructural neighborhood is suitable for fatigue crack initiation. For materials free of inclusions or porosity, the

fatigue crack initiation process is believed to be controlled by the distribution of fatigue critical microstructures or so-called "hot spots" [3] in which damage may accumulate. In other words, microstructure can be modeled as a distribution as shown in Figure 1.2 where microstructural feature can refer to grain size, clustering, crystallographic orientation, etc. These fatigue critical regions will be distributed throughout structural components, due to the natural variability resulting from thermomechanical processing. Thus, given nominally elastic loading, under the lower nominal stresses associated with very long life fatigue, microstructural variability is expected to be an important influence on fatigue lifetime variability. As noted [4] in the literature, the majority of fatigue lifetime in the regime of VHCF is spent in the process of fatigue crack initiation. Given the inherent variability in fatigue damage accumulation processes, it is more appropriate to think of fatigue crack initiation lifetime as a distribution rather than as a deterministic quantity. Therefore, many specimens must be tested at every stress level of interest to characterize this lifetime distribution and the characteristics of the microstructural neighborhoods associated with fatigue crack initiation.

After a crack has initiated, it will begin to propagate as a small fatigue crack, which is known to be a microstructurally sensitive process. Thus, the effect of microstructure on the small fatigue crack growth behavior must be considered separately from the effect of microstructure on the fatigue crack initiation process, as the damage accumulation mechanisms will differ.

Through characterization of the fatigue crack initiating regions, it is possible to identify and quantify the microstructural configurations responsible for fatigue crack initiation. These microstructural "hot spots" observed at the crack initiation site can be used as a means for determining the mechanism of fatigue crack initiation and ranking the severity of these individual regions.

The objectives of this thesis are to:

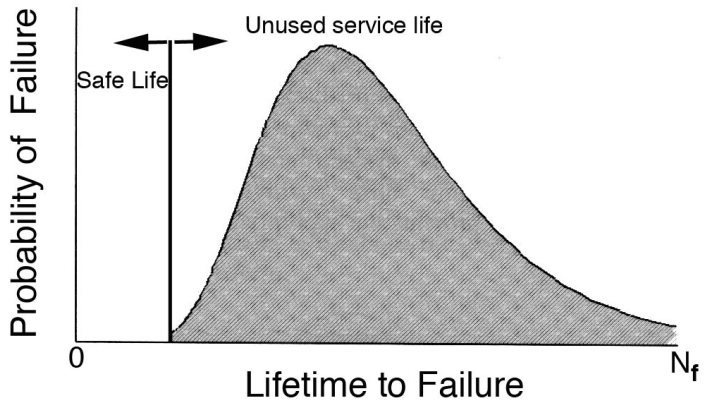


**Figure 1.1:** This schematic illustrates the statistically unused service lifetimes of fracture critical turbine engine components under current lifing practices. After [1].

1.) Characterize the VHCF behavior of the $\alpha + \beta$ titanium alloy, Ti-6Al-2Sn-4Zr-6Mo.

2.) Identify the microstructural features responsible for damage accumulation and determine the mechanisms of fatigue failure on fatigue crack intitiation.

3.) Determine the effect of the distribution in microstructure on small fatigue crack growth.

4.) Compare the prevalence of fatigue critical microstructural regions to those found in the nominal microstructure.

## *1.2 Approach*

The nature of the current research is dependent on characterizing the distribution of fatigue lifetimes as a result of microstructural variability, and as a result, a number of repeat tests must be performed to generate statistically representative lifetime distributions at the stress levels of interest. Ultrasonic fatigue techniques allow researchers to rapidly accumulate fatigue lifetime data in the long lifetime regime of fatigue. S-N type fatigue tests have been conducted using ultrasonic frequency (20 kHz) techniques in the range of 0.4-0.6 $\sigma_{YS}$ at a stress ratio of 0.05 at room temperature in lab air.

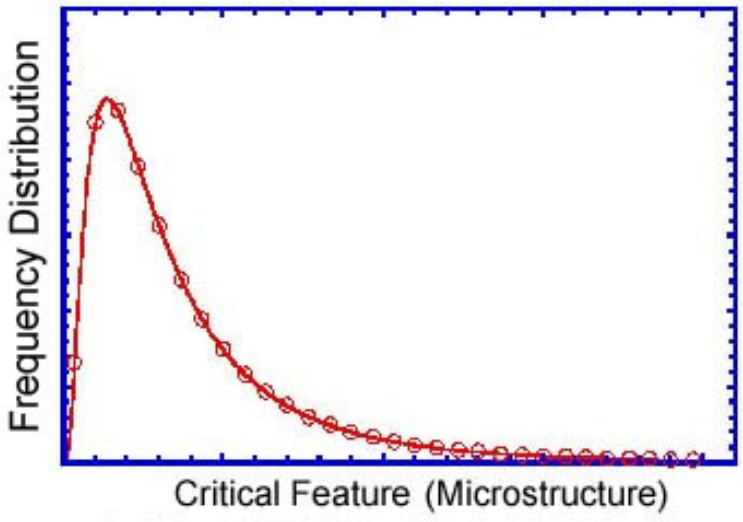


**Figure 1.2:** This chart schematically illustrates the distribution of a given microstructural feature.

A majority of the experimental efforts in the current investigation have focused on characterization of the regions of material near the fatigue crack initiation site to develop an understanding of the mechanism of fatigue crack initiation. Fractographic analysis has been completed on these specimens to quantify the features observed at the site of fatigue crack initiation and to determine if microstructural "hot spots" responsible for fatigue crack initiation can be uniquely identified. Additionally, the grain size, area fraction, crystallographic orientation, spatial orientation, and texture at the fatigue crack initiation sites have been investigated.

Small fatigue crack growth tests have also been conducted to characterize the variability in small fatigue crack growth rates and relate this variability to the distribution of microstructural features. The same types of analyses have been completed in small fatigue crack growth experiments. Namely, to determine if any of these features enhance the probability of fatigue crack initiation from micronotches or if they affect growth rates.

The results of these analyses are then compared to the distribution of microstructural features observed in the general microstructure as a gauge of the likelihood of initiating a

crack in these regions. This is completed as a method to determine the prevalence of the observed "hot spots" in the nominal microstructure.

This thesis is organized into six chapters. Chapter 1 presents the motivation, approach, and methodology for this study. Chapter 2 summarizes the pertinent literature. Chapter 3 details the experimental methods used in this study. Chapter 4 presents the ultrasonic fatigue behavior and fractographic analysis of fatigue fracture surfaces. The effect of texture on the fatigue crack initiation behavior of this alloys is also described in Chapter 4. Chapter 5 presents the results of the small fatigue crack growth testing on this alloy. Conclusions and recommendations for future work are presented in Chapter 6.

# Chapter 2

# Literature Review

This chapter reviews the literature pertinent to the research described in this thesis. The relevant literature is treated in four distinct sections. The first section deals with physical and mechanical metallurgy and includes discussion of the relevant processing routes and deformation of titanium alloy microstructures. The second section focuses on the fatigue behavior of titanium alloys and relates this to microstructure as it is conventionally understood. This section includes discussion of the effects of microstructure on both fatigue crack initiation and fatigue crack propagation. The third section summarizes literature relevant to the objectives and approach of this thesis and discusses very high cycle fatigue. The fourth section addresses some experimental techniques employed in this thesis. The fifth section is dedicated to summarizing these reports and identifying the open questions which this thesis addresses.

## *2.1 Introduction and Metallurgy of Titanium*

Titanium was first suspected to be a distinct material in 1791 by Gregor upon observation of the oxide ilmenite. In 1795, Klaproth identified rutile as being an oxide of the same material. Due to titanium's affinity for oxygen and nitrogen, it is very difficult to extract. It was not until the twentieth century (1937-1940) that the Kroll process was developed as an effective means for production of pure titanium. The Kroll process involves

extraction of titanium from ore by creating $TiCl_4$ and subsequent reaction with Mg to produce titanium sponge, which can then be melted down and formed into ingots. Usage of titanium increased dramactically during the 1950's and 1960's as aerospace applications needed a strong yet lightweight structural material. Titanium alloys are now commonly used in sports equipment, prostheses, airframes, chemical processing industries and automotive applications, owing to their high specific strength, corrosion resistance, moderate temperature oxidation resistance and biocompatibility [5–7].

As shown in Figure 2.1, titanium alloys exhibit high specific strength relative to other structural metals such as steel and nickel-based alloys, which leads to its use in weight saving applications despite higher costs relative to ferrous materials. They also exhibit good moderate temperature (up to 540°C) fatigue resistance and excellent corrosion resistance. The combination of these properties makes titanium alloys a preferred choice over other iron- and nickel-based structural alloys for aerospace applications, where a balance of strength and weight is desired for moderate temperature applications. Improvements in fatigue resistance result from the ability to refine and control the morphology and composition of the microstructure. The following section describes titanium metallurgy as it relates to processing and mechanical deformation of these alloys.

### 2.1.1 Physical Metallurgy

As the phase diagram in Figure 2.2 illustrates, pure titanium exists in two different crystal structures; the equilibrium phase at room temperature is the alpha phase, while at temperatures higher than 882°C the beta phase is stable. As shown in Figure 2.3 the alpha phase is a hexagonal close-packed structure, and the beta phase exists in a body centered cubic structure. The atoms within the lattice are highlighted in red for clarity. The temperature of this transformation, the beta transus, is determined by the alloy composition. Alloy composition and thermal-mechanical processing routes afford a significant level of control over

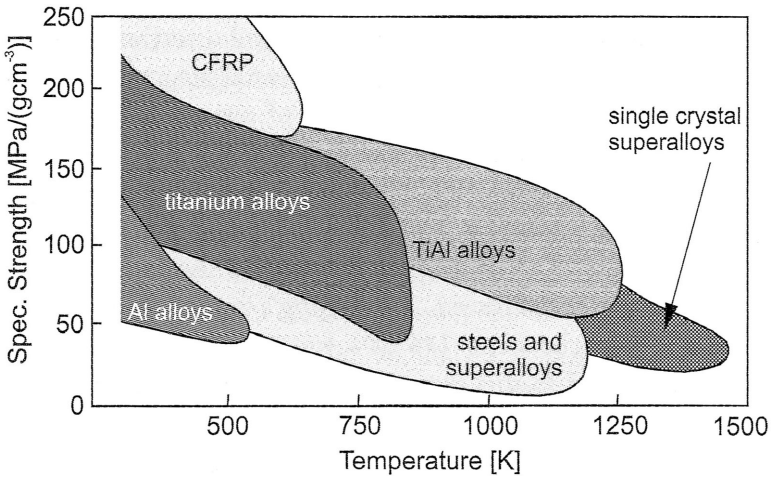


**Figure 2.1:** This plot illustrates that the specific strength of titanium alloys is higher than steel and nickel based alloys below 800 K, after [5].

the morphology of the microstructure and the volume fraction of the $\alpha$ and $\beta$ phases. It is mainly through the manipulation of these phases that the mechanical properties of titanium alloys are controlled. Titanium alloys are generally classified as $\alpha$, $\alpha$+$\beta$, or $\beta$ alloys, depending on the alloy composition or processing routes. The effect of alloying additions will be discussed first.

Aluminum is well known as an $\alpha$-stabilizer, meaning that as its composition is increased, it raises the temperature at which the $\beta \rightarrow \alpha + \beta$ allotropic transformation occurs, as shown in Figure 2.2. Additions of aluminum improve the strength and oxidation behavior of titanium alloys. However, high aluminum content increases slip planarity within the alpha phase, which will be discussed later, and with concentrations in excess of 10% alloys are susceptible to stress corrosion cracking [8]. Additionally, precipitation of the brittle $Ti_3Al$ phase has been observed at concentrations just above 6% aluminum equivalent. The aluminum equivalent is a phenomenological model that quantifies the propensity of various alloying elements to form brittle intermetallic phases and is given in Equation 2.1 [5]. Thus, in applications where damage tolerance is a design criterion, titanium alloys containing less than 6% aluminum are used, and the current discussion of the metallurgy of titanium will

therefore be focused on alloys in this range. Interstitial additions of oxygen, nitrogen and carbon also strengthen the $\alpha$-phase, however they are prone to forming hard alpha and as result are treated as impurities. Tin and zirconium are neutral from a thermodynamic perspective, as they do not affect the $\alpha/\beta$ phase boundary, however they do preferentially segregate to the $\alpha$ phase and increase the strength of the $\alpha$ phase through solid solution strengthening. Common $\beta$-stabilizing elements are molybdenum, vanadium, chromium, niobium and iron, which all decrease the beta transus temperature and strengthen the beta phase by solid solution strengthening.

$$Aleq. = wt.\%Al + 1/3wt.\%Sn + 1/6wt.\%Zr + 10wt.\%O \tag{2.1}$$

In applications where corrosion resistance and deformability are important design criteria, $\alpha$ titanium alloys are typically selected [5]. Also, they are employed in cryogenic applications since they have little or no beta phase present and do not exhibit a ductile to brittle transition, which allows them to maintain their ductility at low temperatures. $\alpha$ titanium alloys generally possess the highest strength and best oxidation resistance while still maintaining good weldability. $\beta$ titanium alloys are typically used in applications where higher strength is required, however this gain is realized at the expense of ductility and weight [5]. $\beta$ titanium alloys are typically used as fasteners, and they exhibit better weldability than $\alpha + \beta$ alloys and do respond to heat treaments [7]. In applications where high specific strengths are required, $\alpha + \beta$ alloys are generally used, since they typically display the beneficial properties of $\alpha$ alloys in combination with the higher strength matrix of $\beta$ phase material, they respond to heat treament, but are less formable than $\alpha$ alloys.

Due to the allotropic transformation, a variety of microstructural morphologies can be achieved through thermomechanical processing and alloying additions, as shown in Figure 2.4. While the composition of the alloy will affect the morphologies that can be achieved,

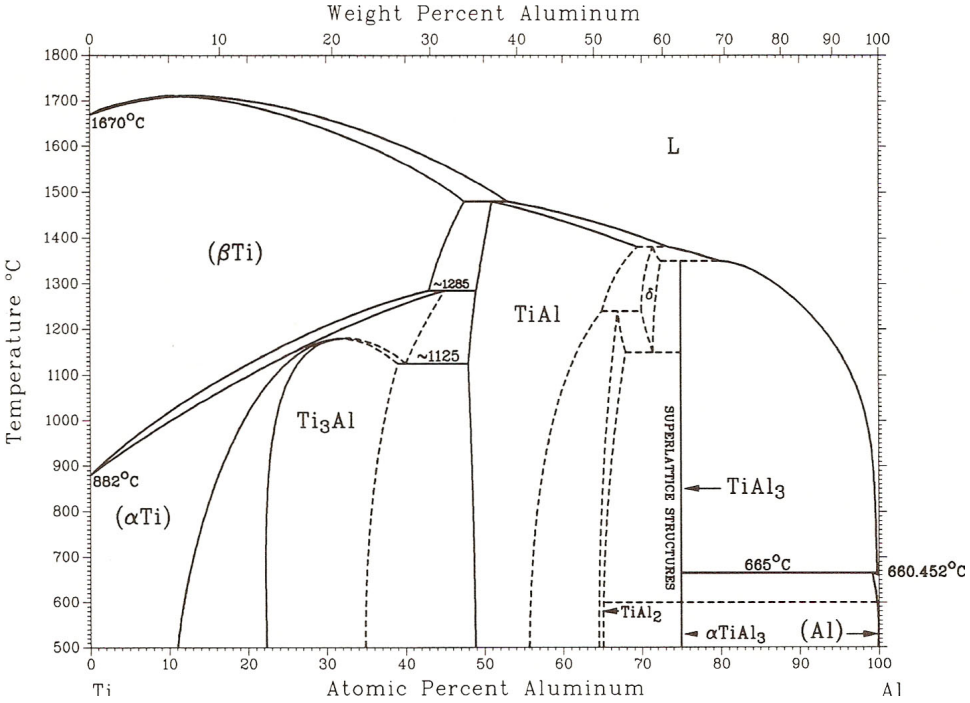


**Figure 2.2:** The binary phase diagram for the titanium aluminum system illustrates the $\alpha$-stabilizing effect that aluminum has when alloyed in titanium, after [9].

these microstructural morphologies result mainly from variations in thermomechanical processing. The most common classes of microstructural morphologies are equiaxed $\alpha$, lamellar $\alpha$, equiaxed $\alpha$ + transformed $\beta$, and Widmanstätten. There are a number of thermomechanical processing steps necessary to form these microstructural morphologies, and these will be discussed in the next section.

### 2.1.2 Description of Microstructure

Figure 2.5 is a schematic of the duplex microstrutures commonly observed in titanium alloys composed of an equiaxed $\alpha_p$ phase and a transformed $\beta$ matrix phase. As this figure shows, there are a number of different features that range in size and morphology. Each of these phases forms due to the thermomechanical processing of these alloys near the allotropic transformation temperature. The lath $\alpha$ phase forms by a transformation from the $\beta$ phase according to the Burgers orientation relationship (OR), and thus the close packed

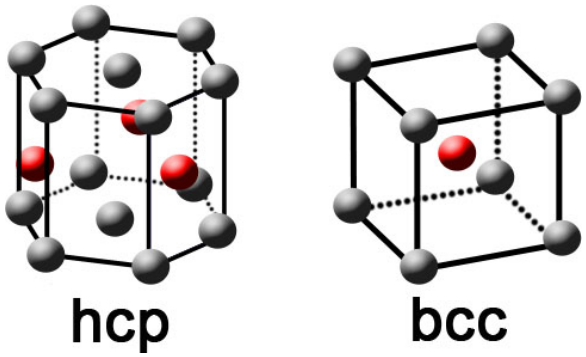


**Figure 2.3:** This schematic depicts the hcp crystal structure of the $\alpha$ phase and the bcc crystal structure of the $\beta$ phase. The atoms in the center plane of the unit cell are shown in red for clarity.

planes of the $\beta$ phase are aligned with the close packed planes in the $\alpha$ phase. As a result, slip is often continuous across the lath $\alpha$ regions, or colonies. The equiaxed $\alpha_p$ grains evolve from $\alpha$ laths by a process of spherodization. During this process, $\alpha_p$ grains do not necessarily maintain the Burgers OR with the beta phase. As a result, slip is not necessarily continuous between $\alpha$ grains and the $\beta$ matrix. The implications of the Burgers OR on slip will be discussed in more detail later. Since mechanical properties often scale with the maximum effective slip length the length scale of the microstructure, it is important to understand the nature of slip transmission across these interfaces and grain boundaries.

### 2.1.3 Thermomechanical Processing of Titanium Alloys

Since the alloy studied in this investigation has been processed in the $\alpha + \beta$ phase field to produce a duplex microstructure, the following discussion focuses on the processing steps required to produce this microstructure and highlights potential defects that may arise from the different stages of processing [5, 6, 10–12].

The forging and heat treatment steps are illustrated schematically for producing duplex alloys in Figure 2.6. To produce bulk material, titanium alloys are homogenized and refined into an ingot using vacuum arc remelting (VAR) or the more recently developed cold hearth

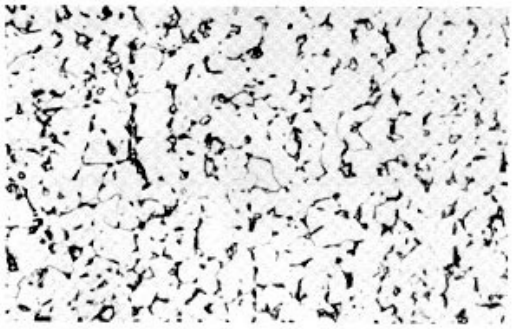

(a) Equiaxed α and a small amount of intergranular β.

(d) Small amount of equiaxed α in an acicular α (transformed β) matrix.

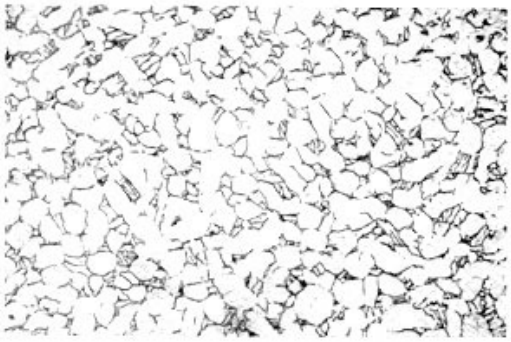

(b) Equiaxed and acicular α and a small amount of intergranular β.

(e) Plate-like acicular α (transformed β); α at prior β grain boundaries.

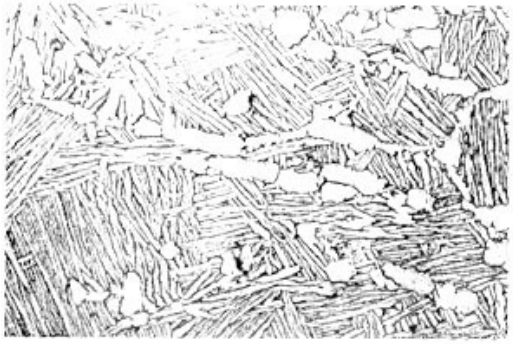


(c) Equiaxed α in an acicular α (transformed β) matrix.

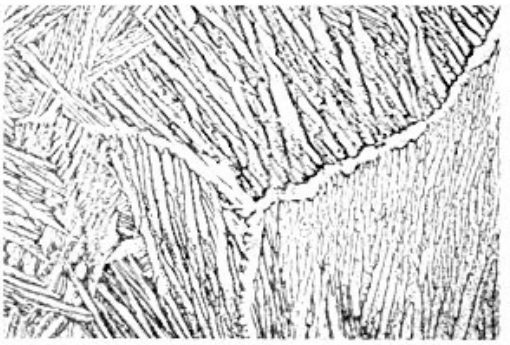


(f) Blocky and plate-like acicular α (transformed β); α at prior β grain boundaries.

**Figure 2.4:** Micrographs depicting the morphology and length scale attainable through control of thermomechanical processing and alloying additions in titanium, after [10]

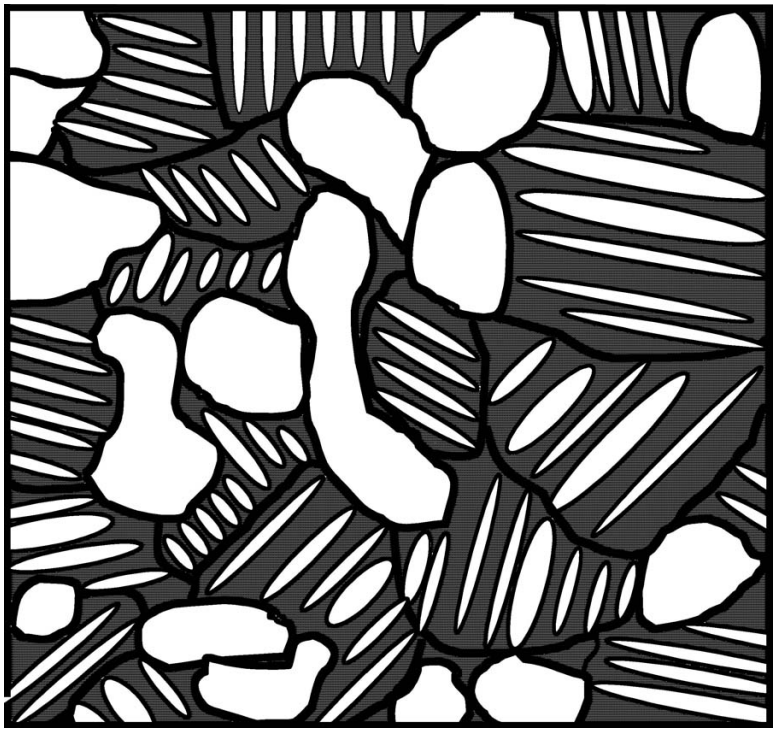

**Figure 2.5:** A schematic depiction of a titanium alloy with a duplex microstructure.

melting. Material can be processed using multiple VAR passes to insure that melt related defects such as hard alpha, high density inclusions, beta flecks, alpha stabilized regions, and voids are not present in the final ingot. Following solidification, the forging and forming operations can result in the formation of microstructural defects such as $\beta$ texture, abnormal $\beta$ grains, $\alpha$ texture resulting from variant selection, and improperly spherodized $\alpha_p$ grains. The processing steps to produce an equiaxed $\alpha$ + transformed $\beta$ microstructure will be discussed below, and the potential for defect creation will be highlighted.

#### *2.1.3.1 β Phase Homogenization*

As shown in Figure 2.6, the first step following solidification of an ingot is to homogenize the $\beta$ grain size and composition within the ingot. The initial rolling or reduction will be completed in the $\beta$ phase field, followed by fan cooling. Due to variations in how the imposed forging strain is distributed among the $\beta$ grains, this step can result in the

formation of abnormally large prior $\beta$ grains or $\beta$ texture. Therefore, the $\beta$ grains need to be recrystallized. The work piece is heavily forged in the $\alpha + \beta$ phase field just below the $\beta$ transus to deform the material sufficiently to serve as the driving force for the nucleation of the recrystallized $\beta$ grains. Then, the material is heated into the $\beta$ phase field and worked 30-40% while the $\beta$ grains recrystallize and the average grain size following this step is on the order of 1 mm. The workpiece is then cooled, and $\alpha$ colonies form according to the Burgers orientation relationship within the prior $\beta$ grains. These primary forging steps homogenize and refine the microstructure of the alloy and also influence the texture of the material that eventually comprises the prior $\beta$ phase.

#### *2.1.3.2 $\alpha + \beta$ phase deformation*

Following the homogenization of the $\beta$ phase, the work piece is forged in the $\alpha + \beta$ phase field. The temperature at which this hot working is completed will determine the final microstructure. For example, forging at temperatures near the $T_\beta$, there will be a lower volume fraction of the $\alpha$ phase and therefore a $\beta$ texture could develop. At lower forging temperatures, an $\alpha$ phase texture can develop. The cooling rate from this forging process will also affect the microstructure by increasing the coarseness of the $\alpha$ laths. At this point, the microstructure is a lamellar $\alpha$ structure, and in this step the material is forged to break up the $\alpha$ lamella. The individual broken segments of the $\alpha$ lamella will coarsen in subsequent processing to form the equiaxed $\alpha_p$ grains. This process is referred to as spherodization, and there are two potential paths that lead to formation of $\alpha_p$ grains from $\alpha$ laths. The first process that can form $\alpha_p$ grains is dynamic spherodization, and this occurs when laths gradually coarsen and become equiaxed in the presence of externally imposed stresses at hot working temperatures. The second mechanism of $\alpha_p$ formation is static spherodization, which occurs at elevated temperatures in the absence of externally imposed stresses by a diffusion process analogous to grain growth. The significance of this is that dynamic

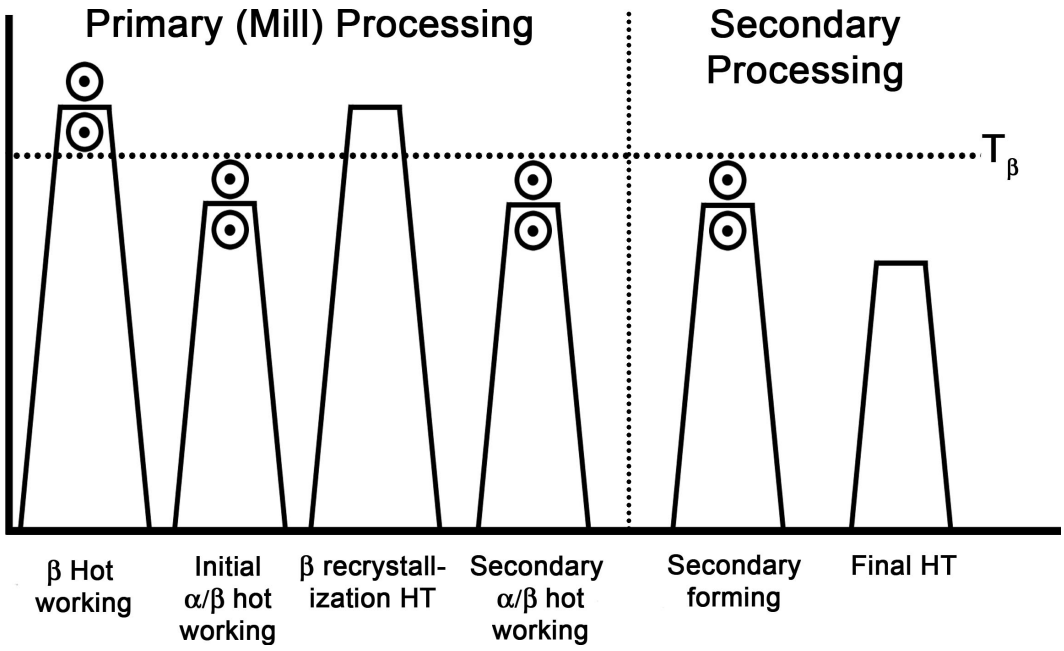


**Figure 2.6:** This diagram schematically depicts the thermomechanical processing employed in the production of duplex titanium alloys. After [11].

spherodization can result in rotation of the $\alpha_p$ grains with respect to the $\beta$ matrix, while static spherodization does not necessarily cause such crystallographic rotation. This will be further discussed in Section 2.1.4.6. Following the spherodization process, the material is cooled, and the lath $\alpha$ nucleates and grows from the prior $\beta$ grains according to the Burgers orientation relationship.

#### *2.1.3.3 Secondary Forming*

Following the mill/primary processing, secondary forging operations are completed to yield a product in the correct form, and during these steps, the $\alpha_p$ grains may coarsen and grow. These steps allow for the refinement of the microstructure and, depending on the temperature at which this forming operation is conducted, different textures may develop. The cooling rate from this processing step will determine the ultimate $\alpha$ lath thickness. Following this process, the material is formed to a near component shape and prepared for final

machining and forming operations.

### 2.1.4 Mechanical Metallurgy of Titanium

#### *2.1.4.1 Slip in HCP Crystals*

Due to the anisotropy of the hcp unit cell, slip deformation in titanium and its alloys is heterogeneous. Many researchers [13–21] have investigated the monotonic deformation of $\alpha + \beta$ titanium alloys to determine the effect of temperature, alloying additions and crystal orientation on the critical resolved shear stress (CRSS) for various slip planes. The typical slip planes in hcp structures are either basal (0001), prismatic $\left(10\bar{1}0\right)$, pyramidal $\left(10\bar{1}1\right)$ or $\left(11\bar{2}2\right)$ -type planes, and Figure 2.7 highlights these planes (red) and slip directions (blue). The slip directions for the first three planes are $\left(11\bar{2}0\right)$ $\langle a\rangle$-type burgers vectors, which are the close packed directions in the hcp cell. In order to accomodate deformation along the $\langle c\rangle$ axis, either twinning or $\langle c + a\rangle$ slip must be activated. For deformation on the $\left(11\bar{2}2\right)$ plane, a nonbasal $\langle c + a\rangle$ Burgers vector, $\left[11\bar{2}3\right]$ is the slip direction. For slip on the $\left(10\bar{1}1\right)$ planes, the $\left[11\bar{2}3\right]$ Burgers vector may also be active [22]. These pryamidal and twinning mechanisms are typically much harder to activate than the other $\langle a\rangle$-type slip systems. However, they may be activated if the crystal is oriented for deformation along the $\langle c\rangle$ axis.

As a first approximation, the active slip systems are the close-packed planes, and in hexagonal crystals the atomic packing fraction on crystallographic planes is related to the c/a ratio of the unit cell. For pure titanium, c/a = 1.587, which is slightly less than the ideal packing ratio of 1.633. Since c/a is less than 1.633 for pure titanium, this approach would suggest that slip will be active on the prism planes since the atomic packing fraction is highest on those planes. However, alloy element additions and elevated temperatures may serve to change the packing density on these planes and activate other slip systems. Of the hcp metals, beryllium is the only metal to exhibit preference for basal slip with increasing purity. Some researchers [23] have suggested that the the stacking fault energy in beryllium

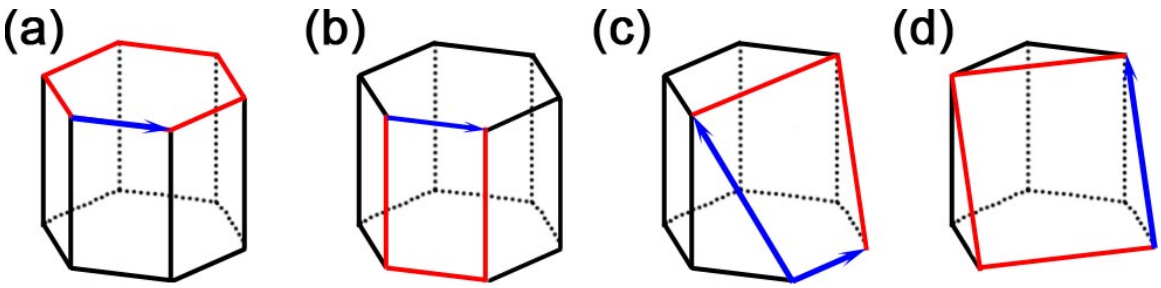


**Figure 2.7:** This figure schematically illustrates the slip planes (red) and possible slip directions (blue) in the hcp crystal structure for a.) basal, b.) prismatic, c.) pyramidal-I, and d.) pyramidal-II.

is low enough that it does not inhibit basal slip.

It is generally [13, 15, 16, 18] agreed that prismatic slip has the lowest critical resolved shear stress of the available deformation modes in pure titanium and Ti-Al alloys. Results from the literature on the monotonic deformation of pure titanium and its alloys with microstructures ranging from single crystals to single colony and polycrystalline samples are summarized in Table 2.1.

#### *2.1.4.2 Slip in Ti-Al Single Crystals*

Paton et al. [13] found that prism slip is easily activated in lean alloys and at low temperatures, but that the CRSS of prismatic slip is sensitive to aluminum concentration and deformation temperature. The CRSS for basal slip, on the other hand, was relatively insensitive to aluminum concentration. Thus, as aluminum concentration is increased, to approximately 6.6%, the CRSS for basal and prism slip was nearly identical. This can be attributed to the fact that $\alpha$-stabilizing subsititutional elements such as aluminum, tin, and oxygen have a smaller bond length than titanium and therefore increase the atomic packing fraction on basal planes relative to prism planes. Williams and coworkers [16] investigated the deformation behavior of Ti-Al single crystals with compositions ranging from 1.4 to 6.6% Al. Both investigations, in the temperature range of 300-1000 K, conclude that the

CRSS for basal and prismatic slip become essentially equal at higher aluminum concentrations and elevated temperatures. Furthermore, they found that the CRSS for $\langle c + a \rangle$ slip on the $\left(11\bar{2}2\right)$ plane is much higher than that for basal or prism slip in these composition ranges and temperatures. Interestingly, the CRSS for pyramidal $\langle a \rangle$ slip is high enough that even in crystals oriented for $\langle c + a \rangle$ slip, basal slip was still preferentially activated when the basal plane normal was only 14° misoriented from the tensile axis.

#### *2.1.4.3 Slip in Ti-Al Single Colony Samples*

The monotonic deformation behavior of single colony samples of near-$\alpha$ titanium alloys has been investigated in a few recent studies [19,20]. These studies investigated the effect of the $\alpha/\beta$ interface on the CRSS for the basal and prismatic slip systems. The earlier work of Suri et al. [20] determined that there is anisotropy in the $a_1$ and $a_2$ slip directions, resulting from the interaction of dislocations with the $\alpha/\beta$ interface. Savage et al. [19] investigated the effect of colony orientation relative to the tensile axis on the measured CRSS, and the results are summarized in Table 2.1. Basal slip, on average, was found to be more difficult to activate than prismatic slip. Numerous finely spaced slip lines were observed in the case of basal slip, whereas in samples oriented for prism slip only a few well-defined slip lines were observed. These observations suggest that increased hardening activity on basal planes relative to prismatic planes was partially responsible for the differences in the CRSS. This is consistent with what was observed by Suri et al. in which work hardening was not observed for crystals oriented for easy slip transfer from $\alpha$ to $\beta$. Ultimately, this is attributed to the alignment of slip planes and directions between the $\alpha$ and $\beta$ planes in the case of prismatic slip, as will be described in Section 2.1.4.6.

#### 2.1.4.4 *Slip in Ti-Al Polycrystals*

The work of Jones and Hutchinson [18] in highly textured polycrystalline Ti-6Al-4V also shows that basal and prismatic slip have a low CRSS. However, their results indicate that the CRSS for $\langle a \rangle$-type pyramidal slip is also quite low, which was previously not reported in the literature. They do agree with other published reports that the CRSS for $\langle c + a \rangle$ slip is higher than that for other slip systems. In situ tests have been completed by Bridier et al. [15] to determine which slip systems are activated to accommodate monotonic deformation in a polycrystalline Ti-6Al-4V alloy with a duplex microstructure. They were able to identify slip traces within $\alpha_p$ grains that corresponded to prism slip in one test and predominantly basal slip in another test. Only in rare cases was the $\langle a \rangle$-type first order pyramidal slip activated. This result agrees with the work of Williams et al. [16] where the pyramidal slip system was observed to have the highest critical resolved shear stress and was therefore least likely to be activated. Zaefferer [17] invesitgated textured Ti-6Al-4V and found that the critical resolved shear stress for prismatic slip was nearly the same as that for basal slip, however actual values were not measured and only relative values were presented. Zaefferer also noted that the critical resolved shear stress for pyramidal slip was quite low, but not many dislocations with a $\langle c + a \rangle$ character were observed in TEM investigations. The absence of $\langle c + a \rangle$ slip was attributed to the fine $\alpha$ grain size and the constraining influence of the $\beta$ phase. Lin and coworkers [21] observed that slip was continuous across alpha colonies, since slip could effectively transfer between the $\alpha$ and $\beta$ phases due to the Burgers orientation relationship. However, Widmanstätten colony boundaries were significant barriers to slip. Peters and coworkers investigated heavily textured Ti-6Al-4V, and they observed that the elastic modulus and yield strength values were found to be higher in orientations where the loading was applied normal to the basal plane [24]. Figure 2.9 is a plot of the CRSS as a function of the angle between the tensile axis and the slip system, where it

is assumed that the (0001) and $\left(10\bar{1}0\right)$ planes deform by $\langle a \rangle$ type slip and the $\left(11\bar{2}1\right)$ planes deform by $\langle c + a \rangle$ slip and the CRSS values are assumed to be a ratio of 1:4, respectively. Thus, the yield stress is expected to be inversely proportional to the bold line drawn in this figure. This figure summarizes the expected slip systems responsible for deformation in $\alpha + \beta$ titanium alloys.

#### *2.1.4.5 Summary of Slip in Ti-Al Alloys*

From these results, basal and prism slip are assumed to have equivalently low CRSS, and a ranking of the CRSS from lowest to highest for the respective slip is prism, basal, and pyramidal $\langle a \rangle$ with an approximate ratio of CRSS of 0.7, 1.0, 3.0, respectively [13, 16]. Commercially relevant titanium alloys are two phase microstructures and therefore the interaction of the $\alpha + \beta$ phases needs to be considered to develop an accurate model of deformation within these complex microstructures. Since the allotropic transformation occurs by a known relationship, the orientation relationship between these two phases must be considered in any description of the slip processes.

**Table 2.1:** Reported CRSS Values for Active Slip Systems in Titanium Alloys. All values given in MPa.

| Slip plane | (0001) | | | $(10\bar{1}0)$ | | | $(10\bar{1}1)$ | | $(11\bar{2}2)$ | Material | Reference |
|---|---|---|---|---|---|---|---|---|---|---|---|
| Slip Direction | $\langle a_1 \rangle$ | $\langle a_2 \rangle$ | $\langle a_3 \rangle$ | $\langle a_1 \rangle$ | $\langle a_2 \rangle$ | $\langle a_3 \rangle$ | $\langle a \rangle$ | $\langle c+a \rangle$ | $\langle c+a \rangle$ | | |
| | - | - | - | - | 218 | - | - | 450* | 450* | Ti-7.0Al(SX) | [13] |
| | - | 210.8 | - | - | 183 | - | - | - | 795 | Textured Ti-6.9Al | [13] |
| | - | 196 | - | - | 196 | - | - | 774** | 774** | Ti-6.6Al(SX) | [16] |
| | - | 444 | - | - | 392 | - | 404 | 631 | - | Ti-6Al-4V | [18] |
| | 245.5 | 286.7 | 217.7 | 208 | 215 | 230 | - | - | - | Ti-6242Si(SC) | [19] |
| | - | - | - | 266.5 | 292.5 | - | - | - | - | Ti-5Al-2.5Sn-0.5Fe(SC) | [20] |

**SX** - Single crystal
**SC** - Single colony

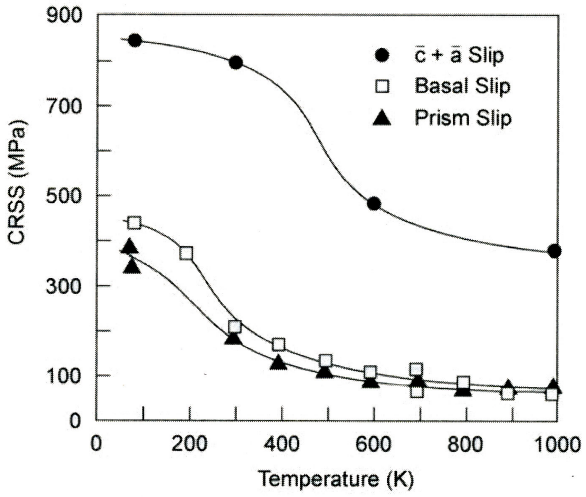


**Figure 2.8:** The plot illustrates the effect of temperatuere on the CRSS of various slip planes in Ti-6.6%Al single crystals. After [13].

#### *2.1.4.6 Effect of Burgers Orientation Relationship on Slip Transmission*

The transformation from the bcc $\beta$ phase to the hcp $\alpha$ phase was first documented in zirconium by Burgers and then later verified in titanium [25]. The Burgers orientation relationship for the $\alpha$ and $\beta$ phases is shown in Equation 2.2, and this illustrates that both the close packed planes and directions in the bcc phase are aligned with the those of the alpha phase. These planes are highlighted in Figure 2.10 for perspective. The symmetry of the hcp and bcc crystal structures leads to the possibility that the hcp crystal structure can be related to the bcc structure in one of twelve different configurations. Due to symmetry, these can be simplified into six unique variants. The investigations of Stanford et al. and Bhattacharyya indicate that there is a variant selection process by which some of these $\alpha$ phase orientations are selected more often than others [26, 27]. Figure 2.10 also illustrates that the slip directions $a_1$ and $b_1$ are aligned, while the $a_2$ and $b_2$ directions are misaligned by 10.63°. High resolution TEM was used to make measurements of the misorientation of these slip directions at the $\alpha/\beta$ interface by Mills et al. [28], and it was found that the misorientation of these directions was actually on the order of 11.7°.

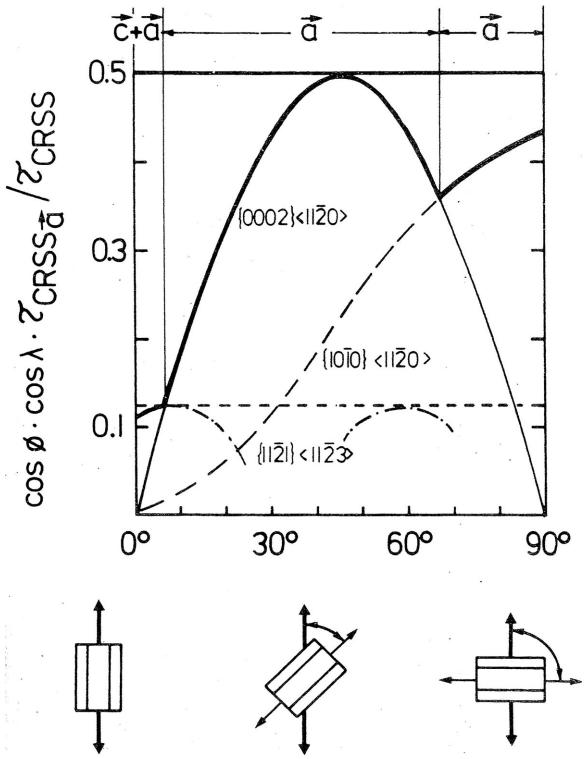


**Figure 2.9:** The plot illustrates variation in slip activity as a function of crystal orientation. After [24].

$$\begin{aligned}(0001)_\alpha \parallel (110)_\beta \\ \left[11\bar{2}0\right]_\alpha \parallel [111]_\beta\end{aligned} \tag{2.2}$$

Initial research [29] indicated that the Burgers OR would result in relatively easy slip transfer across the $\alpha/\beta$ interface. However, recent work by Suri et al. [20] discovered that for specific orientations with respect to the loading axis (i.e. high resolved shear stress along the $a_2$ direction), the $\alpha/\beta$ interface does in fact act as an obstacle to slip transfer. This orientation relationship between the two phases is known to influence the ease of slip transfer across the $\alpha$ and $\beta$ interface, and as a result much research has been conducted characterize the nature of this interface [19, 20, 27, 28]. Thus, the $\alpha/\beta$ grain boundary is not expected to be an effective barrier to slip transfer in the former case. However, it may indeed act as a slight barrier to slip transfer in the latter case. The work of Suri et al. [20] explores the nature this $\alpha/\beta$ interface and its effect on the slip transmission between the two phases. One of the most significant findings of this work was the observation of dislocation pileups at the $\alpha/\beta$ interface for slip activity on $a_2$, but not on $a_1$, which indicates that slip is not hindered by the presence of $\alpha/\beta$ interfaces for configurations in which the slip directions are aligned in the $\alpha$ and $\beta$ phases. Bhattacharyya et al. [27] found that specific variants could be predicted if there was a 10.5° rotation about the $\{110\}_\beta$ orientation in two adjacent $\beta$ grains. The work of Stanford found that the $\alpha$ phase orientations are the same as the orientations of the grain boundary $\alpha$ between $\beta$ grains [26]. Furthermore, if the $\langle 110 \rangle$ planes are parallel in the two adjacent $\beta$ grains, the intermediate $\alpha$ phase will have its c-axis aligned with this direction.

In the formation of $\alpha$ lamella, this transformation results from a nucleation and growth process, and therefore a known relationship between the $\alpha + \beta$ phases exists. The degree to which the $\alpha_p$ phase texture correlates with the prior $\beta$ texture is determined by the severity of the forging and forming operations in the $\alpha + \beta$ phase field [12, 30]. The work of

Woodfield et al. [30] determined that forging strains ($\epsilon$) > 1.0% will result in a loss of the Burgers OR. With static spherodization, the coarsening process allows the individual lamella to maintain a crystallographic relationship with the prior $\beta$ grains. It is through the mechanism of dynamic spherodization that $\alpha_p$ grains may lose the Burgers orientation relationship with respect to the prior $\beta$ grains. To be clear, the $\alpha_p$ grains are not forming through a recrystallization from $\alpha$ lamella, but there may be rotation of the individual segments of spherodizing $\alpha$ lamella relative to the $\beta$ matrix during the forging operation, in which case the Burgers orientation relationship is not maintained. Thus, if the strains imposed in the billet are not high enough to initiate the process of dynamic spherodization, the $\alpha$ lamella can form $\alpha_p$ grains through the process of static spherodization. The amount of strain imposed during billet reduction will result in varying amounts of $\alpha_p$ grains that maintain the Burgers orientation relationship. Mechanical properties such as tensile strength or fatigue behavior that are affected by the $\alpha$ phase texture can thus be related to the homogeneity of the prior $\beta$ texture. In summary, the $\alpha_p$ grains will maintain the Burgers orientation relationship if the material is not heavily deformed, while the lath $\alpha$ will nearly always maintain the Burgers orientation relationship, since it forms upon cooling from the $\beta$ phase and is not subjected to any deformation process.

Given that the active slip systems in both the hcp $\alpha$ and bcc $\beta$ phases will bear some relationship with one another, the thermomechanical processing will influence the strength of these alloys and serve to determine which slip planes will become active. The significance of this is that if the active slip plane in the $\alpha$ phase is not aligned with that of the $\beta$ phase, it will be difficult for this region of microstructure to accommodate deformation. The incompatibility of slip across adjacent grains is often cited as a likely reason for strain localization.

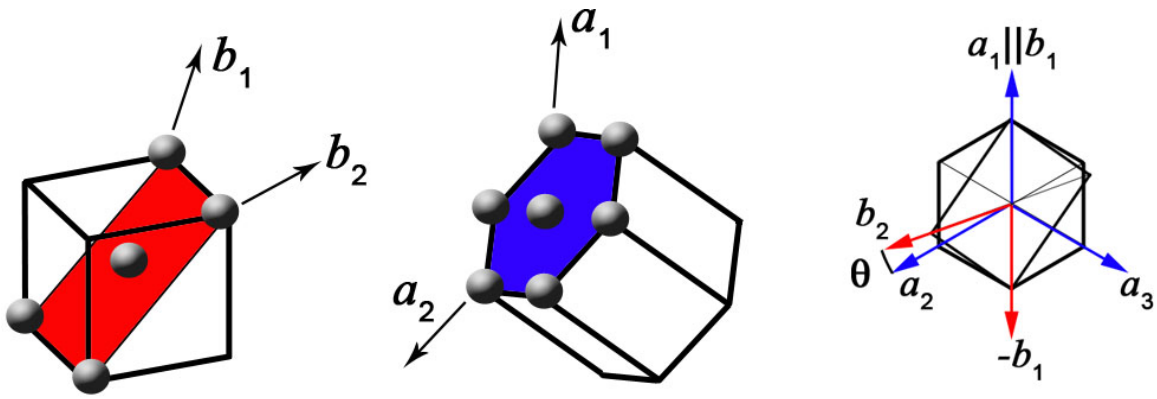


**Figure 2.10:** This figure displays the Burgers orientation relationship between the alpha and beta phases. The (0001) plane of the $\alpha$ phase and the (110) plane of the $\beta$ phase have been highlighted for clarity. The image on the right depicts the relationship between the slip directions in the $\alpha$ and $\beta$ phases.

## *2.2 Fatigue of $\alpha + \beta$ titanium alloys*

The paradigm for determining the total fatigue lifetime of any structural component is to sum the number of cycles necessary for fatigue crack initiation and fatigue crack growth. Hall [31] refines this paradigm by dividing the crack growth contribution into two components which describe small fatigue crack growth and long fatigue crack growth as distinct components of the total fatigue life since these two regimes of behavior are affected by microstructure in different ways. This is shown in Equation 2.3, where $N_t$ is the total fatigue lifetime, $N_n$ is the number of cycles to fatigue crack initiation, $N_s$ is the contribution of small fatigue crack growth, $N_\sigma$ is the contribution of stable crack growth described by linear elastic fracture mechanics, and $N_\delta$ is the portion of life spent in unstable crack growth. The relative percentage of lifetime occupied by these individual components are determined by the testing conditions and the material being investigated.

$$N_t = N_n + N_s + N_\sigma + N_\delta \tag{2.3}$$

A review of monotonic and cyclic mechanical behavior by Margolin and coworkers

identifies that the fatigue performance of Ti-Al alloys is determined by the deformation behavior and strength [32]. Alloys that are likely to exhibit strain localization tend to have poor low cycle fatigue (LCF) ($\leq 10^3$ cycles) properties due to early crack intitiation in slip bands, while alloys that exhibit higher strengths will display longer fatigue lifetimes in the high cycle fatigue range. Margolin and coworkers also cite the ability of similarly oriented grains to transmit slip from one grain to another in these alloys. In the LCF regime, crack initiation occurs very early in life [33], and fatigue lifetimes are dominated by the fatigue crack growth mechanisms [4]. At lower stresses in the regimes of high cycle (HCF) ($10^4 - 10^7$ cycles) and very high cycle fatigue (VHCF) ($10^7 - 10^9$ cycles), fatigue crack initiation occupies increasingly larger portions of the total fatigue lifetime [34, 35]. Thus microstructural morphologies that exhibit improved LCF behavior, i.e. higher fatigue crack growth resistance, generally will not exhibit superior HCF behavior, due to their inferior fatigue crack initiation resistance.

The following sections describe the effect of microstructure on the fatigue performance of titanium alloys. Due to the allotropic transformation and variations in thermomechanical processing, commercial titanium alloys can be processed to yield multiphase microstructures with multiscalar features ranging from $\alpha$ laths less than 1 $\mu$m in size to regions of microtexture, which are on the order of 500 $\mu$m. Thus, a significant level of control over microstructure and hence the mechanical properties is attainable. The discussion of previous work will focus on the effects of microstructure, but certain investigations in which environment or test conditions were varied will be highlighted when they provide insight into the process of fatigue damage accumulation.

### 2.2.1 Damage Accumulation and Fatigue Crack Initiation

The determination of when a fatigue crack has initiated is often open to interpretation and is generally determined by the detection limits of the experimental equipment. Alternatively, the number of cycles for crack initiation can be defined based on when a crack starts behaving as a propagating fatigue crack. This will be determined by the scale of the microstructure and as such, fatigue cracks are considered to have initiated at different length scales, ranging from individual $\alpha$ laths [36] to large $\alpha$ colonies [37, 38]. Hall presents the formalism for this approach by defining these fatigue critical microstructural features as crack-like discontinuities (CLD). A CLD is defined as the minimum feature size at which the accumulated fatigue damage begins to behave as a fatigue crack. As Figure 2.11 illustrates, a CLD may be related to the scale of the microstructure and for different heats of material may be defined as $\alpha_p$ grains, $\alpha$ colonies, prior $\beta$ grains, or the size of microtextured regions. The multiscalar nature of titanium alloys has been noted in a number of studies [32, 39] and is the subject of a recent paper by Rugg and coworkers [40] in which they define the term effective structural unit size, which is the length scale over which deformation processes do not recognize boundaries. The distribution of these neighborhoods or microstructural "hot spots" will determine the distribution of fatigue lifetimes. They cite the significance of microtexturing on mechanical properties such as cold dwell fatigue and notched high cycle fatigue as an example where the effective structural unit size that is much larger than the grain size affects mechanical properties. Thus, both the microstructure and the type of fatigue loading will ultimately determine the length scale of deformation and, hence, which microstructural feature is responsible for fatigue crack initiation.

Much of the literature on fatigue crack initiation in $\alpha + \beta$ titanium alloys focuses on analysis of the fracture surfaces to determine the deformation and possible strain accumulation mechanisms that are responsible for crack initiation. In materials that do not contain

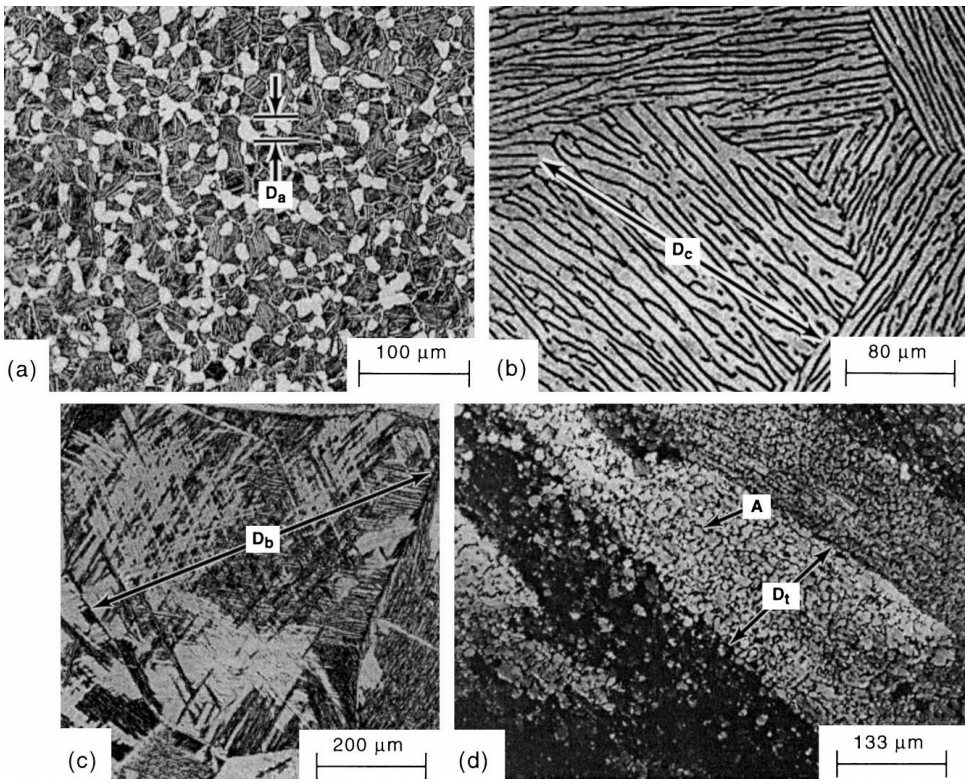


**Figure 2.11:** This figure depicts the range of microstructural features which can be responsible for fatigue crack initiation in $\alpha + \beta$ titanium alloys. a.) $\alpha_p$ grains b.) $\alpha$ colonies c.) prior $\beta$ grains d.) microtextured regions. Taken from [41].

inclusions or porosity, fatigue cracks will initiate in locations where the local microstructure promotes the accumulation of irreversible slip [34]. Hall's review [41] of fatigue crack initiation in $\alpha + \beta$ titanium alloys establishes that fatigue damage typically accumulates in the alpha phase. This is physically reasonable since the $\alpha$ phase is typically the higher volume phase, it has a higher propensity for strain localization, and the $\beta$ phase is typically harder owing to precipitation strengthening and a longer slip length($|b_1| > |a_1|$).

The fatigue critical microstructural features have been identified as anamolous microstructural features such as large $\alpha_p$ grains, $\alpha$ colonies, prior $\beta$ grains, clusters of $\alpha_p$ grains or microtextured regions of similarly oriented $\alpha$ grains, as shown in Figure 2.11. The cited mechanisms of fatigue crack initiation are slip band formation in $\alpha$, $\alpha/\beta$ strain incompatibility, strain incompatibility between adjacent $\alpha$ grains, or damage accumulation across microtextured regions. In some investigations, mechanisms such as pseudo-cleavage fracture of $\alpha$ grains or colonies have been proposed to account for the observation of facets on the fracture surface at the site of fatigue crack initiation.

Numerous studies of fatigue behavior in $\alpha + \beta$ titanium alloys have been conducted to determine the mechanism of fatigue crack initiation. The mechanism of crack initiation depends on initial microstructure, and materials with a duplex microstructure are commonly observed to initiate fatigue cracks on the basal plane of the $\alpha_p$ grains [24,30,37,38,42–44]. Though, for certain microstructures and testing conditions, fatigue crack initiation was observed on prism planes [45–47]. More recent work [46, 48, 49] has observed that both basal and prism slip are activated in the crack initiating volume of material. In transformed $\beta$ structures, cracks typically initiate across the alpha colony or along the lath $\alpha/\beta$ interface. Applied stress level will influence the crack initiation location as well. Typically, testing at higher stresses will encourage the formation of slip bands within the $\alpha_p$ grains or across $\alpha$ colonies [24, 37, 38, 42, 50–53]. However at lower stresses, many researchers [33,36,50,53–57] have cited the $\alpha/\beta$ interface as the initiation site. In both cases,

it is assumed that damage accumulation within the $\alpha$ phase leads to fatigue crack initiation. At high stresses, the slip activity is severe enough that formation of slip bands is observed. However, for testing completed at lower stresses, slip activity is more moderate and as a result, continued cycling will lead to the accumulation of damage at the $\alpha/\beta$ interface, and eventually fatigue crack initiation occurs at these locations due to strain incompatibility. In subsequent sections, the range of microstructural features and mechanisms responsible for fatigue crack initiation will be described.

#### *2.2.1.1 Fatigue Critical Microstructural Features*

Fatigue crack initiation sites are often described as neighborhoods of material where the local microstructure is suitably oriented for slip accumulation. This is found to be the case in Ni-based alloys [58], and is also true in titanium alloys where the two-phase nature of the microstructures will affect the slip properties and damage accumulation mechanisms within the phases. Two locations for crack initiation were noted across a number of studies in the literature; namely crack initiation at $\alpha/\beta$ interfaces and cracks initiating from slip bands within $\alpha$ grains. In some cases, the slip bands in $\alpha$ caused decohesion of the $\alpha$ grain from the $\beta$ matrix. Slip was intensified in cases where a number of $\alpha$ grains favorably oriented for slip were in close proximity to one another. The next subsections detail the microstructural configurations that enhance strain localization and fatigue crack initiation.

*$\alpha_p$ grains*

Mahajan and Margolin [51] found that, in Ti-6246, fatigue cracks initiated in large $\alpha$ grains or in areas where a number of $\alpha$ grains were clustered together. They speculated that both of these features allowed slip to accumulate over long distances. At low strain levels ($\varepsilon_T/2$=0.7-0.9 pct) crack initiation occurred at predominantly $\alpha/\beta$ interfaces, while for higher strains ($\varepsilon_T/2$ $\geq$1.0 pct) crack initiation was favored within primary $\alpha$ grains.

The basis for this behavior was proposed to be that the amount of irreversible slip accumulated in the grain is proportional to the length of the slip path. These findings were corroroborated in equiaxed $\alpha$ microstructures by Benson et al. [33] and by Akahori [54] and coworkers in Widmanstätten and duplex microstructures. Based on their findings, Mahajan and Margolin suggested that a likely method for improving the fatigue resistance of this alloy is to increase the spacing between $\alpha$ grains or to refine the $\alpha_p$ grain size to limit slip transmission between $\alpha_p$ grains or plastic deformation within grains, respectively.

*$\alpha$ colonies*

Akahori [54] and coworkers observed that crack initiation occurred across $\alpha$ colonies in Widmanstätten structures. Further evidence for the development of slip bands across $\alpha$ colonies is found in the work of other researchers [36, 38, 42, 59], and these observations illustrate that slip is easily transmitted across the $\alpha$ laths in the transformed $\beta$ regions. In one study, the size of the initial crack was observed to be stress dependent, with cracks initiating in one $\alpha$ needle at low stresses and across one or two full colonies at higher stresses [36]. The ease of slip transfer in these regions is attributed to the Burgers orientation relationship. The accumulation of slip across $\alpha_p$/transformed $\beta$ interfaces has been observed by Bridier and coworkers [15], as well. These regions are typically larger than $\alpha_p$ grains and thus, they are often the dimension of maximum slip accumulation in $\alpha$. Ruppen observed that cracks initiated in $\alpha$ colonies where the $\alpha$ platlets were aligned with one another [59]. The initiation facets were observed to be oriented at 45-55° with respect to the tensile axis.

*$\alpha_p$ clusters*

Ravi Chandran and Jha [60] determined that clusters of $\alpha_p$ grains are the fatigue critical microstructural features in Ti-10V-2Fe-3Al in one population of failures, and were able to correlate the sensitivity in lifetimes to the defect population using Poisson statistics. This work provided evidence to support the theory of earlier researchers [51] that cited $\alpha$ clusters as the microstructural neighborhood responsible for fatigue crack initiation and that

increasing the spacing between $\alpha_p$ grains acts to reduce slip transmission between grains.

*Microtextured regions*

Gilbert and Piehler [61] speculated that regions of similarly oriented $\alpha$ grains could serve as the fatigue crack initiation sites when they observed subsurface cracking in specimens subjected to bending fatigue. Regions of material with similar crystallographic orientation are observed to initiate fatigue cracks in a number of titanium alloys [30, 41, 46, 48, 49]. Notably, LeBiavant et al. [48] found that microtextured regions that are inherited from the $\beta$ texture are microstructural regions that are more susceptible to fatigue crack initiation. Increased susceptibility of microtextured regions to fatigue cracking is speculated to occur, since fatigue damage is accomodated nearly uniformally in these regions. Woodfield and coworkers [30] also observed that these heterogenous regions of preferred texture were the initiation sites favored for fatigue cracks under conditions of dwell fatigue loading. Bieler and Semiatin [12] built on the work of Woodfield et al. and established that the presence of these microtextured regions results from local heterogeneities in deformation during thermomechanical processing. Sinha [62] observed that cracks initiate in numerous microtextured regions throughout a sample. However, the fatal fatigue crack is not the first to initiate, but it does initiate in the largest region of microtexture.

Similar microstructural features are reported as the fatigue crack initiation sites in Waspaloy by Davidson et al [58]. They found that the crack initiation sites are associated with clusters of similarly-oriented grains, which they termed "supergrains." They suggested that supergrains were more susceptible to fatigue crack initiation, because localized deformation in one grain could be more easily accommodated in adjacent grains due to their similar crystallographic orientation leading to damage accumulation across these regions.

*Prior $\beta$ grain boundaries*

Stubbington and Bowen [56] observed that the $\alpha/\beta$ interface was a likely crack initiation location at low stresses and that the likelihood of cracks initiating there was enhanced if the

$\alpha$ grain happened to sit at the prior $\beta$ grain boundary. In an investigation of $\beta$-Cez and Ti-6246 in the $\beta$ processed condition, Sauer and Lutjering [55] observed that cracks initiated at the $\alpha$ grain boundary layers found at the prior $\beta$ grain boundaries. Krupp and coworkers found that cracks initiate at grain boundaries of $\beta$ grains, due to the elastic anisotropy at this interface [63].

#### *2.2.1.2 Fatigue Crack Initiation Mechanisms*

Each of the fatigue critical microstructural neighborhoods have been identified as crack initiating regions because of their propensity to accumulate the necessary cyclic damage to initiate fatigue cracks. Even though a number of microstructural regions are found to be capable of initiating fatigue cracks, there are essentially just two mechanisms by which cyclic damage accumulates and microstructural interactions cause a fatigue crack to initiate. In all of these studies, fatigue cracks are initiated due to slip accumulation within a grain, colony, or microtextured region (e.g. slip bands, slip transfer to adjacent laths) or by a mechanism of slip incompatibility at an interface such as a grain boundary, colony boundary or the edge of two prior $\beta$ grains. A general observation is that at high stresses, strain localization within a given microstructural feature will cause cyclic plasticity capable of initiating a fatigue crack. At lower stresses, it appears that the requisite amount of cyclic plasticity is typically not achieved within an individual microstructural component, and thus fatigue cracks are observed to intiate in locations where slip activity is hindered, such as grain boundaries, colony boundaries, or the interface of prior $\beta$ grains. There is an effect due to microstructural conditions as well, since the microstructure will control the effective slip length. The initial slip events can still be attributed to specific crystallographic planes within these microstructural features, and this will be discussed as a measure of the likelihood for fatigue damage to initiate on these planes.

Because the work of Mahajan and Margolin spans different regimes of stresses, they

observe crack initiation at interfaces at low stresses and within $\alpha$ grains at high stresses. Baxter et al. observed that slip occurred primarily on basal planes within $\alpha_p$ grains, but prism planes were active in the absence of grains that were suitably oriented for basal slip [42]. They completed tests at 80-100% of $\sigma_{YS}$ and observed that slip was continuous across lath alpha in transformed $\beta$ regions. Eylon and Pierce found that cracks initiated in a single $\alpha$ needle at low stresses and across $\alpha$ colonies at higher stresses [36].

Feaugas and Clavel [64] found that slip in Ti-6246 occurred primarily on prism planes and formed intense slip bands within the alpha phase. However, there was evidence of $\langle \vec{c} + \vec{a} \rangle$ slip in first or second order pyramidal planes $\left\{10\bar{1}1\right\}$ or $\left\{11\bar{2}2\right\}$ and $\langle a \rangle$ type slip in first order pyramidial planes. It was found that secondary slip depends on $\alpha_p$ grain orientation, temperature, and type of loading, although prismatic slip is found to be the most common slip mode in the $\alpha$ phase independent of the testing temperature. The researchers categorized microstructural heterogeneity into three classes according to the level at which slip transmission is most affected. They are: incompatibility of slip between $\alpha$ grains of differing orientations, incompatibility of slip between $\alpha$ and $\beta$ phases, and localization of slip into bands within the $\alpha$ phase.

One mechanism of fatigue crack initiation due to strain incompatibility at colony boundaries has generated much attention in the past few years. This mechanism is often referred to as the modified Stroh mechanism, where crack initiation on basal planes of the hexagonal crystal structure is attributed to the operation of a pseudo cleavage mechanism. This is a form of the Stroh mechanism modified to account for cyclic loading, as shown in Figure 2.12, in which slip is activated on planes with a high resolved shear stress, leading to fatigue crack initiation resulting in a cleavage facet in an adjacent grain. Thus, the facet that appears to form by cleavage is in fact created by the impinging stress of the adjacent grain and by the macroscopically applied stress. Stroh initially proposed this model as a mechanism of fracture in monotonic loading of metals [65], and the idea was first proposed by

Neal and Blenkinsop [44] to account for fatigue cracks that were observed to initiate from facets that formed in $\alpha$ grains or colonies in which the basal plane was oriented normal to the loading axis. Neal and Blenkinsop cited the Stroh mechanism of fracture in monotonic loading as an analogue to their observations of facet formation under cyclic loading conditions, but they acknowledged that it is not clear how the monotonic loading case translates to the cyclic loading case. In another paper [66], Evans discusses fatigue crack initiation in $\alpha + \beta$ titanium alloys as an issue of stress redistribution in the matrix due to the interaction of $\alpha + \beta$ grains based on their orientations relative to the stress axis.

These defects are examples of how a fatigue crack is observed to initiate from a neighborhood of material rather than from an individual grain. This mechanism of fatigue crack formation has been observed in the formation of cracks in specimens tested under dwell fatigue conditions. More recent work in this area by Sackett and coworkers [67] still focuses on this pseudo-cleavage mechanism of fatigue crack initiation. However, the supporting micrographs shown in Figure 2.13 provide evidence that crack initiation in these regions is still caused by slip processes on a plane of high resolved shear stress. It may be just a matter of defining when a fatigue crack has initiated as it is clear that these planes are favorably oriented for slip.

### 2.2.2 Fatigue Crack Propagation

As observed by a number of researchers [4, 41, 69–72] and shown in Equation 2.3, fatigue crack propagation rates for small cracks are observed to be higher than the propagation rates observed in long fatigue crack growth. By definition, small fatigue cracks must satisfy one of the following criteria: they are small compared to microstructural dimensions, small compared to the scale of local plasticity, or when they are simply physically small (<0.5-1 mm) [69]. The significance of small fatigue cracks is illustrated in Figure 2.14 [73];

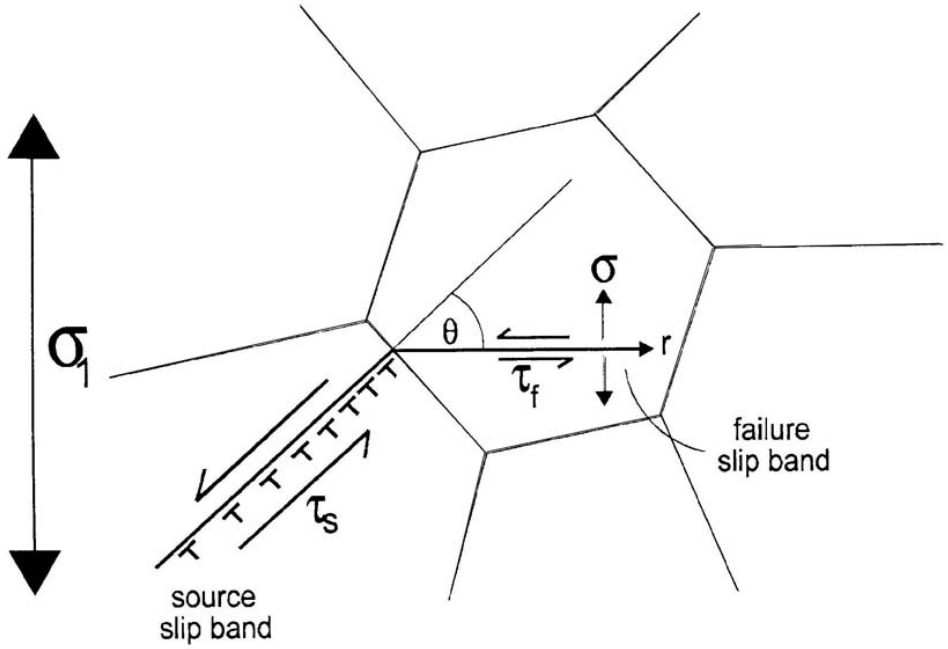


**Figure 2.12:** A schematic depiction of the Stroh model for planar slip. From [68].

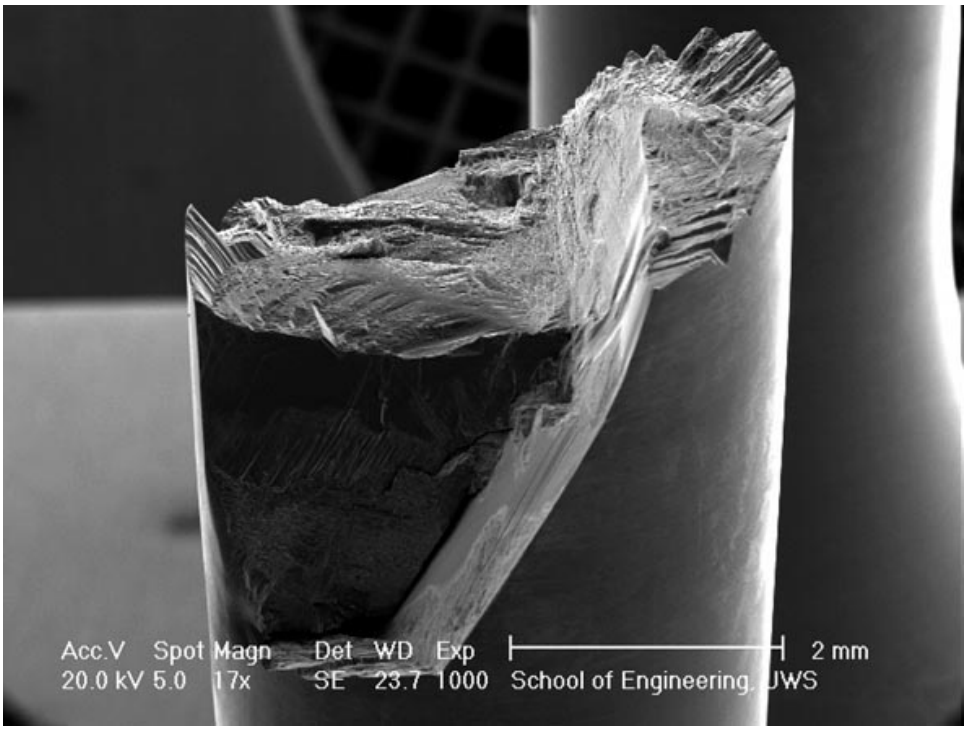


**Figure 2.13:** A fractograph which displays the overall appearance of the fracture surface attributed to form by a modified form of the Stroh mechanism. From [67].

namely, they propagate at least as fast and in some cases faster than long cracks for equivalent stress intensity values [70]. Additionally, small cracks have been shown to propagate at stress intensity values below the long fatigue crack growth threshold, as shown by curve S3 in Figure 2.14. Therefore, from the perspective of accurately predicting fatigue lifetimes, it is critical to account for the so-called small crack effect. In addition to this, significant variability in growth rates for small cracks occurs in the near-threshold regime of fatigue crack growth, which is generally attributed to microstructural dissimilitude [71, 72]. When cracks propagate at larger sizes, very little scatter in the crack growth rates is observed. Lankford [71] observed that small cracks may decelerate as they approach adjacent grains. He proposed that grain boundaries are not necessarily responsible for the deceleration of fatigue cracks, but rather the different crystallographic orientation of the adjacent grain causes this deceleration. This is thought to result from the necessity of the crack to change direction to propagate along another crystallographic direction. At grain boundaries, some of these fatigue cracks were observed to arrest. At these locations of crack arrest, initiation sites have been identified, which indicates that fatigue cracks re-initiated before propagating into adjacent grains. Thus, the following sections discuss fatigue crack propagation and will focus on small fatigue cracks and the effect of microstructure on the variability in growth rates.

#### *2.2.2.1 Effect of Microstructure on Fatigue Crack Growth in Titanium Alloys*

The fatigue crack growth behavior of titanium alloys has been the focus of many studies [50, 63, 74–87]. These investigations attempt to relate microstructure to the fatigue crack growth behavior, and often this is done on a macroscopic scale. Many reports cite the improved fatigue crack growth resistance of macrocracks in coarse microstructures, whereas microcrack propagation resistance is enhanced in fine grained alloys as observed by Hines and Luetjering [84]. The improved crack growth resistance is typically attributed

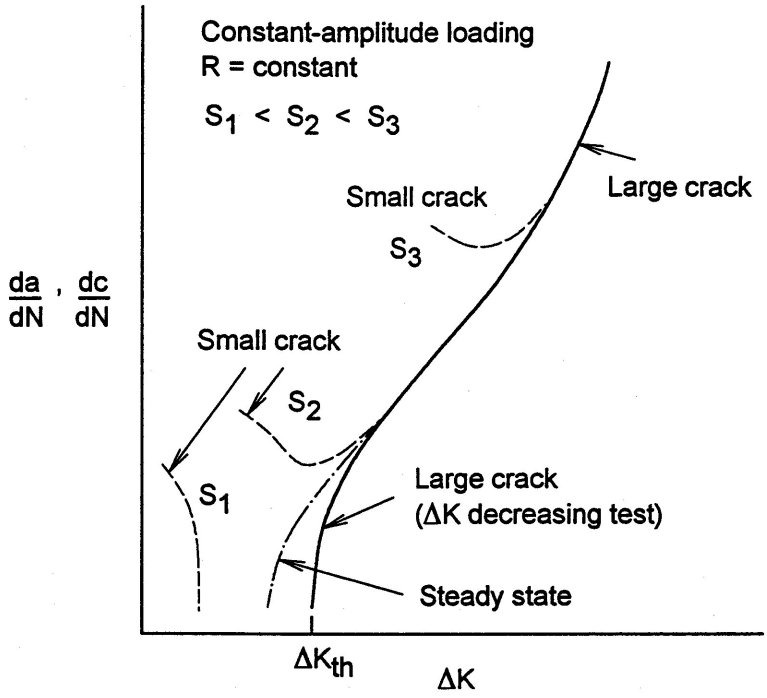


**Figure 2.14:** This schematic depicts the growth rates of small cracks that can sometimes be higher than expected based on long fatigue crack growth rates. From [73].

to greater crack deflection in coarse microstructures relative to that observed in fine grain alloys [77,79–82]. Crack deflection reduces growth rates by causing a propagating crack to change direction [71], or by increasing crack path tortuosity [79, 80], which enhances the benefits of fatigue crack closure [88]. Improved fatigue crack growth resistance is sometimes attributed to other factors, including texture [75], slip character [76], or favorable microstructural neighborhoods, such as microtextured regions [74] and grain clusters with specific misorientations [63]. The effect of microstructural scale will be addressed first and then specific examples will be discussed that highlight the effect of local grain orientations or provide unique insight into the damage accumulation process.

Jin and Mall [77] examined the small crack growth behavior of coarse and fine lamellar microstructures of Ti-6242-Si, and they observed that coarse lamellar microstructures exhibited a small crack effect, while the fine structures do not. They attribute the small crack

effect in these microstructures to the breakdown of microstructural similitude. However, closure measurements were not made, and as a result, it is not possible to rule out roughness induced closure as a cause of the observed small crack effect. Schroeder et al. [80] investigated the effects of microstructure on fatigue crack growth rates with lamellar and a so called bi-lamellar microstructure, which is annealed to produce thicker beta-laths between the lath alpha. They observed slower fatigue crack propagation of microcracks for the bi-lamellar microstructures and attributed this to the effectiveness of the $\beta$ laths in reducing slip transfer between adjacent $\alpha$ laths. However, once cracks begin to propagate as macrocracks, the bi-lamellar microstructure exhibits poorer fatigue performance. This is attributed to the fact that the fracture surface is relatively flat on a macroscopic scale.

Sinha [82] examined the effects of closure on the fatigue crack propagation in lamellar structures. They found that the coarser lamellar structures had a higher degree of closure and additionally slower propagation rates. However, even at higher stress ratios (R=0.8), which are thought to be closure-free, the coarser structures had slower propagation rates. This observation lead Sinha and Soboyejo to conclude that the coarser microstructures displayed slower fatigue crack propagation rates due to the intrinsic effects of the microstructure. They cited the increased tortuoisity of the fracture surface correlated with the observed improvement in fatigue crack growth resistance due to crack deflection.

Bowen [75] investigated the effects of texture on the fatigue crack propagation rates in Ti-6Al-4V for specific specimen orientations. In half of the samples, predominantly $\left\{10\bar{1}0\right\}$ slip and $\left\{11\bar{2}1\right\}$ twinning were observed to be the active deformation modes and deformation was observed to occur symmetrically about the crack tip, leading to a nominally flat fracture surface. Slightly lower fatigue crack growth rates are observed when deformation is symmetric about the crack tip, suggesting that symmetric deformation acts as a toughening mechanism, thereby increasing the ability of the microstructure to accumulate more fatigue cycles with limited crack extension. In specimens where asymmetric deformation

is observed at the crack tip, fatigue cracks are observed to grow faster, since slip damage is concentrated on one specific slip system. Gray and coworers acquired similar results by studying the effect of oxygen concentration on slip character in titanium alloys [76]. As the oxygen concentration increased, the fatigue crack growth rates increased at high stress ratios (R=0.8). At low stress ratios (R=0.1), higher fatigue crack growth rates were observed in the alloys containing low concentrations of oxygen. Since increasing oxygen concentration is observed to shut down slip systems in titanium [16], the reduction in growth rates of alloys containing high oxygen concentrations was attributed to the relative ease of slip reversibility. Also, with less active slip systems, the alloy with higher concentrations of oxygen will have a more tortuous fracture path, resulting from greater crack deflection, and thus it will exhibit a lower fatigue crack growth rate. This work displays similarities with the findings of Krupp et al. in which they observed that if a single slip system was activated, the crack growth rates would be fast, whereas multiple active slip systems served to decelerate the propagating fatigue crack.

Saleh and Margolin investigated the crack paths of propagating fatigue cracks in Ti-Mn alloys, and they observed that fatigue cracks are mostly associated with the $\alpha$ phase in two phase alloys [50]. Notably, they observe cracks that form on slip bands in the $\alpha$ phase are not always transmitted to the $\beta$ phase despite the alignment of slip planes between these phases as governed by the Burgers orientation relationship. Similar findings are detailed by Helbert et al. [39] in which fatigue crack growth rates were observed to be proportional to $\lambda/\phi$, where $\lambda$ is the center to center distance between $\alpha$ particles and $\phi$ is their diameter. The work of Helbert et al. agrees with the work of Schroeder in the fact that the effective slip length is an important parameter controlling the fatigue crack growth behavior.

The work of Krupp et al. [63] indicates that the local microstructural configurations will have a significant effect on the fatigue crack growth rates in a $\beta$ titanium alloy. Grain boundaries with large misorientations ($\theta$=15°) are the preferred sites for fatigue crack initiation,

due to the high elastic anisotropy at these sites. Minimal fatigue crack growth retardation is observed as cracks propagate across low misorientation angle boundaries or if there is a small angle between the propagation direction of an approaching microcrack and the slip plane in the next grain.

## *2.3 Very High Cycle Fatigue*

The study of very high cycle fatigue (VHCF) behavior is attracting increased interest from industry, since many components in structural applications such as automobile cylinder heads, engine blocks [89] and turbine engines will accumulate $10^8$ to $10^{10}$ cycles in service. The conventional approach of designing components to a fatigue limit is not applicable in VHCF, since fatigue failures have been observed [90] below the conventional fatigue limit. This has led some researchers [91] to propose a modified S-N curve where surface initiated fatigue failures are observed at high stresses and subsurface fatigue crack initiation is observed at very long lifetimes below the conventional fatigue limit. Mughrabi [34] explained failures below the conventional fatigue limit in terms of fundamental physical mechanisms of fatigue damage accumulation by suggesting that even though macroscopic strain in VHCF is below the PSB threshold, slip irreversibility can still accumulate and lead to failure. This agrees with the work of Lukás and Kunz [92] who argue that in the VHCF regime the applied strain is nominally elastic and only localized plastic deformation will accumulate at specific microstructural locations. Thus, as compared to LCF where the majority of grains accommodate some plastic deformation, in HCF and VHCF it is likely that specific microstructural configurations can be associated with more rapid local fatigue damage accumulation. Such fatigue critical microstructural neighborhoods have been defined based on grain size [51], spatial orientation [51,60], proximity to the specimen surface [91,93], and crystallographic orientation [48,49].

In the regime of VHCF, researchers have noted the increased likelihood of subsurface

fatigue crack initiation in fatigue specimens. This has been attributed to a number of different factors, such as the presence of compressive surface residual stresses, the likelihood of finding a crack initiating defect in the specimen interior compared with the specimen surface, and the effect of environment. Current thinking and approaches in fatigue work indicate that the presence of microstructural regions capable of initiating fatigue damage determines where the fatigue crack will initiate.

### 2.3.1 Competing Mechanisms of Fatigue Failure

The fatigue behavior of commercial nickel and titanium-based alloys commonly exhibit bimodal distributions of lifetimes [60, 94–96]. This has been attributed to the interaction of surface and subsurface fatigue crack initiation [94], the distribution of fatigue critical defects [60], and the distribution of fatigue critical microstructural neighborhoods with varying levels of susceptibility to fatigue damage [96]. These approaches have been used to describe the range of fatigue lifetimes observed in different alloys, and these will discussed in this section. As these examples will indicate, different mechanisms of fatigue failure can be activated based on the stress level, loading conditions, material and testing environment being investigated.

Cashman has observed a bimodal nature in the fatigue lifetime curves of a nickel-based alloy, René 95 [94]. He attributes the bimodal distribution of lifetimes to the distribution of surface and subsurface fatigue crack initiation sites, in which the initiation sites were always found to be nonmetallic particles. In this work, lifetime is determined only by the location of the fatigue crack initiation site with respect to the specimen surface with the shorter lifetimes resulting from surface crack initiation. The work of Chandran and Jha explored the fatigue behavior of the titanium alloy Ti-10V-2Fe-3Al [60]. They found that the short lifetime distribution of failures could be modeled by applying Poisson defect statistics to the distribution of $\alpha_p$ clusters. Both of these examples highlight the paradigm

of thinking about fatigue critical microstructural regions as defects, which will certainly initiate a fatigue crack, if present within a given specimen.

Another approach to the issue of competing fatigue mechanisms is demonstrated with the strain-controlled fatigue experiments in Ti-6246 by Mahajan and Margolin [51]. They observed that at low strain levels, fatigue crack initiation is favored at $\alpha/\beta$ interfaces; while at higher strains, fatigue cracks initiate from slip bands that develop within the $\alpha_p$ grains, and this has been observed by other researchers [33,56]. These observations may simply be an artifact of the resolution limit of the experimental capabilities. That is, at high stresses, slip accumulation is expected to be more severe, leading to the development of slip steps within $\alpha$ grains. At lower stresses, strain accumulation will take longer, which will delay the formation of slip steps within grains. It seems reasonable that this process would lead to fatigue crack initiation from locations of strain incompatibility, i.e. $\alpha/\beta$ interfaces. This finding is similar to the current understanding of competing mechanisms of fatigue failure in the field of very high cycle fatigue (VHCF) in which a bimodal distribution of lifetimes is attributed to "'multistage"' S-N plots. Mughrabi [34,97] has developed the idea that the step-like nature of these fatigue curves is related to the threshold stresses required to activate fundamental physical mechanisms of fatigue damage accumulation, such as persistent slip bands (PSBs) and localized slip irreversibility.

Jha proposed a mechanism to explain the dual nature of fatigue lifetimes at each stress level [95], which is supported by others [98]. This model is consistent with the theory of competing fatigue mechanisms in the regime of VHCF, but he also develops the model to describe the effect of microstructural variability in these processes. In the first mechanism causing failure, slip accumulates in a few $\alpha_p$ grains and is transferred to the $\beta$ matrix. At this point, a crack is assumed to have been initiated. The other mechanism consists of strain accumulation in $\alpha_p$ grains and a subsequent homogenization step in which other nearby $\alpha_p$ grains accumulate strain. Fatigue crack initiation only occurs when the strain within

the $\alpha$ grains has saturated to the point where they can no longer accumulate more strain. This model implicity incorporates the effect of local microstructural neighborhoods where cyclic deformation accumulates, i.e. some neighborhoods have multiple $\alpha_p$ grains capable of accumulating damage, while other regions have cracks initiating from only one $\alpha_p$ grain.

The concept of competing mechanisms has been refined in more recent work by Jha and Larsen, with the idea that multiple levels of microstructural heterogeneity are responsible for the observed fatigue curve [96]. In this model, the effect of various microstructural configurations is explicity incorporated to describe how damage accumulates between the constituent microstructural phases. A ranking of these fatigue critical regions in order of increasing fatigue resistance is presented in Figure 2.15(a-d). This order also ranks the increasing probabilities of observing these specific neighborhoods within a given microstructural volume. For example, the configuration illustrated in Figure 2.15(a) is the most severe microstructural configuration, and leads to the shortest fatigue lifetimes, but has the smallest probability of being observed. The longest lifetimes are observed when the level of heterogeneity is only limited to one grain diameter, as shown in Figure 2.15(d). It should be noted that configurations (a) and (b) were only observed to initiate subsurface failures, while (c) and (d) were not associated with subsurface initiation sites. Jha and Larsen propose that if the rare, but microstructurally severe, configurations depicted by Figure 2.15(a) and (b) existed at the specimen surface, they would trump the presence of configurations (c) and (d) and result in the worst-case fatigue lifetimes. Thinking about this from another perspective, if microstructural configurations (a) and (b) could be eliminated from the material, a fatigue crack would be forced to initiate from configurations such as those depicted in (c) or (d) within the specimen interior and presumably, the fatigue lifetime would be longer.

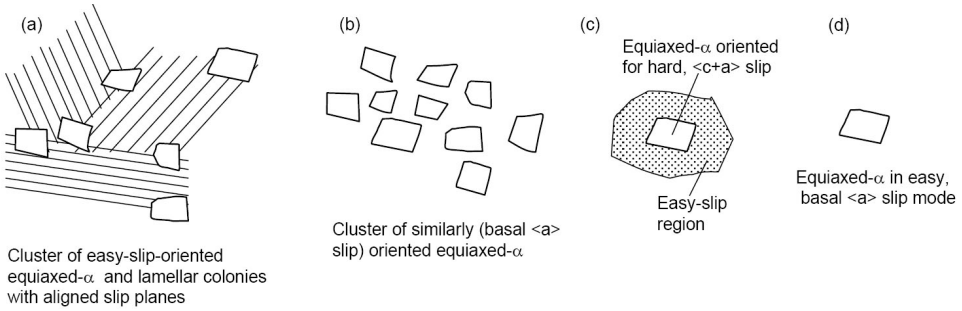


**Figure 2.15:** A schematic representation of the different levels of microstructural heterogeneity in a duplex titanium alloy.

### 2.3.2 Surface vs. Subsurface Fatigue Crack Initiation

Cracks have been observed to initiate at both surface and subsurface locations and this is often related to loading conditions and testing environment [44, 52, 95, 99]. At high stresses, fatigue crack initiation at slip bands is the preferred initiation location and slip bands are typically observed at the surface. However, at lower stresses, the mechanism of fatigue crack intiation has been observed to shift to the specimen interior. However, the work of Gilbert and Piehler [61] is an example where local microstructure overrides the effect of testing conditions on the fatigue crack initiation mechanism and location. They observed some cracking in subsurface regions under cyclic bending and this was attributed to the local grain orientations. This example highlights the significance of local microstructural neighborhoods in the process of fatigue crack initiation. None of the fatal fatigue cracks initiated from these subsurface locations, however an arrangement conducive to slip transfer was found. Further development of this paradigm for thinking of fatigue crack initiation has been spurred by the work of numerous groups [24, 30, 37, 48, 49, 74] who have examined the effect of the local texture on the fatigue crack initiation and growth processes. Generally, the finding is that regions of material suited for basal and prism slip are the crack initiation sites in these $\alpha + \beta$ titanium alloys.

## 2.4 Ultrasonic Fatigue

Researchers have long been working to accelerate fatigue testing by increasing the test frequencies. Ultrasonic fatigue techniques operating at 20 kHz were first employed in the 1950's [100]. Higher test frequencies of 100-200 kHz were subsequently achieved, but as the frequency is inversely proportional to specimen length, frequencies of 20 kHz are the practical limit for investigations of structural materials. Testing in the megahertz frequency range is used in the electronics industry to characterize MEMS devices. This section will discuss the principles of operation of ultrasonic fatigue equipment and the equivalence of data with conventional frequency fatigue.

The velocity of a wave in of a smooth cylindrical bar of constant diameter is given as

$$k = \sqrt{\frac{E}{\rho}} \tag{2.4}$$

The equation for the first mode of vibration is then

$$u(x,t) = A_o cos(kx) sin(\omega t) \tag{2.5}$$

The amplitude at any point $x$ along the bar is shown in Equation 2.6,

$$A(x) = A_o cos(kx) \tag{2.6}$$

where $A_o$ is the amplitude at the end of the bar and

$$k = \sqrt{\frac{\pi}{l}}, \omega = \frac{\pi c}{l} \tag{2.7}$$

The strain ($\epsilon$) at each point is given by Equation 2.8 where

$$\epsilon(x,t) = -kA_o sin(kx) sin(\omega t) \tag{2.8}$$

Using Equations 2.4 and 2.7,

$$l = \frac{1}{2f}\sqrt{\frac{E_d}{\rho}} \tag{2.9}$$

where $f = \omega/2\pi$, $l$ is the wavelength of the acoustic pulse, $\rho$ is the density of the material, and $E_d$ is the dynamic elastic modulus. The load train components used in ultrasonic fatigue need to be designed with consideration of this resonance length to ensure that the amplitude of the acoustic pulse is not attenuated.

### 2.4.1 Frequency Effects in Fatigue

The effect of frequency on the fatigue behavior of both pure metals [101,102] and commercial alloys [103–105] has been investigated by many researchers. Some materials exhibit longer fatigue lifetimes when tested at ultrasonic frequencies as compared to the fatigue lifetimes observed at conventional frequencies. The difference in lifetimes observed using conventional and ultrasonic frequency techniques is generally attributed to either a strain rate effect [105] or the time dependent effects of testing environment such as humidity [106], temperature [102], and atmospheric exposure [107].

In some cases, titanium alloys exhibit a frequency effect, but in other cases the data acquired at conventional frequencies and ultrasonic frequencies have equivalent lifetimes. For example, Ritchie and coworkers did not observe a frequency effect in Ti-6Al-4V between 50 Hz and 1 kHz [85–87]. Furthermore, tests conducted by Davidson at 1.5 kHz on the same material exhibited essentially unchanged fatigue crack growth rates in air, but vacuum crack growth rates were 3 orders of magnitude slower than air [83]. The next two sections will discuss the effects of frequency on fatigue that arise from the strain rate effects and environmental effects.

#### 2.4.1.1 Strain Rate Effects

Roth et al. [102] proposed that materials with few primary slip systems exhibit a larger strain rate effect than those with many primary slip systems. Namely, FCC materials exhibit little or no strain rate effect, while HCP and BCC materials, with their relatively few slip systems have a larger effect. Roth and co-workers also state that variation in specimen temperature will have a substantially larger effect on the observed fatigue lifetime than variations due to strain rate effects. Some researchers have also speculated that the strain rate effect can be exacerabated in two-phase materials such as Ti-6Al-4V due to the frequency dependence of the incompatibility stresses at the $\alpha/\beta$ interface [103]. Holper et al. [106, 108] have investigated the effects of environment and frequency in aluminum alloys, and their results agree that no frequency effect is attributable to the strain rate.

#### 2.4.1.2 Environmental Effects

Recent work in cast aluminum alloys has investigated the effect of environment on the fatigue lifetime at ultrasonic and conventional frequencies [107]. Zhu and co-workers found that the frequency effect could be accounted for by considering the effects of environmental exposure. Wanhill observed a frequency effect on the fatigue crack growth rates of Ti-2.5Cu, which was related to the testing environment [109]. Aqueous environments of distilled water and 3.5% aqueous NaCl were observed to have detrimental effects on the fatigue performance. A number of researchers [110–112] investigated the fatigue crack growth rates of Ti-6246. Again, in these experiments, environments containing water vapor have a deleterious effect on fatigue behavior in this alloy, and that effect is accentuated at high temperatures of 500°C. Tests were run at a number of different frequencies in various environments, and the same effect was observed in humidified argon, which indicates that water vapor is the deleterious species.

Peters et al. [24] studied the effect of texture on the fatigue behavior of Ti-6Al-4V. Texture was observed to affect the fatigue behavior of this alloy in corrosive environments. That is, 3.5% NaCl and lab air exhibited accelerated fatigue crack growth rates when the crack growth direction was parallel to the (0002) planes. The faster crack growth rates on these planes was attributed to enhanced environmental susceptibility along these crystallographic directions.

## *2.5 Summary*

The purpose of this section is threefold: to provide a summary of the observed fatigue crack initiation mechanisms, to relate these mechanisms to fatigue critical microstructural features, and to identify the remaining questions regarding cyclic deformation in $\alpha + \beta$ titanium alloys. To do this, it is first necessary to define what is meant by fatigue crack initiation. The best definition to use is from Hall [31], where a fatigue crack is determined to have initiated when it begins to propagate as predicted by small fatigue crack growth laws. Depending on the resolution of the experimental techniques used and the objective of the study, researchers have attributed fatigue crack initiation to a variety of mechanisms, such as pseudo-cleavage [44, 113, 114], slip band crack initiation [51], grain boundary crack initiation [54], damage homogenization [95], or crack coalescence in microtextured regions [48]. However, these mechanisms all appear to result from either of two fundamental physical processes. That is, for a crack to form, dislocations must ultimately enable the formation of crack initiating slip bands within grains, or dislocation pile-ups at grain boundaries will cause fatigue cracks to initiate as a result of a strain incompatibility between adjacent grains. The specific mechanism being activated will depend on microstructural morphology, size, and the ability of these fatigue critical neighborhoods to accommodate cyclic slip accumulation. The regime of very high cycle fatigue is unique, since only specific microstructural locations will be susceptible damage accumulation and

hence fatigue crack initiation. Therefore, damage will be localized in only those localized neighborhoods that present the least resistance to fatigue damage accumulation. In summary, fatigue crack initiation results from either of two fundamental physical processes: a mechanism of cyclic strain incompatibility or cyclic strain accumulation. Both of these processes result from the accumulation of the irreversible portion of cyclic slip in specific microstructural locations. The remainder of this section will summarize the effect of microstructure and loading conditions on the activation of these mechanisms.

As this chapter discussed, there are a variety of microstructural features and locations that are reported to initiate fatigue cracks. These features range in size from individual lath $\alpha$ needles [36] to large $\alpha_p$ grains [51] and even up to large microtextured regions [48, 62]. The features responsible for fatigue crack initiation depend on their prevalence within the microstructure, their size relative to other microstructural features and the loading conditions being applied. For example, many studies have focused on low cycle fatigue or dwell fatigue, which enhances the number of microstructural neighborhoods that may contribute to fatigue crack initiation. Under these loading conditions, in colony or $\beta$ processed microstructures, the pseudo-cleavage mechanism is often cited as the mechanism of fatigue crack initiation to explain the presence of facets oriented perpendicular to the tensile axis, and the investigation of this mechanism has been the explicit focus of a few fatigue studies [44, 62, 113, 114]. Others have observed that microtextured regions are responsible for fatigue crack initiation under dwell-time loading [30, 62].

It remains to be determined what specific microstructural features are associated with worst-case fatigue lifetimes in the very high cycle fatigue regime where the applied stresses are nominally elastic and only the most severe microstructural locations will be susceptible to fatigue crack initiation. A number of other questions related to the mechanism of fatigue crack initiation have still not been resolved in the literature. In the case of fatigue crack

initiation from clusters of $\alpha_p$ grains or microtextured regions, fatigue critical microstructural volumes have been identified, but it is not clear how strain accumulates and transfers among the microstructural features in these regions or what length scale is significant in the operation of these mechanisms. Additionally, due to the Burgers orientation relationship that exists in titanium alloys, it is possible that slip can transfer between the $\alpha$ and $\beta$ phases. This has been observed in the monotonic deformation behavior of these alloys [19, 20], but it is not clear if this mechanism of slip transfer also applies to cyclic loading. Specifically, does the presence of microtextured regions enhance slip transfer from the $\alpha$ to the $\beta$ grains to initiate fatigue cracks? Texture is known to affect the fatigue performance of these alloys, but no studies have attempted to address the effect of texture on both fatigue crack initiation and fatigue crack growth. These issues are addressed in this thesis.

# Chapter 3

# Material and Experimental Procedures

This chapter describes the materials investigated and the experimental techniques employed in this study. It is divided into three sections; material, fatigue testing, microstructural characterization and other experimental techniques used in this research.

## *3.1 Material*

The material investigated in this study is an $\alpha + \beta$ titanium alloy, with a nominal composition: Ti-6Al-2Sn-4Zr-6Mo (wt%), which is commonly referred to as Ti-6246. The specifications for this alloy are listed in Table 3.1. The $\beta$ transus ($T_\beta$) for this alloy is 927°C. The microstructure consists of equiaxed alpha grains in a transformed beta matrix. Although the exact thermomechanical processing steps are proprietary, the processing route used to produce this microstructure can be estimated based on the observed microstructure [11].

### 3.1.1 Forging and Heat Treatment Process

The ingot would have been produced by a VAR process, which may have been remelted multiple times to homogenize the composition and remove impurities. Subsequently, the material was initially forged in the $\beta$ phase field, at approximately 150°C above $T_\beta$, and

**Table 3.1:** The nominal composition of Ti-6246

| Al | C | H | Fe | Mo | N | O | Sn | Ti | Zr |
|---|---|---|---|---|---|---|---|---|---|
| 6.0 | ≤0.1 | ≤0.015 | ≤0.1 | 6.0 | 0.02 | 0.12 | 2.0 | 82.0 | 4.0 |

then fan-cooled. The material would then be reheated to approximately 30-50°C below $T_\beta$ and further hot worked. This step refines the microstructure by providing the driving force for recrystallization. The material is then reheated for a further reduction in the $\beta$ phase field and rapidly cooled. Following these $\beta$ homogenization steps, the material is worked in the $\alpha + \beta$ phase field. During this process, the microstructure is lamellar and the forging process breaks up the lath $\alpha$ phase. It is during this phase of the forging operation that the lath $\alpha$ undergo both dynamic and static spherodization to transform into equiaxed $\alpha_p$ grains. Following the forging and spherodization process, the final heat treatment steps are as follows: a two-hour soak at 921°C with an air/fan cool, a two-hour hold at 824°C with a water quench, and finally an eight-hour aging at 593°C with an air cool. The first of these steps is responsible for the formation of the lath $\alpha$, and the cooling rate is directly related to the lath width. The water quench following the 824°C treatment would produce a martensitic transformation within the $\beta$ phase. The aging step at 593°C relieves strain developed within the microstructure due to the martensitic transformation in the previous cooling step. This last step in the heat treatment process is responsible for toughening the $\beta$ phase by stabilizing the solid solution strengthening.

## *3.2 Fatigue Testing*

### 3.2.1 Specimen Design

Specimens were designed to resonate at approximately 20 kHz. The procedure was completed using numerical techniques to solve a wave equation of the form shown in Equation 3.1, where u = u(x,t) is the displacement in the longitudinal (x) direction. A is the cross-sectional area and A' is the derivative of A, $\rho$ and E are the density and modulus of the specimen, respectively [115]. Equation 3.1 is solved iteratively to represent the three portions of fatigue specimens: the straight gage section, the curved end of the gage, and the shoulder region leading to the grips.

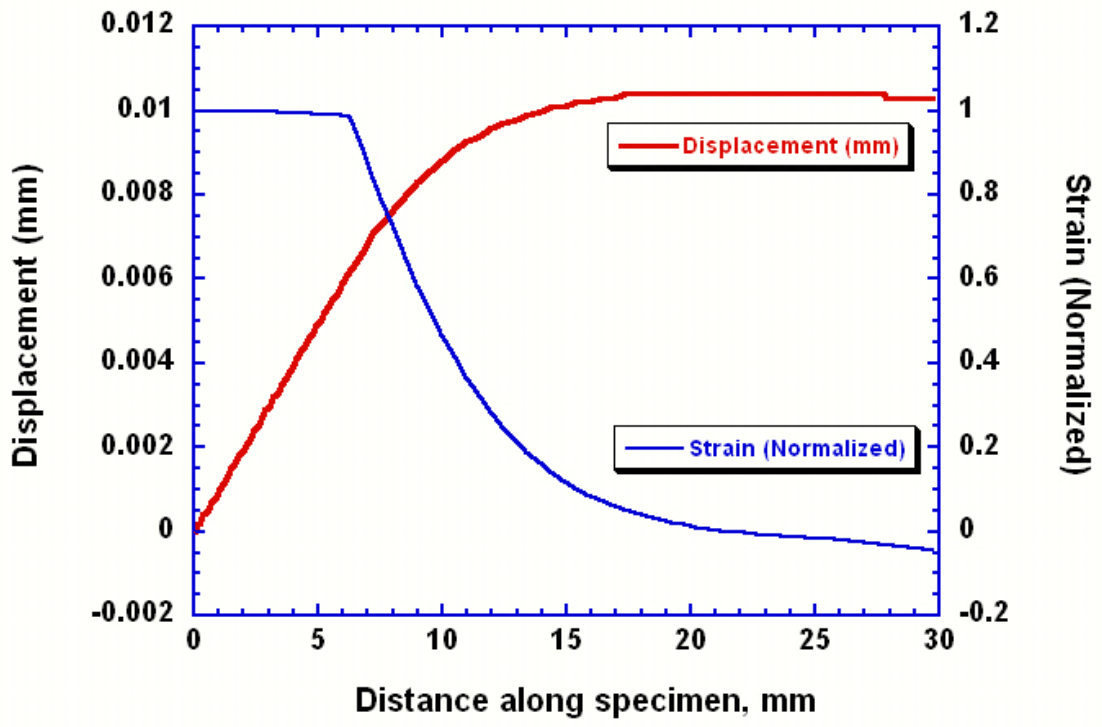


**Figure 3.1:** A plot of the strain and displacement as a function of position along the specimen axis for Ti-6246.

$$u'' + (A'/A)\,u' + \omega^2\,(\rho/E)\,u = 0 \tag{3.1}$$

This results in the sharp discontinuities observed in the plot of the normalized strain. As shown in Equation 3.1, the resonant frequency depends on the modulus to density ratio. Figure 3.1 is a plot of the strain and displacement as a function of position along the specimen. Due to symmetry, Equation 3.1 only has to be solved for one half of the specimen. As the plot shows, the strain (plotted on the right ordinate) is nearly constant through the specimen gage (6 mm) and then decreases through the shoulder and grip regions. The center of the specimen (0 mm) corresponds to a displacement node and the ends of the specimen are displacement maxima, which corresponds to a strain node.

### 3.2.2 Specimen Preparation

Smooth bar fatigue specimens were used for both S-N type tests and small fatigue crack growth tests. Specimens were cut with their axes aligned circumferentially from a forged pancake and a retired disk. The forged pancake component was processed to simulate the microstructure observed in actual components and the microstructural characterization results will be discussed in Section 4.1. Cylindrical specimen blanks were extracted from the large volumes of material, and grip ends of Ti-6Al-4V rod were inertia welded onto the specimen blanks. Final machining of cylindrical specimens was completed by low stress grinding to minimize compressive residual stresses [116]. A part drawing of the sample is shown in Figure A.1. Specimens were designed specifically to resonate at approximately 20 kHz to enable the use of ultrasonic frequency fatigue techniques. The specimen gage is nominally 4 mm in diameter and 12 mm in length.

All specimens were electropolished to remove the remaining surface compressive residual stresses. Approximately 100 $\mu$m of material was removed from the specimen surface. The electrolyte used was 59% methanol, 35% ethylene glycol monobutyl ether (butyl cellosolve), and 6% perchloric acid. A schematic of the electropolishing setup is shown in Figure 3.2. A one liter beaker was filled with the electrolyte and cooled to approximately -40°C using a cooling bath of isopropanol. A Neslab Cryocool CC-100II Immersion Cooler unit was used to cool the isopropanol. Periodically, liquid nitrogen was added to the electrolyte to maintain the temperature at -40°C. It was necessary to do this in between every specimen that was polished, since the Neslab Cryocool unit could not handle the thermal load of the electropolishing setup. The cooling bath of isopropanol was contained in an Agitainer unit, which stirs and insulates the cooling solution. Within the one liter beaker, a cylindrical stainless steel (316L) cathode was used, and specimens were attached to a motor

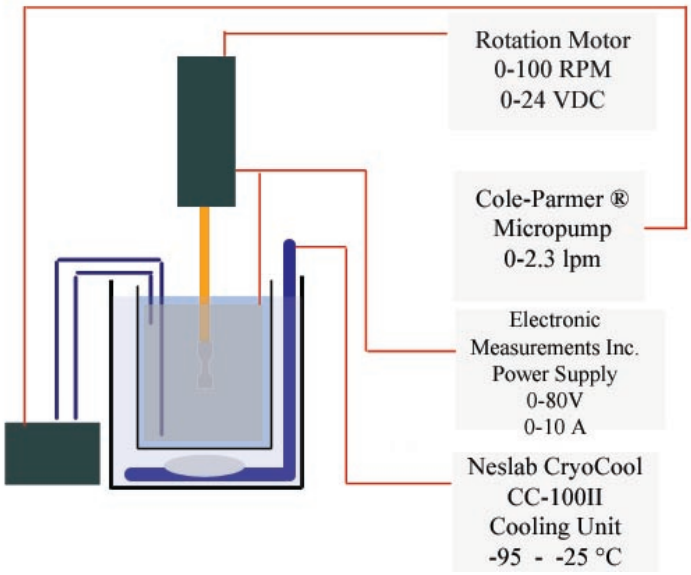


**Figure 3.2:** A schematic of the electropolishing setup.

to rotate them at approximately 2-3 rpm to ensure that material removal was uniform. Additionally, the electrolyte was agitated by pumping it through a Cole-Parmer MicroPump with polytetrafluoroethylene (PTFE) gears and tubing. The electrolyte was pumped at a rate of 1.5 liters/minute to ensure that no thermal gradients developed in the solution. The power supply was set to control the potential at 40 V, and the current was allowed to fluctuate as a function of the electrolyte temperature and condition. With every new batch of electrolyte, a rod of Ti-6Al-4V was polished for 10-20 minutes to condition the electrolyte and introduce titanium ions into the solution.

### 3.2.3 Fatigue Crack Growth Test Specimens

Smooth bar fatigue specimens were modified for use in small fatigue crack growth studies. Flats were machined on opposing sides of the specimens to maintain symmetry and to prevent any bending stresses from developing. Approximately 5 micronotches, which served as the initiation sites for fatigue cracks, were machined on each of these flats using a femtosecond-pulsed laser or using a focused ion beam (FIB) microscope. While specimens

machined with the laser provided reasonable fatigue crack growth rates, smaller notch sizes were desired to probe the effects of local microstructural volumes on fatigue crack growth rates. For this purpose, a Nova NanoLab FIB microscope was employed to machine micronotches ranging from 15 - 35 $\mu$m surface length (2c) in fatigue specimens. In all cases, the ratio of notch dimensions c:a=1 was used to approximate a semi-elliptical shape, which enables the application of standard stress intensity solutions [117]. Parametric studies have been completed to ensure that machining conditions used in this study would produce micronotches with the desired depth.

#### *3.2.3.1 Femtosecond-pulsed Laser Micromachining*

A femtosecond-pulsed laser was used to place surface defects in specimens while avoiding the introduction of deleterious effects in the microstructure surrounding the defect. This allows for the study of small crack growth rates that are not influenced by the process of machining defects in the material [118]. The femtosecond laser setup is shown in Figure 3.3, and the main components in this setup consist of the laser, optical density filters for controlling laser power, a four axis stage, a 350 mm planoconvex lens and a 50 mm planoconvex lens. The position of the laser beam is fixed in this setup, and the fatigue specimen is attached to the stage. Machining is completed by moving the specimen into the focal point of the laser. The laser beam is produced by a Clark-MXR CPA 2000, which is a Ti:sapphire chirped pulse laser operating at 1 kHz repetition rate of 150 fs pulses. The wavelength is 780 nm, and the initial laser power is approximately 800 mW. With optical density filters in the beam path, the power was reduced to 2.8 mW. A fast-acting shutter was placed in the beam path to regulate the laser dosage. To machine the micronotches, 200 shots were used to ablate conical volumes of material from the specimen. The diameter of the ablated spot as measured at the specimen surface was typically 30 $\mu$m. The four axis stage has a resolution of 0.5 $\mu$m, which allows for fine control over the location and

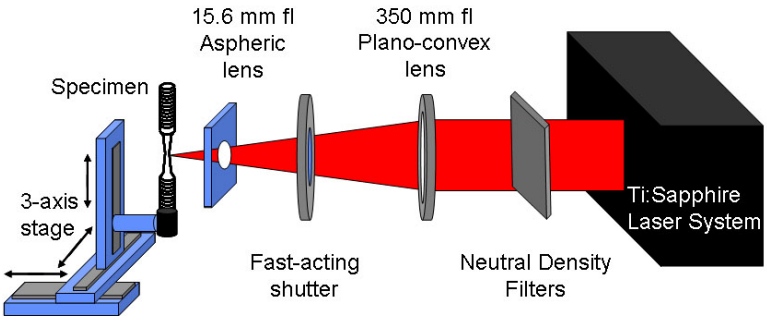


**Figure 3.3:** A schematic of the femtosecond-pulsed laser setup used for machining micronotches in fatigue crack growth specimens.

shape of the notch. The spacing between laser shots was 10 $\mu$m and this setting produced micronotches that appeared continuous as shown in Figure 3.4a.

#### *3.2.3.2 FIB Micromachining*

In these specimens, five notches were machined on each flat, resulting in ten notches for every specimen. An ion probe current of 2.8 or 6.5 nA was used, depending on the size of the notch to be machined. The lowest probe current providing a reasonable machining time was used to minimize gallium ion implantation. Additionally, the accelerating voltage of the ion beam was set to 30 kV. A representative notch machined with this technique is shown in Figure 3.4b. The notches produced with this technique are clearly smoother and more well-defined; however the machining time is longer than that required for the femtosecond laser ablation. In cases were the machining time is not prohibitively long, the FIB is the preferred method for machining micronotches.

## *3.3 Ultrasonic Fatigue Tests*

Axial fatigue tests were completed using ultrasonic fatigue equipment operating at 20 kHz and a load ratio of 0.05 at room temperature in laboratory air. Also, a block loading cycle of 350 ms/900 ms pulse/pause was used to prevent heating of the specimen. Thermocouples were used to verify that the specimen surface temperature did not vary by more than ± 3 °C.

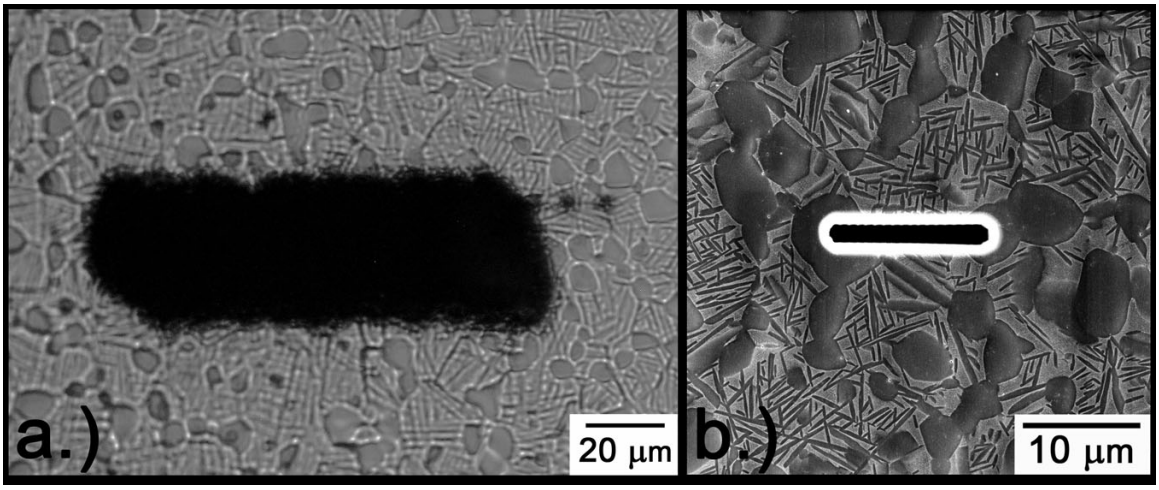


**Figure 3.4:** Example micrographs of the notches that were machined in fatigue specimens using a.) a femtosecond-pulsed laser and b.) a focused ion beam microscope.

A schematic of the ultrasonic fatigue system is shown in Figure 3.5. The acoustic pulse responsible for driving the fatigue specimen in resonance is generated by the piezoelectric transducer. The acoustic signal from the ultrasonic transducer is amplified by the booster horn and then travels through the lambda rod down to the specimen. As shown in Figure 3.5, the ultrasonic load train is mounted in an MTS load frame, which allows for the static application of a mean load [115, 119]. The MTS load frame is controlled with a MTS 458.20 Microconsole controller using a 10 kN range card. The actuator arm shown below the specimen in the load train is used to apply this load. The ultrasonic fatigue system has been specifically designed so that this actuator arm applies a load at a displacement node to prevent damping of the ultrasonic pulse. This displacement node is determined by the resonance length, as shown in Equation 2.9, and can shift due to variations in specimen design, material, and temperature. Therefore, the load train components are designed using the equations in Section 2.4, but generally must be modified through a process of trial and error to determine the proper setup and minimize damping of the acoustic pulse. It should be noted that the soundness of the connections between the hardware used in this system is very important, since loose connections will result in damping of the ultrasonic pulse.

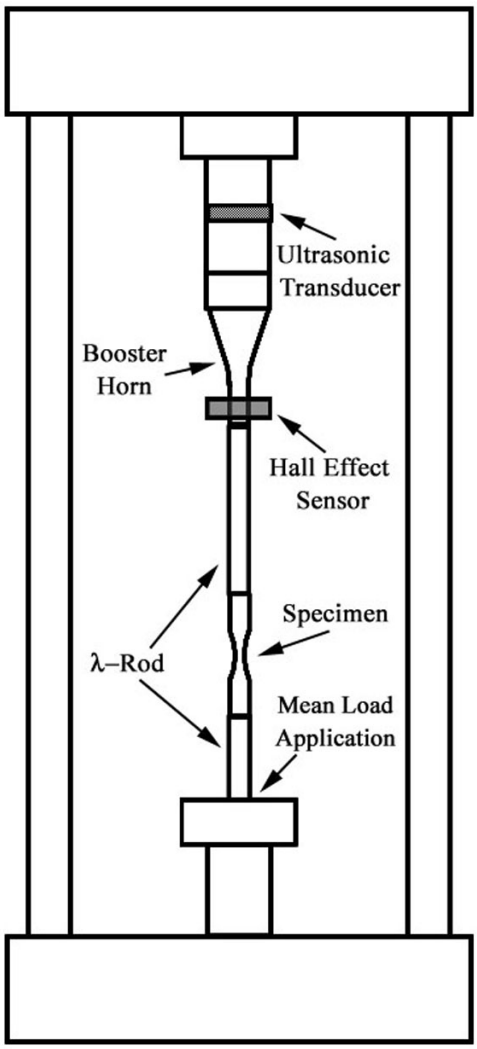


**Figure 3.5:** A schematic of the ultrasonic fatigue test frame, which has been assembled within an MTS load frame for application of mean loads.

Fatigue tests are run in displacement control, with feedback provided by the Hall Effect sensor. The control unit sends a command voltage to the ultrasonic transducer, and the Hall Effect sensor monitors displacement within the load train. The control unit continues to send maximum power to the piezoelectric transducer until the displacement measured by the Hall Effect sensor matches the amplitude set with the control unit. At this point, the specimen is in resonance at the specified stress amplitude and the command voltage sent to the ultrasonic transducer is decreased to a point that is sufficient to maintain resonance in the specimen. The control unit can drive the ultrasonic transducer at low duty cycles to limit heating of the specimen. Additionally, compressed air and cooling fans were directed at the specimen to prevent specimen heating.

Due to the slight variations in specimen dimensions and soundness of the connections between load train hardware, it is necessary to calibrate the system before each fatigue test. Kyowa strain gages with a gage length of 1 mm were applied to fatigue specimens using plastic cement, and all fatigue specimens are instrumented with these gages to measure the ultrasonic (i.e. dynamic) portion of the fatigue cycling. Specimens are cycled at low amplitudes, well within the elastic regime of loading to determine the slope of the command voltage vs. strain curve. Since the stresses used to test the samples were in the range of 0.4 to 0.6 of the yield stress, it is assumed that the cyclic loading is nominally elastic. Therefore, the set point for the testing amplitude of the command signal was determined by extrapolation of this curve. This calibration is verified using a Fotonic® displacement sensor, which can measure displacements with a resolution of 0.3 $\mu$m. The fatigue setup is aligned to the specification that there be no more than 5% bending strain. The specimen used for alignment has twelve strain gages attached to it in three rows, and four columns which are separated by 90° around the specimen circumference. This specimen enables alignment of the load train in terms of concentricity and angularity. This procedure is completed approximately every three months or more often if the experimental configuration is

significantly altered.

### 3.3.1 Validation of Ultrasonic Fatigue Calibration Procedure

One assumption that is made with the calibration procedure is that it is accurate to extrapolate the strain measured at low amplitudes as the means for determining the pulse amplitude at the testing strains. This cannot be verified by the strain gages used to calibrate the machine before every fatigue test, since the gages are damaged at strains of approximately 1000 $\mu\epsilon$ and tests are completed with strain amplitudes in the range of 2500 $\mu\epsilon$.

An interferometric strain displacement gage (ISDG), for measuring the strain directly from the specimen, has been developed to operate at kilohertz frequencies [120]. This technique relies on the use of photomultiplier tubes to measure the shift of interference fringes, as depicted in the schematic in Figure 3.6. Interference patterns are created by the interaction of the incident laser beam with either hardness indents or platinum markers on the specimen surface. The intensity of the interference fringes can be represented by Equation 3.2, where $I_o$ represents the maximum intensity, d is the spacing of the indents or markers, $\alpha_o$ represents the solid angle between the specimen and the detector, and $\lambda$ is the wavelength of the laser. The shift in the interference fringes is described using Equation 3.3, where d changes due to the measured variation in intensity, and by dividing d by the initial gage length, $d_o$, the stran is calculated. The minimum theoretical strain that can be measured with this approach can be determined using Equation 3.5, where $\Delta$m represents fringe shift, and $\epsilon$ is the strain. The helium-neon laser has a wavelength ($\lambda$) of 0.6328 $\mu$m, $d_o$ is 200 $\mu$m, and $\alpha_o$ is on the order of 45°. If a 1/1000th shift of a fringe is detectable, the minimum attainable strain measurement will be 0.447 $\mu\epsilon$. There are a number of advantages to using this technique, as it is a non-contact method for real-time strain measurement that can operate at high temperature. Thus, with the use of megahertz-speed data acquisition cards, it is possible to measure and capture strain at kilohertz frequencies used in ultrasonic

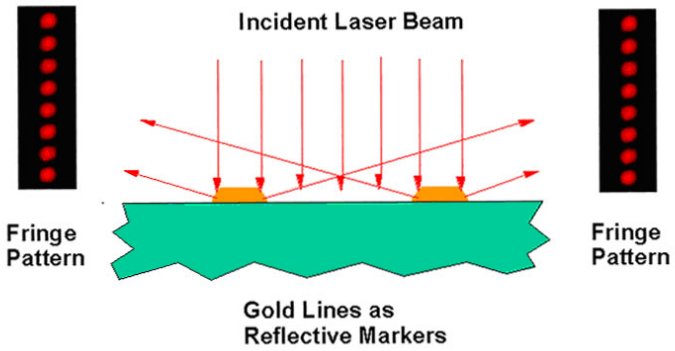


**Figure 3.6:** A schematic of the ISDG technique in which interference fringe movement is measured with photomultiplier tubes allowing for real time strain measurement directly from the specimen surface. After [120]

fatigue. A representative plot illustrating the agreement of the strain measured with resistance gages, and as measured with the ISDG technique, is shown in Figure 3.7. This plot demonstrates that the practice of extrapolating the amplitude setting to high strains is valid for the regime of fatigue behavior that is being investigated in this study.

$$I = I_o cos^2 \left(\pi d sin\alpha_o / \lambda\right) \tag{3.2}$$

$$d = cos^{-1} \left(I/I_o\right)^{1/2} / K \tag{3.3}$$

$$K = \pi sin\alpha_o / \lambda \tag{3.4}$$

$$\epsilon = \Delta m \lambda / d_o sin\alpha_o \tag{3.5}$$

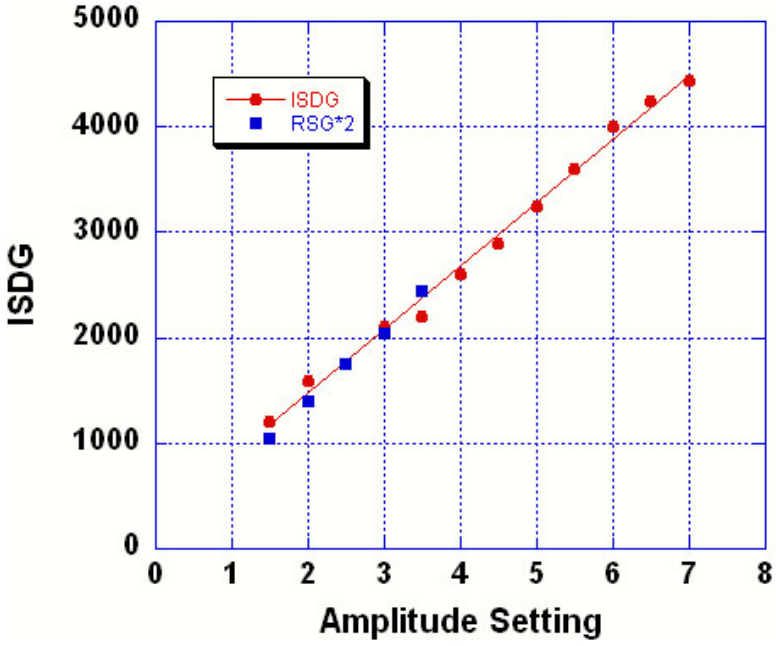


**Figure 3.7:** A plot comparing the strain measured by the ISDG and the resistance strain gages. After [120]

### 3.3.2 Ultrasonic Fatigue Crack Growth Tests

Surface lengths of fatigue cracks were measured with two different techniques. In some cases, crack lengths were measured optically, and in other specimens cracks were measured by surface replication. Flats were required in the case of optical crack measurement to ensure that the specimen surface and the focal plane of the telescope are co-planar. To measure crack length, digital images were acquired using a Questar QM100 telescope with a Dage MTI RC-300 CCD camera. The images were acquired on a PC using the National Instruments IMAQ Vision Builder software.

In fatigue specimens with multiple micronotches, surface replicas were made with acetate tape. Replicas were made every 2,000 - 3,000 cycles, once a crack was observed to have initiated. This method is preferred, since it provides a record of the entire specimen surface while providing better resolution than the optical measurement technique. Replicas were viewed with an Olympus PME3 optical microscope instrumented with a graticule and

stage micrometers for accurate crack length measurement.

### 3.3.3 Analysis of Fatigue Crack Growth Data

Fatigue crack growth data are presented in the typical da/dN vs. ΔK format. The measured growth rates have been smoothed with a three point sliding average to reduce the variability in growth rates resulting from measurement frequency. The stress intensity factor range, ΔK, was calculated from the analytical solution presented by Newman and Raju [117]. This solution for the stress intensity assumes that a surface crack is growing in a semi-infinite plate. For the micronotches that were machined in this study, this is a reasonable assumption, and the data generated with this approach will be presented in future sections. Since the depth of the crack could not be directly measured, it was assumed that the crack advanced according to c/a =1.

The behavior of fatigue cracks is assumed to follow a power law equation of the form shown in Equation 3.6. The constants, C and m, are measured from a fit of the fatigue crack growth curves. These constants are used to predict the crack growth portion of fatigue lifetimes using Equation 3.7, where $a_i$ and $a_f$ represent the initial and final crack size, respectively.

$$\frac{da}{dN} = C\Delta K^m \tag{3.6}$$

$$N_f = \int_{a_f}^{a_i} \frac{1}{C\Delta K^m} \tag{3.7}$$

## *3.4 Microstructural Characterization*

### 3.4.1 Sample Preparation

Metallographic samples were prepared by typical mechanical polishing techniques. Samples were mounted in Buehler Konductomet resin in preparation for scanning electron

microscopy (SEM) investigations. For optical microscopy specimens, the samples were mounted in Buehler CastoLite epoxy. The castolite epoxy was used in cases where it was necessary to extract the sample from the mount after polishing. Only if the sample needed to be examined in an SEM was the Konductomet mounting resin used. Typical polishing procedures were used, with grinding on successively finer grit silicon carbide papers being conducted from 60 grit up through P2400 grit. Polishing was completed using alumina slurries of 1 $\mu$m, 0.3 $\mu$m, and 0.05 $\mu$m with Buehler TEXMET pads. Some samples were etched using Krolls reagent: 4 ml hydrofluoric acid, 4 ml nitric acid, and 100 ml distilled water by swabbing the surface for 5 seconds and rinsing with methanol.

Fractured samples were examined by SEM, and for this analysis the shoulder and grip ends of the fatigue specimen were cut off. The resulting piece was a cylinder, approximately 3-6 mm tall containing the fracture surface, as shown in Figure 3.8. Additionally, some of the samples that failed by subsurface fatigue crack initiation were sectioned to examine the material near the site of fatigue crack initiation. The plane of sectioning is annotated as plane B-B in the schematic shown in Figure 3.8. The specimen was first examined in the SEM, and the distance between the crack initiation site and the specimen surface was measured. The specimen was then mounted in epoxy for grinding and polishing using the polishing procedure outlined above. Material removal was monitored with a micrometer. As the desired depth was approached, a final polishing step in a Buehler Vibromet 2 was completed to provide a residual stress-free surface suitable for OIM investigation. Vibratory polishing was completed using Allied 0.05 $\mu$m noncrystallizing colloidal silica on a nylon pad. Specimens were polished for 3 hours, and in this time 1-3 $\mu$m of material was removed. The specimen was then extracted from the Castolite epoxy mount by dissolving the mount in acetone overnight. By extracting the samples from the mount, it was possible to view both the fracture surface and the material at the site of fatigue crack initiation simultaneously in the SEM.

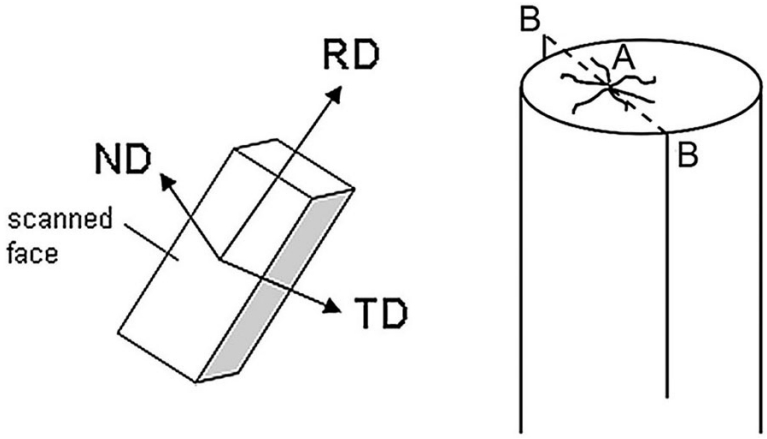


**Figure 3.8:** A schematic depicting the sectioning plane of fractured fatigue samples and the reference frame for OIM scans.

### 3.4.2 Optical Microscopy

An Olympus PME3 inverted optical microscope was used to examine the microstructure. Digital images were acquired, and these were used to measure the grain size and volume fraction of the $\alpha_p$ phase.

### 3.4.3 Scanning Electron Microscopy

Observation of metallographic sections and fracture surfaces was completed using two scanning electron microscopes: a Leica Cambridge S360FE and a Phillips XL30FEG. Both microscopes have a field emission gun electron source. The Leica operates at a probe current of 100 pA, accelerating voltage of 15 kV, and working distance of 15 mm. The XL30FEG is used with accelerating voltage of 10 kV with a probe current of approximately 2 nA and a working distance of 10 mm. Both microscopes are equipped with a 4 Pi image acquisition system that enables the acquisition of very high resolution electron micrographs. Additionally, EBSD detectors are installed on both of these microscopes.

Orientation imaging microscopy (OIM) was completed on metallographic specimens and on polished sections of the fractured fatigue specimens using these two microscopes

with detectors manufactured by EDAX-TSL. For OIM investigations, the probe current and accelerating voltage were approximately 10 nA and 20 kV, respectively. Samples are oriented at 70° with respect to the stage normal position at working distance of 25 mm. With well polished samples, frame rates of 58.8 frames per second were achieved. This setting was employed whenever practical, so as to maximize the size of the scan area, improve scan resolution, or to reduce the scan time. Step sizes of 0.2 $\mu$m were used as the coarsest step size, since this still permitted observation of the morphology of equiaxed $\alpha_p$ grains and lath $\alpha$. For very high resolution scans, a step size as low as 0.05 $\mu$m was employed, and this step size was adjusted based on time available for scanning. OIM scans were completed on the region of material just below the fracture surfaces at the site of fatigue crack initiation. The section of material that was exposed for OIM analysis is depicted as plane B-B in Figure 3.8. Figure 3.8 also illustrates the reference frame for OIM scans. The OIM scans have been acquired in the RD-TD plane, with RD corresponding to the tensile axis of the fatigue specimens.

OIM batch scans were collected from metallographic samples using a stage automation procedure to control the microscope stage and the OIM data collection software, which was written in-house at AFRL. This LabView program enabled the collection of areas as large as 1.7 x 1.5 mm with a resolution of 0.5 $\mu$m in a single weekend run.

### 3.4.4 Stereo Fractography

The spatial orientation of facets was measured with respect to the loading axis using stereology. Images used to produce 3D reconstructions of fracture surfaces were acquired in the SEM by centering the feature of interest in the field of view at the eucentric height. Images were then acquired at tilt angles of 0° and 6° with respect to the stage normal position for each facet. The technique and procedure for generating stereo pairs was validated using MeX commercial software (Alicona: Grambach, Austria) on known geometries such as

Vickers microhardness indents.

### 3.4.5 Grain Size and Volume Fraction Measurements

The grain size and volume fraction of the $\alpha_p$ phase were measured using manual techniques and verified with digital image analysis techniques. The grain size measurements were taken using the linear intercept method, while the volume fraction of the $\alpha_p$ grains was measured with the point count method.

### 3.4.6 Digital Image Analysis

The characterization of microstructure described above was also completed with digital image analysis techniques. This procedure was completed using the Image Processing Toolkit plugins written by ReindeerGraphics that integrate with Adobe Photoshop. The microstructural features were extracted from the micrographs by using the image processing algorithms including thresholding, erosion, dilation, and selection/rejection of features based on size and aspect ratio. Application of these algorithms in different order and to varying degrees was found to be a suitable means for separating the lath and equiaxed $\alpha$ phases. These tools were applied to micrographs acquired with EBSD techniques.

The texture separation procedure was applied to the EBSD scan tiles individually, but each of the scan tiles was montaged with the 8 adjacent tiles for prior to processing with this algorithm. That is, the process required montaging the 8 neighboring images with the tile of interest. This step was necessary to ensure that the aspect ratio and particle size feature-based filters were not erroneously applied in cases where an equiaxed $\alpha_p$ grain was on the edge of a scan tile. Then, the texture separation algorithm was applied to this group of 9 (image of interest + 8 nearest neighbors) images. Following the application of this procedure, the individual images are then cropped from the montage to yield only the image of interest. The individual scan tile is outlined in red as shown in the images in

Figure 3.9.

Figure 3.9 illustrates each step of the procedure that was followed to separate the lath $\alpha$ phase from the equiaxed $\alpha_p$ phase. To start with, a grayscale image is created from the OIM data using the image quality (IQ) parameter as shown in Figure 3.9a. The resulting image is a binary file in which the $\alpha_p$ grains are in the foreground (black), and the transformed $\beta$ matrix is the background (white). Each pixel in these figures correspond to an OIM data point, and hence each point has three Euler angles associated with it. The IQ parameter is a measure of the quality (sharpness of lines and contrast) of the Kikuchi pattern used to determine the crystallographic orientation of the material. This parameter typically varies between 0 and 150, which makes it suitable for representation with a grayscale image. Regions near grain and phase boundaries will naturally have lower IQ values, as the diffracting volume may have contributions from two different orientations and potentially different crystal structures. As shown in this image, the morphology of the phases is clearly observable in this pseudo micrograph, and the morphological differences between the lath and equiaxed particles can be used as the basis for phase separation.

Figure 3.9b illustrates the image after an auto leveling (histogram normalization) procedure is applied to take advantage of the full grayscale range. In this image, a difference in grayscale values is evident between the $\alpha$ (both lath and equiaxed) and $\beta$ phases. This is due to the presence of the $\alpha$ precipitates within the $\beta$ phase, which distort the bcc lattice and consequently lead to more diffuse Kikuchi patterns and hence lower IQ values. Figure 3.9c illustrates the image after it is thresholded to isolate the $\alpha$ phase material. The grayscale value selected for the thresholding procedure is determined by the user and typical values fall within the range of 140-160. Some of the low IQ values fall within features that are clearly $\alpha_p$ grains and are therefore eliminated during the thresholding procedure. Therefore a hole-filling routine is employed and this is shown in Figure 3.9d. Figure 3.10e displays

the image following an erosion of the remaining particles and this step successfully removes most of the lath $\alpha$ phase. The image is then treated with a filter to remove particles containing less than 40 pixels or those having an aspect ratio of greater than 4:1, as shown in Figures 3.10f and 3.10g, respectively. The final step of the phase separation process is a grain dilation to readjust the remaining $\alpha_p$ grains to their original size. A Euclidian distance map (EDM) morphological technique is used for this portion of the procedure. The advantage of EDM techniques are that they consider the distance of the pixel in question with respect to the nearest background (white) pixel. Thus, the resulting particles are more faithful to the true particle morphology than those resulting from a blind dilation technique in which pixels are indiscriminately added to the circumference of the particle. The final image is shown in Figure 3.10h, and this image is then used to populate the phase identifier field within the OIM data file.

### 3.4.7 Burgers Orientation Relationship Calculations

The material at the site of fatigue crack initiation was investigated with OIM to determine if the $\alpha_p$ and the lath $\alpha$ orientations were related to the parent $\beta$ grain by the Burgers orientation relationship. From the OIM scans, it was possible to measure orientations for both the $\alpha$ and $\beta$ grains. To determine whether a $\alpha_p$ grain and an adjacent $\beta$ grain were related by the Burgers orientation relationship, the measured Euler angles representing the orientation of an hcp $\alpha$ grain were transformed into those representing a bcc $\beta$ grain similar to reports by other groups [121–123]. For these calculations, the set of Euler angles $(\phi_1, \Phi, \phi_2)$, in Bunge notation were used to create the direction cosine matrix (DCM). To predict all the possible $\beta$ orientations, the 12 hexagonal symmetry operators and the 24 cubic symmetry operators had to be considered. This is completed using Equation 3.8, where $P_\alpha$ is the DCM for the measured $\alpha$ orientation, $S_j^\alpha$ is the set of 12 hexagonal symmetry operators, $S_k^\beta$ is the set of 24 cubic symmetry operators, $B^\beta$ is the DCM corresponding to the $\beta$ grain orientations,

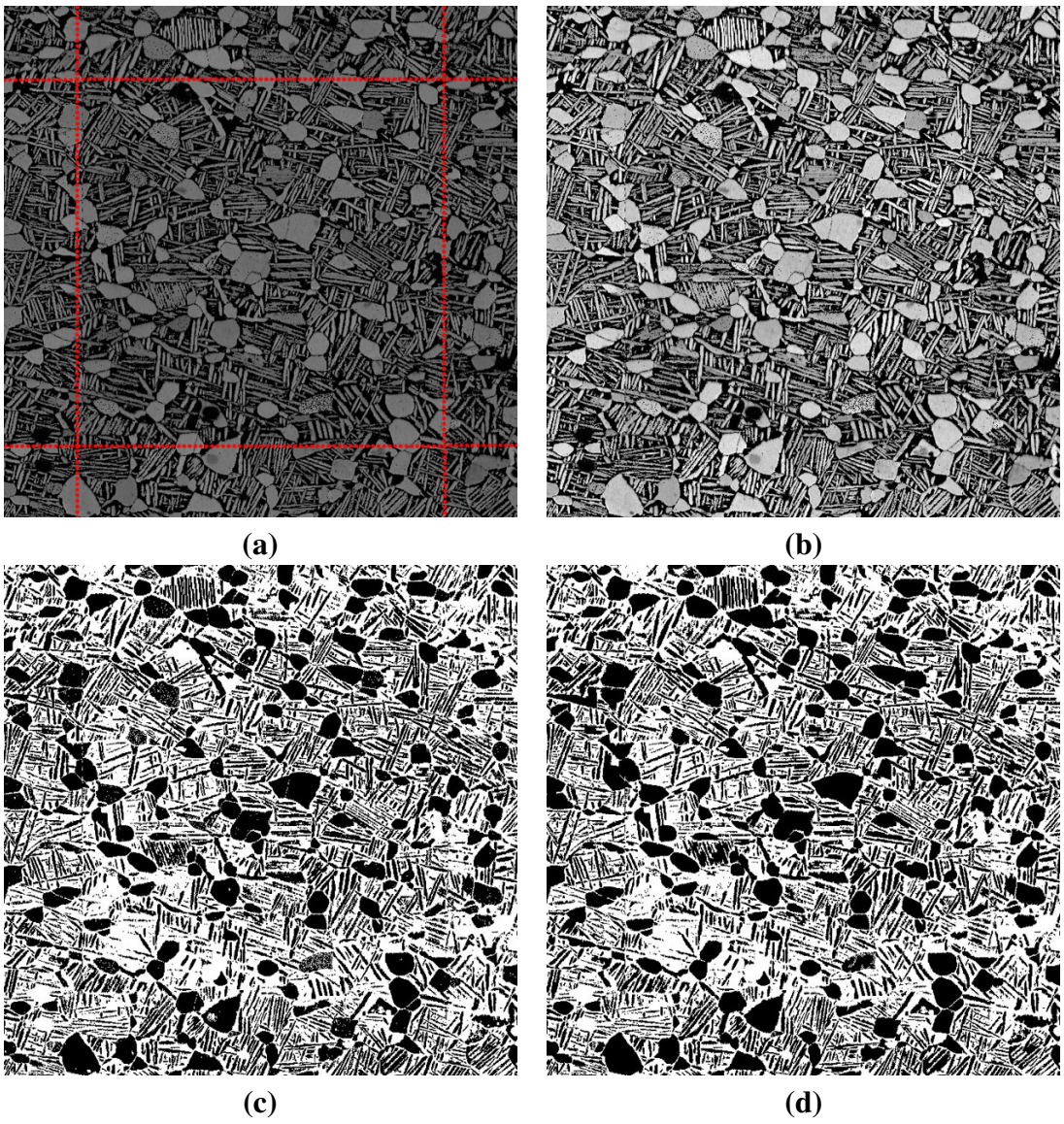


**Figure 3.9:** Individual steps of the texture separation process: (a.) Initial grayscale values acquired from OIM scan, (b.) Grayscale image after histogram equalization, (c.) Thresholding image to isolate pixels with grayscale values ≥ 148, (d.) Fill holes to fill in white spots within $\alpha_p$ grains.

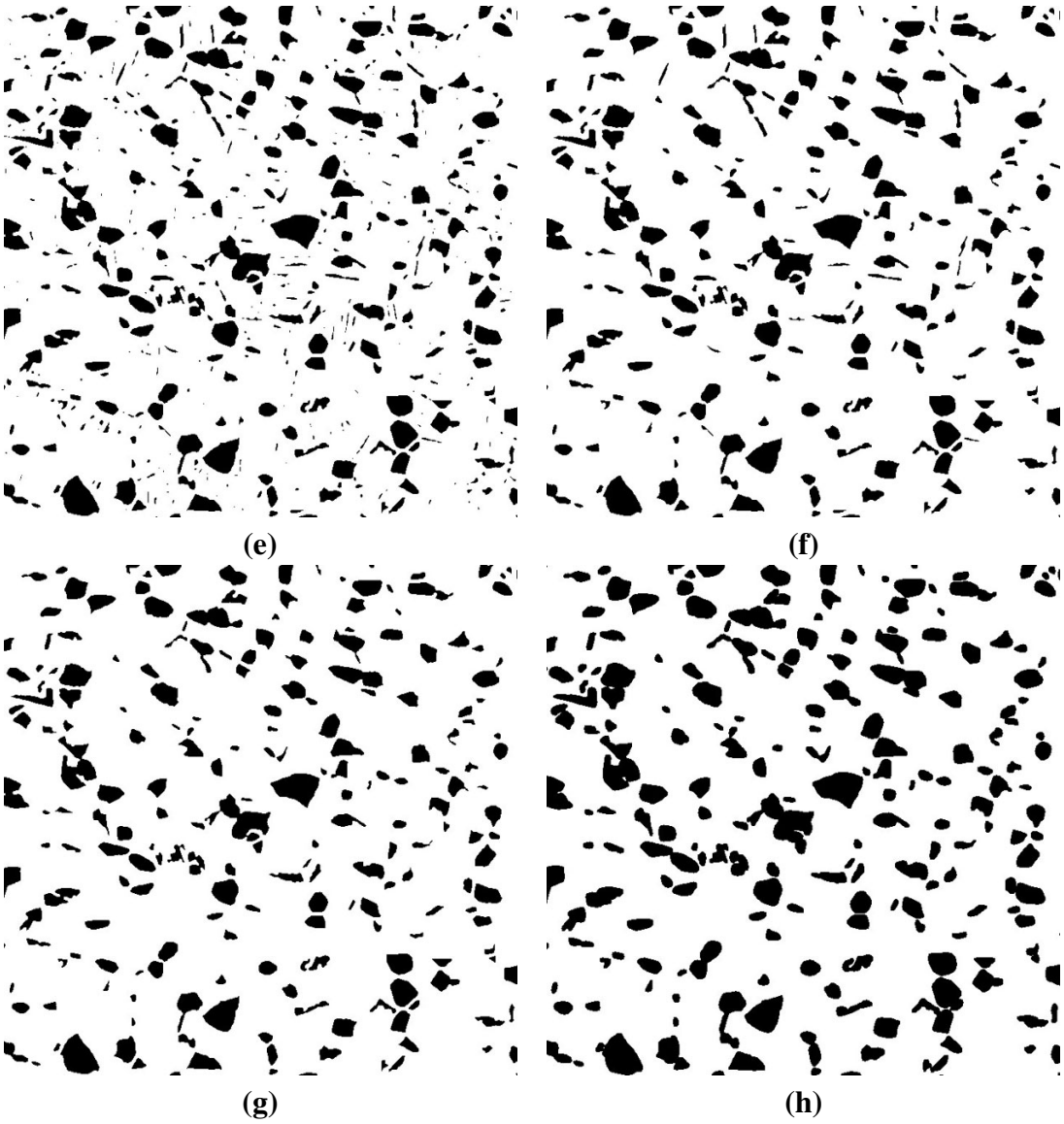


**Figure 3.10:** Individual steps of the texture separation process: (e.) EDM morphology: erosion depth = 2, (f.) reject features containing ≤ 40 pixels, (g.) Select features to include only those features with an aspect ratio in the range 1.0-4.0, (h.) EDM morphology: dilation depth = 2.

and D is the DCM of the Burgers orientation relationship. This can be rewritten as shown in Equation 3.9 for the purpose of predicting $\beta$ grain orientations. The Burgers orientation relationship for the $\alpha \rightarrow \beta$ phase transformation is $\phi_1 = 135, \Phi = 90$, and $\phi_2 = 325$.

$$DS_k^{\beta} B^{\beta} = S_j^{\alpha} P^{\alpha} \tag{3.8}$$

$$B^{\beta} = D^{-1} S_k^{\beta} S_j^{\alpha} P^{\alpha} \tag{3.9}$$

A script was written in MatLab to calculate the sets of Euler angles for all 288 (12 x 24) symmetrically equivalent $\beta$ grain orientations for each $\alpha_p$ grain. From all these 288 predicted orientations of the parent $\beta$ grain, the set of Euler angles representing the smallest misorientation with respect to the measured $\beta$ grain orientation was then selected as the most likely $\beta$ grain orientation. The misorientation, given as

$$\gamma = B_{meas}^{-1} B_{pred} \tag{3.10}$$

between the measured $\beta$ grain orientation and the $\beta$ grain orientation predicted from the $\alpha$ grain orientation was then calculated and this value is reported.

# Chapter 4

# Fatigue Behavior and Fractographic Analysis

This chapter presents experimental results from microstructural characterization, fatigue behavior, fractographic analysis, and textural analysis. These results are discussed with respect to prior results in the field, and a mechanism of fatigue crack initiation is proposed.

## *4.1 Microstructural Characterization*

Fatigue and microstructure studies were conducted on two different Ti-6246 materials: (1) a forged pancake intended to replicate the microstructure in a turbine disk and (2) a turbine disk that had been retired from service. Table 4.1 summarizes the microstructural characterization of the two materials. In both cases, specimens were extracted from the circumferential direction of the pancake and disk. The microstructure is treated as a uniform quantity, as no difference in microstructure was observed in specimens extracted from the bore and the rim of the disk. The microstructure of the pancake forging is shown in Figures 4.1 and 4.2. Using the linear intercept method, the $\alpha_p$ grain size was measured to be 3.7 $\mu$m $\pm$ 2.6 $\mu$m. As Figure 4.3 shows, the $\alpha_p$ grain size follows a log-normal distribution. The area fraction of $\alpha_p$ grains as measured by the point count method is $27\% \pm 3\%$. Within the transformed $\beta$ regions, Figure 4.2, the area fraction of lath $\alpha$ was measured as 50%, resulting in a total area fraction of alpha near 65% (30% $\alpha_p$ and 35% lath $\alpha$). Area fractions were measured using the point count method and verified with commercially available computational image analysis tools.

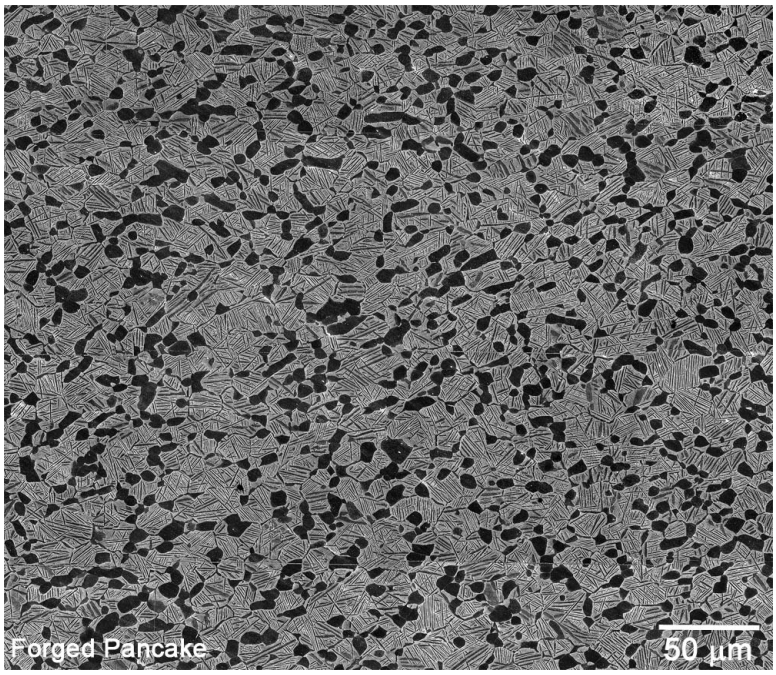


**Figure 4.1:** Secondary electron micrograph of a nominal microstructural area that displays the equiaxed $\alpha_p$ grains in a transformed $\beta$ matrix for the pancake microstructure.

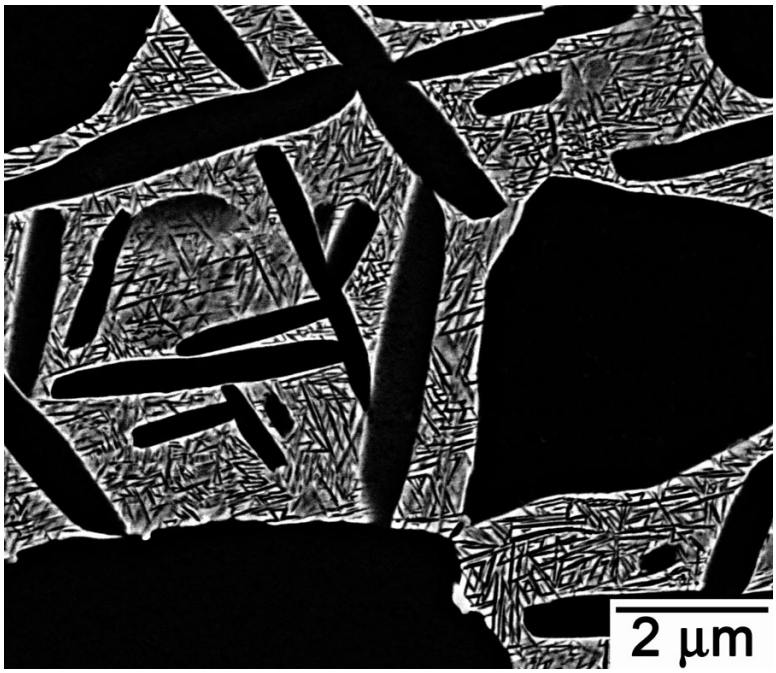


**Figure 4.2:** Backscattered electron micrograph displaying the presence of tertiary $\alpha$ within the transformed $\beta$ regions of material.

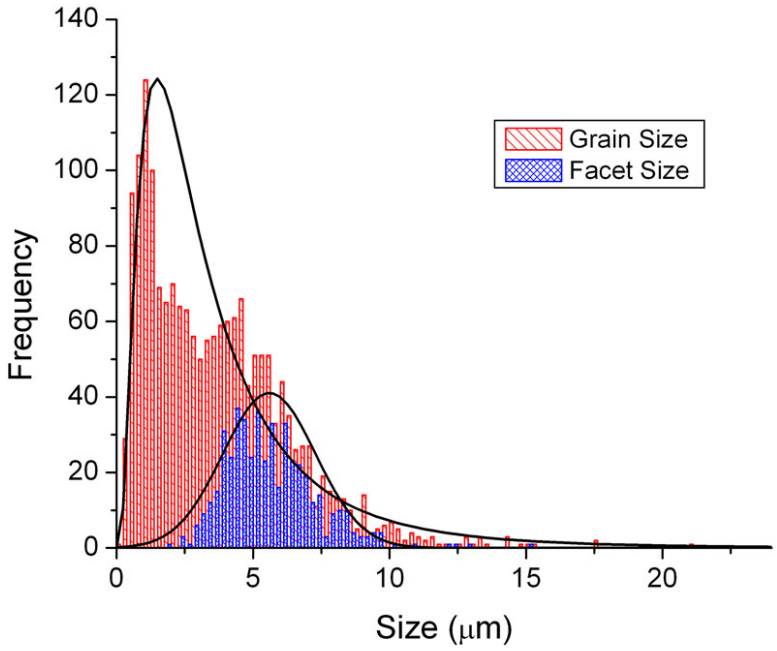


**Figure 4.3:** The histogram of $\alpha_p$ grain size and $\alpha_p$ facet size depicts the distribution of feature sizes measured from the pancake microstructure in this investigation.

The microstructure of the retired disk is shown in Figure 4.4. The histogram of grain sizes is shown in Figure 4.5. The $\alpha_p$ grain size for these samples was measured to be 4.7 $\mu$m ± 2.4 $\mu$m. The volume fraction of the $\alpha_p$ phase is 37% ± 4.6%, as measured with manual point counting and digital image analysis techniques. The lath $\alpha$ phase in the disk microstructure is finer than that in the forged pancake microstructure. Figure 4.6 also shows a more detailed view of the microstructure in the transformed $\beta$ regions, and from this micrograph it is possible to see a distribution of $\alpha$ precipitates similar to those observed in the forged pancake microstructure. These microstructural characteristics were measured in a number of different specimens to ensure that the measured quantities do not vary as a function of location within the component or bulk material from which the specimen blanks were extracted.

### 4.1.1 Prior $\beta$ grain size

The prior $\beta$ grain size was measured using OIM techniques, which are well suited to distinguishing the separate phases in the microstructure. Due to the high concentration of molybdenum, there is a relatively high percentage of retained $\beta$ phase as compared to conventional titanium alloys. This fact enabled direct observation of the $\beta$ phase grain orientations, and hence the prior $\beta$ grain sizes from the OIM IPF map, as shown in Figure 4.7a. Since OIM is sensitive to lattice strains, which may arise due to strain in the matrix resulting from the presence of precipitates within the retained beta regions, a specimen was vacuum heat treated at 824° for 2 hours and then vacuum furnace cooled to anneal the microstructure and solutionize the precipitates for imaging of the $\beta$ phase using OIM. A

**Table 4.1:** Initial Microstructural Characterization Results

| **Microstructure** | $\alpha_p$ **grain size** ($\mu$m) | **Volume Fraction** $\alpha_p$ |
|---|---|---|
| Forged Pancake | 3.7 ± 2.6 | 27% ± 3% |
| Retired Disk | 4.7 ± 2.4 | 37% ± 4.6% |

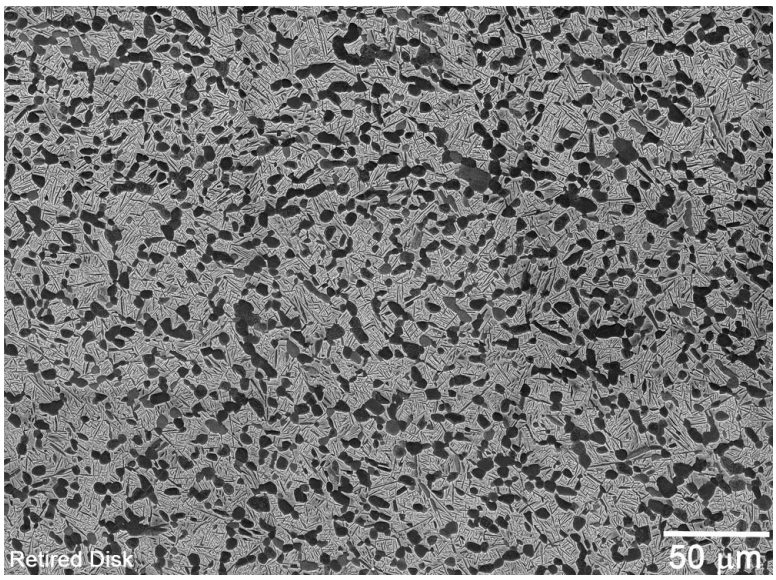


**Figure 4.4:** Secondary electron micrograph of a nominal microstructural area that displays the equiaxed $\alpha_p$ grains in a transformed $\beta$ matrix for the disk microstructure.

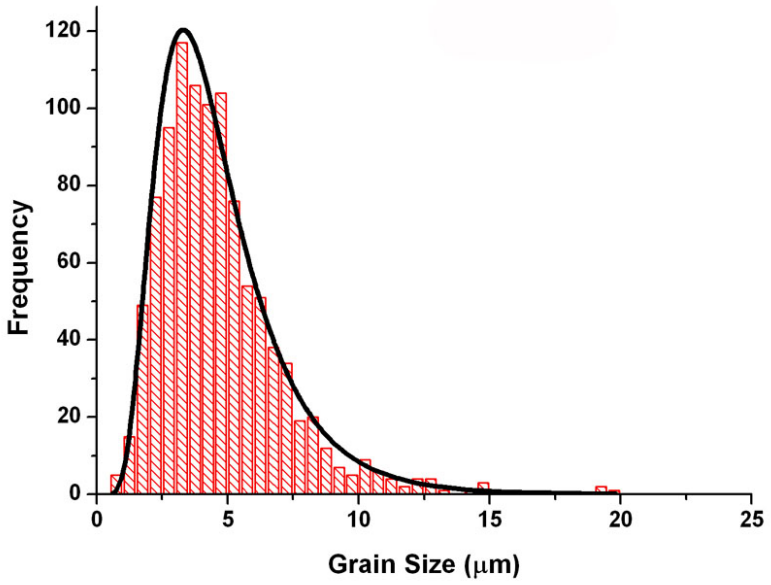


**Figure 4.5:** The histogram of $\alpha_p$ grain size measurements for the disk microstructure depicts the distribution of feature sizes measured in this investigation.

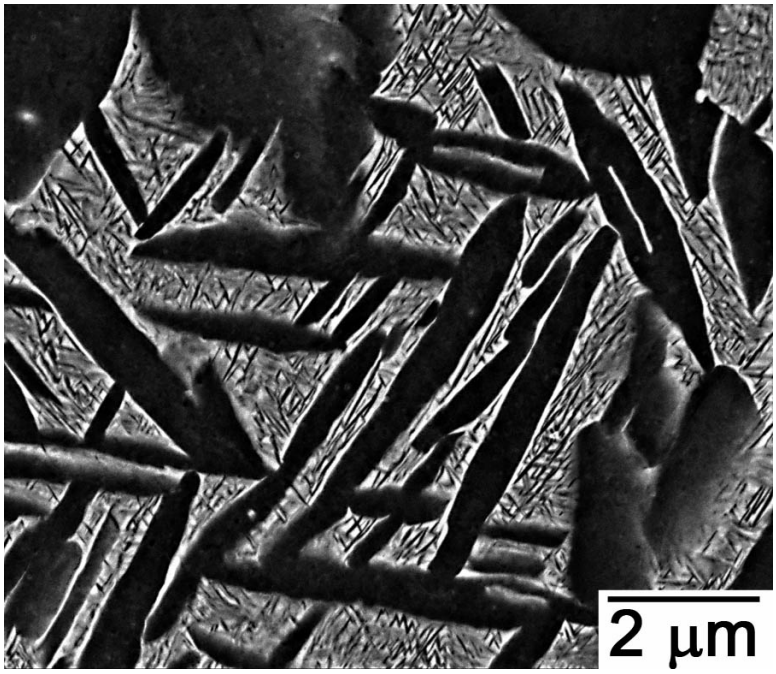


**Figure 4.6:** A high magnification micrograph of a random section in the disk sample.

backscattered electron micrograph is shown in Figure 4.8, and this image illustrates that the precipitates within the retained $\beta$ phase have been solutionized. The IPF map for the same sample after this heat treatment is shown in Figure 4.7b. These two images illustrate that the orientations of the $\beta$ phase measured directly from fatigue specimens are the same, and therefore the presence of precipitates does not adversely affect the proper indexing of the Kikuchi patterns in OIM. The prior $\beta$ grain size is measured to be approximately 20 $\mu$m, but larger regions on the order of a few hundred micrometers are commonly observed in the microstructure, and this will be characterized and discussed in greater detail in later sections.

## *4.2 Fatigue Lifetime*

Fatigue failures from ultrasonic fatigue testing ranged from $10^6$ to $10^9$ cycles, as shown in Figure 4.9. A comparison of fatigue lifetime behavior for conventional and ultrasonic

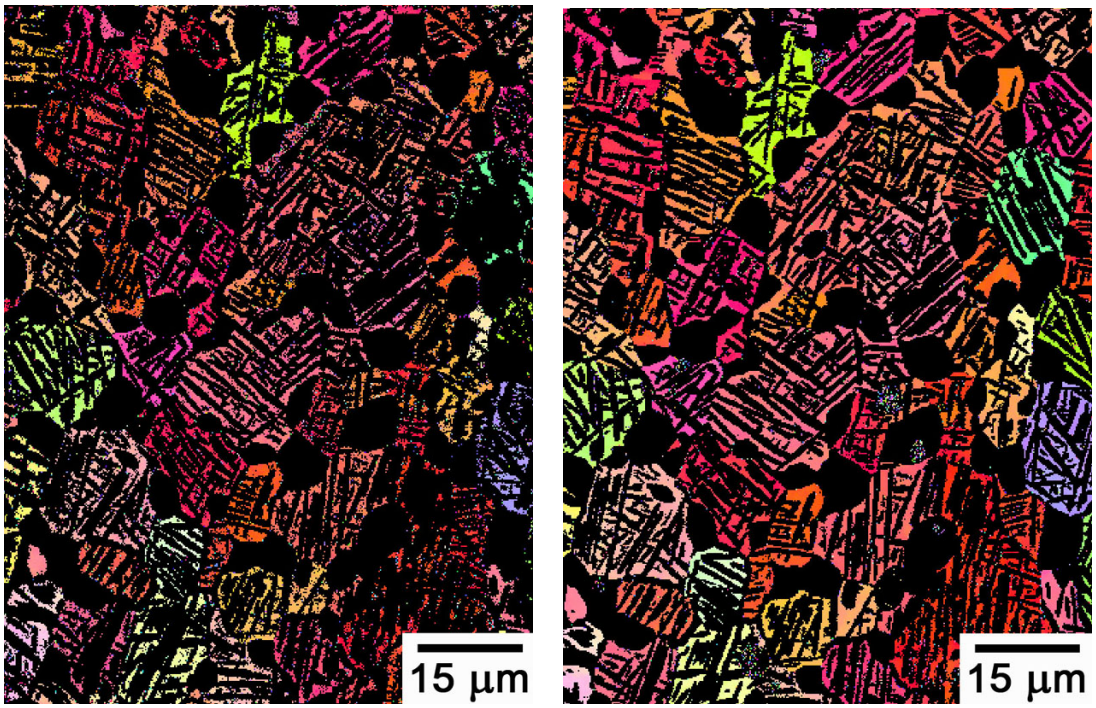


**(a)** **(b)**

**Figure 4.7:** Comparison of the prior $\beta$ grain orientations from an as-polished sample (a) and a heat treated sample (b), which was heat treated to solutionize the $\alpha$ precipitates within the transformed $\beta$ regions.

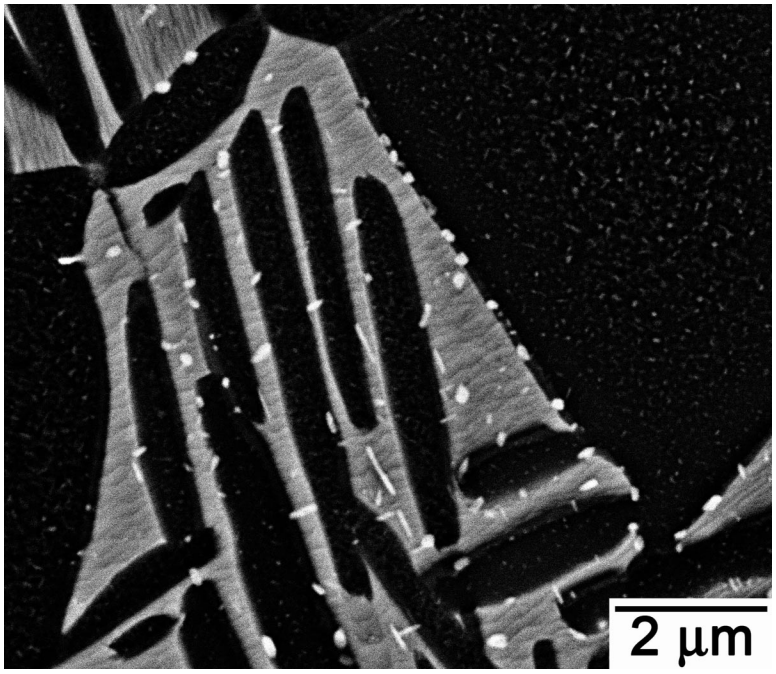


**Figure 4.8:** A high magnification backscattered electron micrograph of a random section following the vacuum heat treatement procedure used to dissolve the $\alpha$ preciptates from within the retained $\beta$ phase.

testing is presented in Figure 4.9. Data are shown for the two frequencies investigated - 20 Hz and 20 kHz, and all tests were run at a load ratio of 0.05. The 20 Hz tests were conducted at stress levels ($\sigma_{max}$) of 820 MPa and higher at AFRL [95]. Ultrasonic frequency fatigue testing was completed at 20 kHz at stresses ($\sigma_{max}$) of 700 MPa and below. Cracks initiated from surface and subsurface locations, as indicated by the open and closed data points, respectively. Although the stress levels used for conventional and ultrasonic fatigue do not overlap, the data follow the same trend, as expected for a typical stress-life (S-N) curve. This indicates that there is no appreciable frequency effect on fatigue lifetime between testing frequencies of 20 kHz and 20 Hz. This is consistent with the findings of Paparikicou et al. [105], who also observed a negligible effect of test frequency on the fatigue lifetimes of a similar $\alpha$+$\beta$ titanium alloy.

Subsurface crack initiation was more prevalent at both test frequencies as the stress

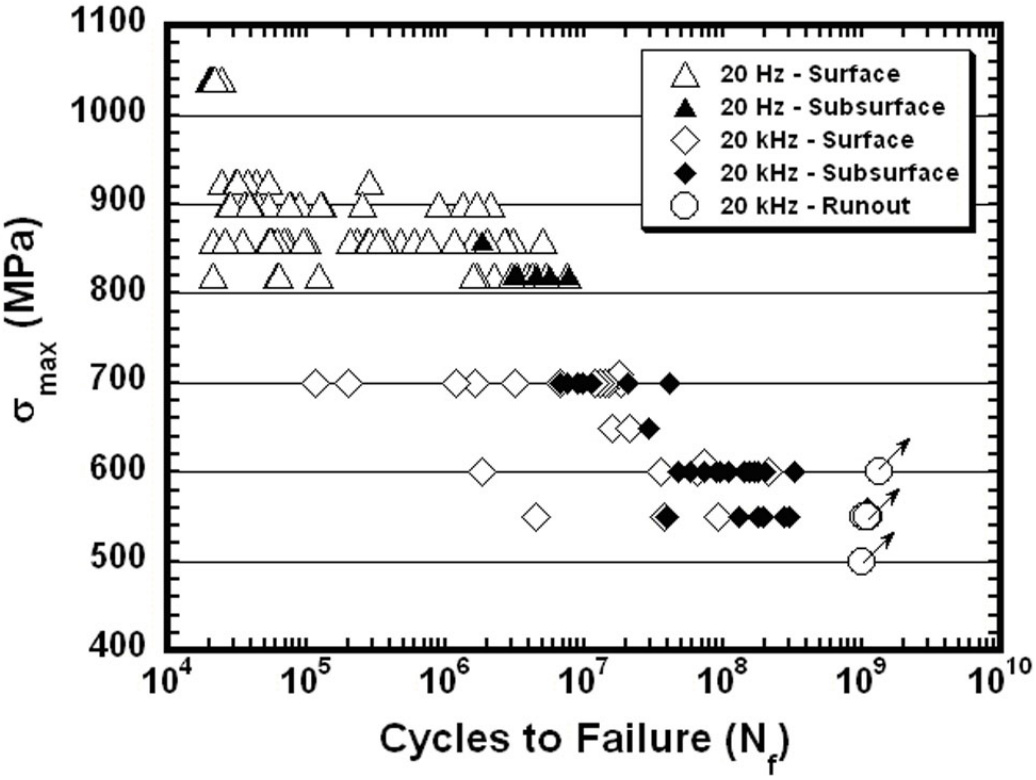


**Figure 4.9:** S-N curve displaying the fatigue lifetimes of specimens tested at ultrasonic frequencies and conventional frequencies [95].

level is decreased. At 20 kHz, surface crack initiation was observed approximately 80% of the time for the highest stress level investigated (700 MPa), while at the lowest stress level (550 MPa), only 20% of the specimens failed from a surface-initiated fatigue crack. At a given stress level, specimens that failed by surface crack initiation tended in most cases, but not all, to have shorter lifetimes than those that failed from subsurface crack initiation. However, in a few cases, surface initiated failures were observed to have similar lifetimes as specimens that failed from subsurface crack initiation sites, consistent with other investigations of fatigue in $\alpha + \beta$ titanium alloys [44]. This observation differs from the understanding of the fatigue behavior of René 95 developed by Cashman in which the bimodal distribution of fatigue lifetimes is determined simply by the location of the crack initiation site relative to the specimen surface [94].

## *4.3 Fractographic Analysis*

Fractographs of typical crack initiation sites in surface and subsurface locations are compared in Figure 4.10. In all cases, facets are observed at the site of crack initiation, and their size is commensurate with the size of the larger $\alpha_p$ grains. During fatigue, the facets are presumed to form in $\alpha_p$ grains along a preferred crystallographic plane and are referred to here as $\alpha_p$ facets. The average $\alpha_p$ grain size is approximately 4 $\mu$m, as measured from a random 2D section, while the average facet size is 5.3 $\mu$m. The histogram of $\alpha_p$ facet size is overlaid on the $\alpha_p$ grain size histogram in Figure 4.3. The $\alpha_p$ facet sizes were measured from SEM micrographs. It is noted that facets are actually three dimensional features projected onto a 2D micrograph; i.e. the true size of the facets is larger than is represented in the histogram. The angle of the facet normal with respect to the fracture surface was not determined for every facet, but it was determined for selected facets near the site of fatigue crack initiation, and these results will be presented in Section 4.3.3. Therefore, it is not possible to determine the true dimensions of all the facets. To summarize, facets form in $\alpha_p$

grains that are slightly larger than average, but clearly do not fall into the tails of the grain size distribution.

Based on the appearance of the fracture surface near the crack initiation site, three distinct crack initiation types have been identified: (1) surface, (2) isolated subsurface faceting, and (3) macroscopically planar subsurface sites. In the case of categories 1 and 2, individual $\alpha_p$ facets are observed on the fracture surface, as shown in Figure 4.10 (a) and (b), respectively. Figure 4.10 (c) illustrates the third type of crack initiation site, which consists of a macroscopically planar region that is occasionally observed in subsurface crack initiation. This type of crack initiation spans a number of $\alpha_p$ grains and transformed $\beta$ regions, and the crack appears to form along the same plane relative to the loading axis in each of these grains. Upon closer inspection of these macroscopically planar initiation sites, evidence of ductile fracture processes is apparent within these large flat regions. Thus, it is not appropriate to call them facets, since they are not truly planar. Crack initiation was classified as surface if the $\alpha_p$ facets intersected the specimen surface. Figure 4.11 displays the fatigue lifetimes where the data points have been classified into three different groups depending on the appearance of the fatigue crack initiation site. It is thought that the appearance of the fracture surface provides insight into the mechanism of fatigue crack initiation and the type of defect responsible for the formation of a fatigue crack. As shown in Figure 4.11, surface crack initiation generally leads to the shortest lifetimes. However, the lifetimes of specimens failing by the two types of subsurface crack initiation mechanisms are not significantly different. If these three different types of crack initiation sites are classified as different mechanisms, it would be more instructive to compare the fatigue lifetime distributions as a function of the mechanism of crack initiation. In Figure 4.12, a plot of the average lifetimes to failure for all of the specimens that have fractured by each of the three mechanisms is shown. From this plot, it is still apparent that the surface initiated failures tend to have the shortest lifetimes. Based on the data, it is not possible to determine

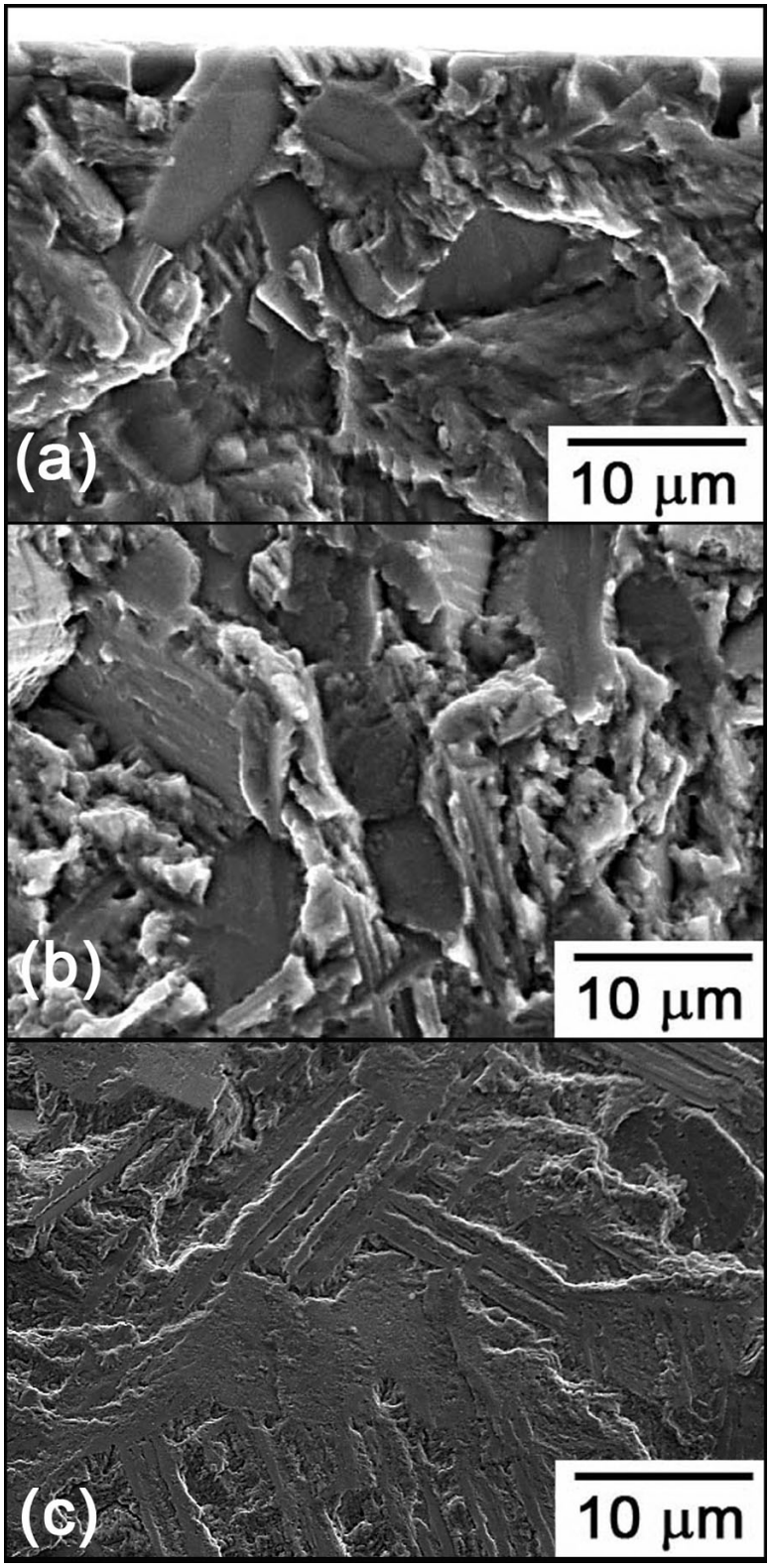


**Figure 4.10:** Fractographs displaying examples of the three types of fracture surfaces: (a) surface, (b) isolated subsurface faceting, and (c) macroscopically planar subsurface crack initiation sites.

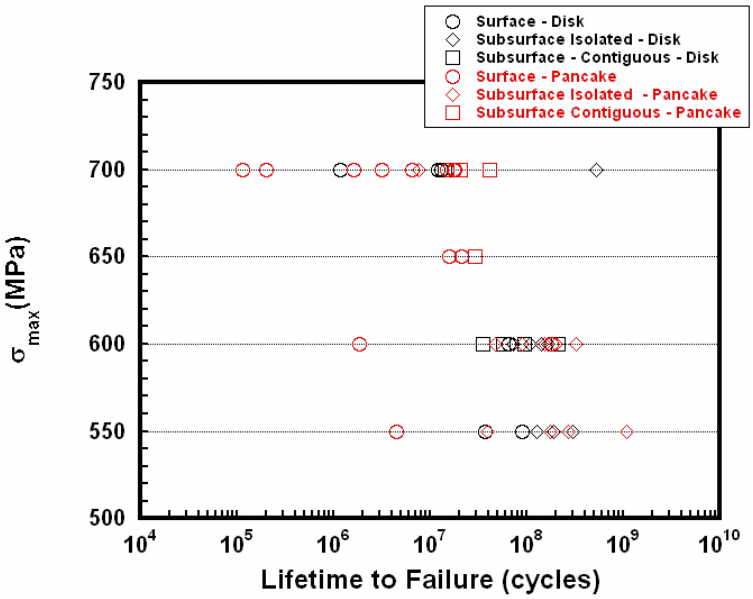


**Figure 4.11:** S-N curve displaying only ultrasonic frequency (20 kHz) data with initiation types distinguished.

whether a difference in lifetime is observed as a function of the initiation category. That is, in some cases, the subsurface isolated facets type of failure exhibits the longest lifetimes, while at other stress levels, the subsurface contiguous faceting mode of crack initiation exhibits longer lifetimes. Thus, it is not possible to rank the individual crack initiation mechanisms based on order of susceptibility to fatigue crack initiation.

Subsurface crack initiation has been observed in a number of fatigue studies on $\alpha$ + $\beta$ titanium alloys [43, 44, 59, 60, 95, 99]. The competition between surface and subsurface crack initiation sites has alternately been attributed to the specimen surface to volume ratio [97], the presence of compressive residual stresses on the surface [99], environmental effects [124], and the relative ease with which grains can deform at a free surface as compared to the specimen interior.

In the regime of VHCF, the low applied cyclic stresses are believed to result in only certain microstructural neighborhoods being susceptible to fatigue damage accumulation.

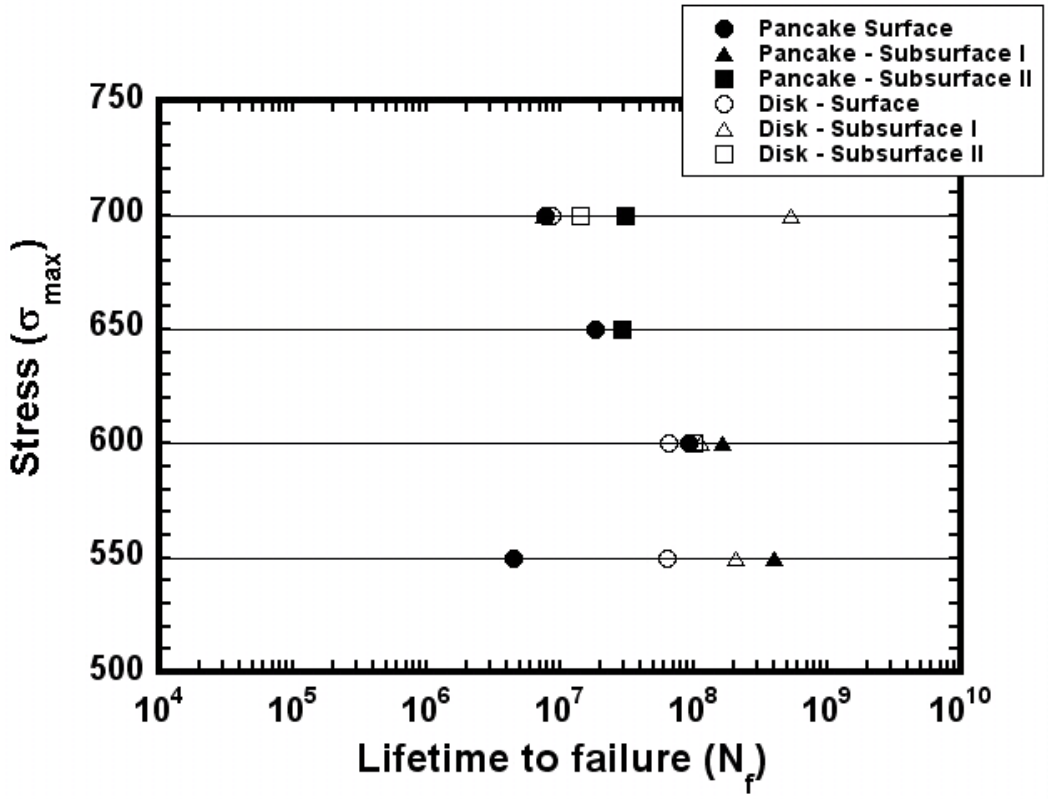


**Figure 4.12:** S-N curve displaying the average lifetime to failure of the specimens for each of the given crack initiation mechanisms.

These damage accumulation processes lead to fatigue crack initiation, and these microstructural configurations do not necessarily exist at the specimen surface. This idea was first put forth by Mughrabi [97] and Jha and Larsen [96] subsequently proposed that different microstructural neighborhoods may be in competition with one another to initiate the dominant fatigue crack. In the current work, it appears that there may be a number of different microstructural regions in each sample that may initiate a fatigue crack, however only the site that accumulates fatigue damage most rapidly will ultimately lead to fatigue crack initiation. The fact that three characteristic crack initiation sites have been observed at the same stress level indicates that there is competition between different microstructural neighborhoods for crack initiation. The evidence suggests that if there is not a suitable group of $\alpha_p$ grains near the specimen surface, then a crack will initiate from the specimen interior, and the presence of different microstructural neighborhoods in the interior will cause either a subsurface initiation site with isolated facets or with a macroscopically planar region. The occurrence of $\alpha_p$ facets at the crack initiation sites indicates that $\alpha_p$ grains are influential in accumulating fatigue damage and subsequent fatigue crack initiation. Similar observations led to speculation [61] that specific spatial and crystallographic orientations of $\alpha_p$ grains are required for fatigue cracks to initiate in the HCF regime of other titanium alloys.

Subsequent subsections discuss results from further investigations of fracture surfaces. These investigations have been completed as an attempt to gather insight into the process of fatigue damage accumulation leading to fatigue crack initiation. Furthermore, these investigations have been completed to identify the characteristics that distinguish fatigue critical neighborhoods from nominal microstructures.

### 4.3.1 Crack Initiation Location

In one study [125], the variability in fatigue lifetimes is related to crack initiation location. Surface cracks exhibit the shortest lifetimes, while subsurface cracks displayed much longer lifetimes to failure. The distance from the crack initiation site to the specimen surface has been measured in all fatigue specimens, and the results are shown in the plot in Figure 4.13. These values are measurements of the distance from the specimen surface to the center of the fatigue crack initiating facet. Specimens that exhibited surface-connected facets or facets within one of their own diameters from the specimen surface were classified as surface failures. Therefore, any failures that were observed to initiate from features within approximately 10 $\mu$m of the surface are classified as surface initiated failures, and this is indicated with the dotted line on the plot. The overall trend is that the specimens with longer fatigue lifetimes result from crack initiation locations that are farther into the interior of the specimen, whereas the short lifetime specimens tend to initiate cracks within grains located at the specimen surface. However, there is a fair amount of scatter in the data, as surface and near surface ($\leq$ 20 $\mu$m from surface) initiated failures are observed to have lifetimes ranging from $10^5$ cycles up through $10^8$ cycles. In some cases, specimens that failed from subsurface initiated fatigue cracks exhibit shorter lifetimes than those that have failed due to surface crack intitiation. The existence of this scatter inhibits the direct correlation of initiation location with lifetime, but overall the general trend is observed such that in the case of fatigue crack initiation from the specimen interior, a longer fatigue lifetime will typically be observed. Since the fatigue lifetimes of specimens cannot simply be determined as a function of the distance from the initiation site to the specimen surface, this indicates that the scatter in lifetimes is not dominated by scatter in fatigue crack growth rates in vacuum compared with lab air. The implication of this is that scatter in fatigue lifetimes results from variability in the fatigue crack initiation process.

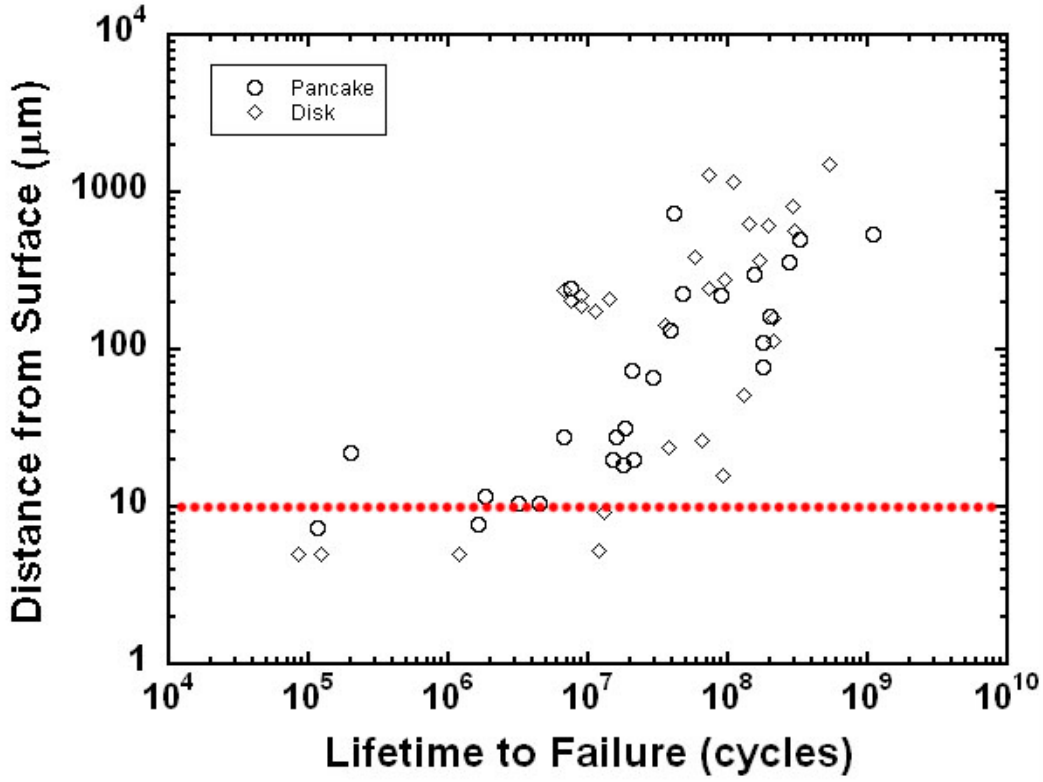


**Figure 4.13:** A plot of the distance from the initiation site to the specimen surface as a function of fatigue lifetime.

### 4.3.2 Spatial Clustering of $\alpha_p$ grains

RaviChandran and Jha [60] observed that clusters of the $\alpha_p$ grains are the fatigue critical microstructural neighborhoods in Ti-10-2-3. This agreed with earlier results by Mahajan and Margolin [51] who speculated that the proximity of $\alpha_p$ grains to each other is an important characteristic in determining where fatigue cracks will initiate, due to the ease with which slip may accumulate in clusters of $\alpha_p$ grains. Also, as Hall mentions [31], clusters of $\alpha_p$ grains can increase the effective slip length which is a critical factor in the damage accumulation process.

Figure 4.14 shows a fracture surface for which the $\alpha_p$ facets have been highlighted. As illustrated in this figure, there is a higher tendency of faceted fracture of $\alpha_p$ grains near the site of fatigue crack initiation. To characterize the spatial distribution of $\alpha_p$ grains and to determine whether this influenced fatigue crack initiation in the current work, the area fraction of $\alpha_p$ facets was measured from fracture surfaces. The results are shown in Figure 4.15, where the area fraction of the fracture surface covered by facets is plotted as a function of the crack tip driving force. The stress intensity values on the abscissa were calculated using the Newman Raju [117] stress intensity solutions for surface cracks while the Murakami [126] solutions were used for subsurface cracks. The thick bounding lines in the plot represent the extremes of $\alpha_p$ grain spatial distribution in the general microstructure, i.e. the most clustered regions and the regions nearly devoid of $\alpha_p$ grains. As larger areas are probed, the area fraction of $\alpha_p$ grains, which is represented by these bounding lines, converges to the global measurement of $\alpha_p$ area fraction of 27% as indicated by the horizontal dotted line. Open data points represent failures by surface initiation, while closed data points mark the area fraction of facets from specimens that failed by subsurface crack initiation. The legends in the plots indicate the lifetime of specimens that have been examined with this analysis. These data have been dissected in two different ways to examine

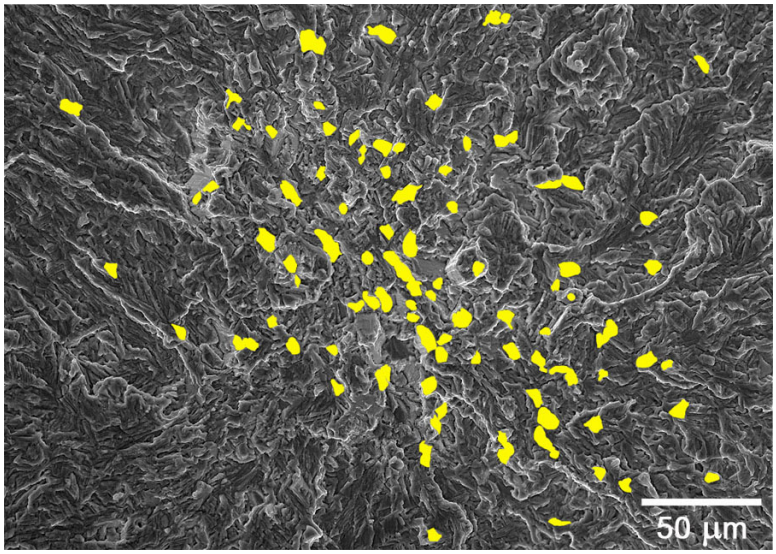


**Figure 4.14:** A typical fractograph displaying isolated subsurface faceting where the facets have been highlighted.

differences in faceting between surface and subsurface crack initiation, as well as the effects of stress level. The plots in Figure 4.15(a) and (b) illustrate the area fraction of faceting in surface and subsurface initiated failures, respectively. Figure 4.15(c) displays the area fraction of facets with respect to the presumed crack size for specimens tested at 700 MPa ($\sigma_{max}$), while Figure 4.15(d) shows this data for specimens tested at 600 MPa ($\sigma_{max}$).

A number of observations can be drawn from these plots; firstly, the area fraction of $\alpha_p$ facets typically decreases as material farther from the crack initiation site is considered. As the facet formation process is suspected to result from fracture of $\alpha_p$ grains on crystallographic planes oriented favorably for slip, the apparent lack of faceting for large crack sizes is expected, since long cracks are not expected to propagate in a crystallographic manner. The local microstructure is known to influence crack initiation and small crack growth [58, 61, 62], and therefore more facets are expected to form in these regions than in regions where long crack growth conditions apply.

The results suggest that there is no critical value of spatial clustering of $\alpha_p$ that must be met for cracks to initiate. In some cases, the $\alpha_p$ facets are much more dispersed at the site of

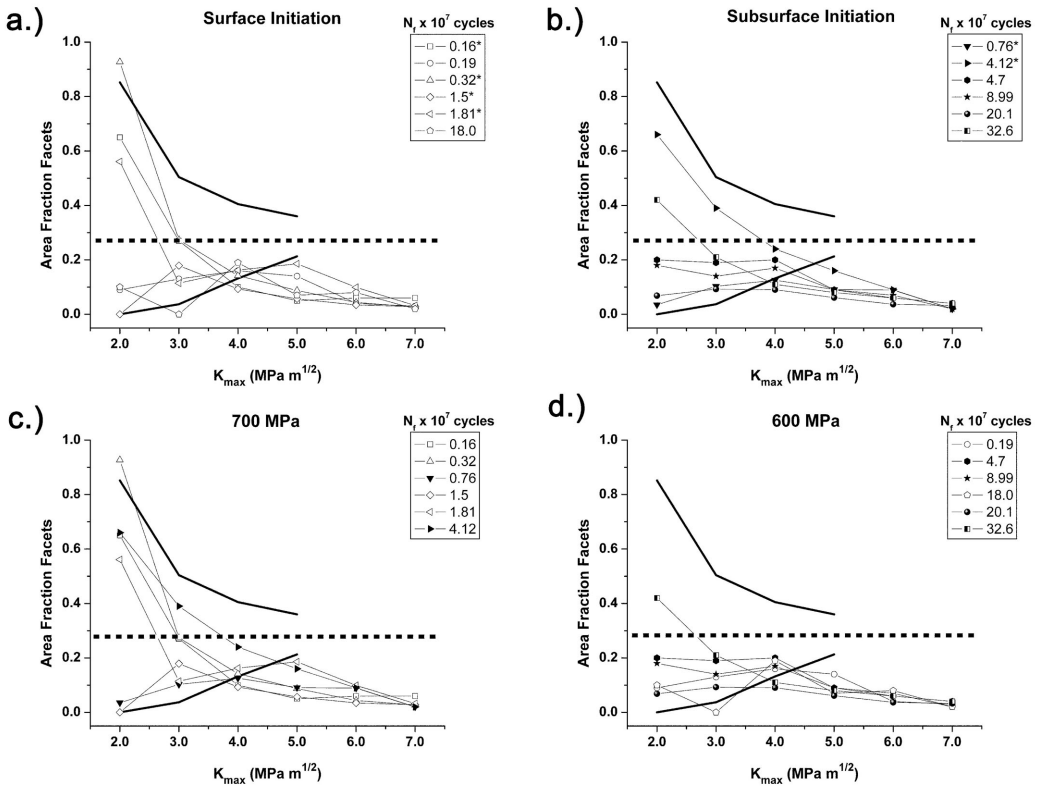


**Figure 4.15:** Area fraction clustering plots for (a) surface crack initiation, (b) isolated subsurface faceting, (c) failures from testing at ($\sigma_{max}$) 700 MPa, and (d) 600 MPa. The dark bounding lines depict the extremes of spatial orientations of $\alpha_p$ grains within the nominal microstructure.

crack initiation than the $\alpha_p$ grains are in the general microstructure, while in other samples the degree of faceting at the initiation site is markedly higher than the average $\alpha_p$ grain distribution. Thus, the spatial distribution of $\alpha_p$ grains alone does not determine where cracks will initiate in the general microstructure. Additionally, the lifetimes of specimens do not correlate with the spatial distribution of $\alpha_p$ at the crack initiation sites. Assuming that the majority of $\alpha_p$ grains that a propagating fatigue crack interacts with fail by faceted fracture, this suggests that the area fraction of faceting is not indicative of the rate of fatigue damage accumulation or the degree of difficulty to initiate a fatigue crack in these microstructural regions. As the plots in Figure 4.15(a) and (b) illustrate, there is no discernable difference in the degree of faceting between surface and subsurface crack initiation. It is apparent that in general more faceting is observed at the crack initiation sites for higher stress levels of $\sigma_{max}$ as shown in Figure 4.15(c) and (d). If faceting resulted from crystallographic propagation of short fatigue cracks, this trend would be expected to be reversed. Therefore, this finding suggests that the higher resolved stresses on the basal and prism slip systems in unfavorably oriented grains may cause slip to be activated in grains that would not otherwise contribute to the damage accumulation process. As a result, a larger volume of material could contribute to the crack initiation process at higher stress levels.

### 4.3.3 Spatial Orientation of Facets

A number of researchers [43,44,49,59,99,127] have found that facets at the crack initiation site are typically oriented normal to the tensile axis. This led some researchers [44, 127] to speculate that stress redistribution within the microstructure can lead to activation of a pseudo-cleavage mechanism of fatigue crack initiation. This mechanism proposes that grains oriented for slip may induce stress in adjacent grains in which the active slip planes are not oriented for slip. As the stress imposed on this neighboring grain increases, it will eventually fail by a cleavage type failure mechanism as described in Section 2.2.1.2 and

shown in Figure 2.12. A representative set of specimens have been examined to measure the spatial orientation of these facets for each of the three observed crack initiation mechanisms. In the current study, the larger facets at the crack initiation site are typically oriented for high resolved shear stress (facet normal is inclined at an angle of greater than 30° with respect to the fracture surface plane).

An example of a surface initiated failure is illustrated in Figure 4.16, where the facets that have been measured by this technique are highlighted, and the labels correspond to the numbers in Table 4.2. Facets 1 and 2 have the ideal spatial orientation for slip. Facet 4 is notable, since its normal forms only a 19° angle with respect to the tensile axis. This observation agrees with the work of Williams et al. [16] in which basal slip was observed to occur in Ti-6.6Al single crystals where the basal plane was only 13-15° from a perpendicular orientation with respect to the tensile axis.

An example of a fracture surface from a specimen that failed by subsurface fatigue crack initiation with isolated facets is shown in Figure 4.17, and the corresponding measurements are shown in Table 4.3. As measurements listed in the table illustrate, the majority of the facets are oriented for high resolved shear stress. Additionally, these facets are isolated from one another and they are all oriented at different angles with respect to the tensile axis. This is in contrast with the measurements of the facet angles for the subsurface contiguous faceting mechanism displayed in Figure 4.18, where it is clear that many of the facets share the same orientation with respect to the tensile axis. The measurements for this subsurface contiguous mechanism of crack initiation are shown in Table 4.4.

Specimens were sectioned to expose the microstructure below the crack initiation site, as shown in Figure 3.8, which is a schematic that depicts the sectioning plane cutting through the crack initiation site. An SEM micrograph of a specimen that was prepared by this sectioning procedure is shown in Figure 4.19, which illustrates that the crack plane is not perpendicular to the loading axis at the crack initiation site. The tensile axis in this

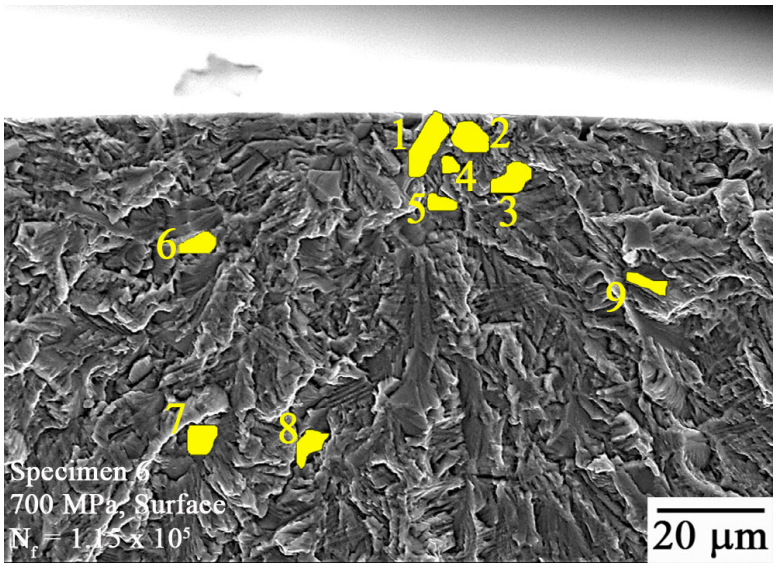


**Figure 4.16:** A fractograph of a surface initiated failure indicating the facets that have been measured with MeX. $N_f$=1.15 x $10^5$ cycles, $\sigma_{max}$=700MPa.

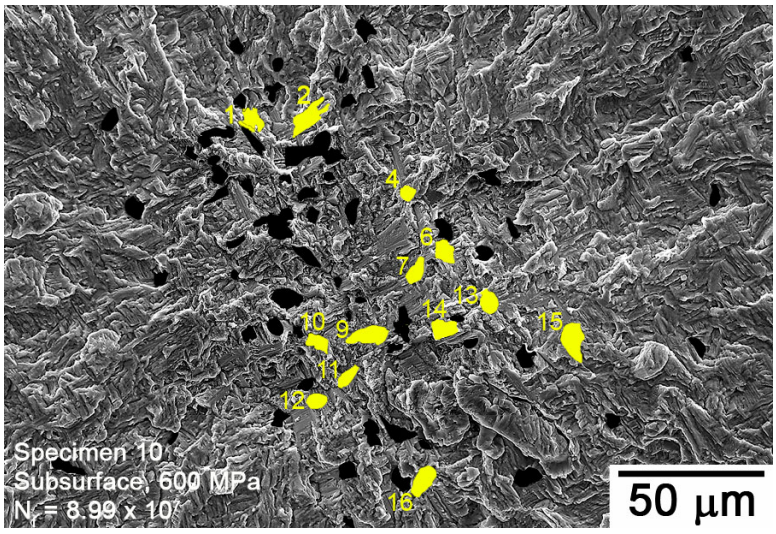


**Figure 4.17:** A fractograph of a subsurface initiated failure with isolated facets indicating the facets that have been measured with MeX. $N_f$=8.99 x $10^7$ cycles, $\sigma_{max}$=600MPa.

image is vertical in the plane of the page. From this image, it is apparent that the crack initiation process is caused by slip, since this plane is oriented for a high resolved shear stress. These results indicate that for this alloy and test condition, fatigue cracks initiate by a slip process and not by pseudo-cleavage as observed in other investigations [49, 127] of the fatigue behavior in $\alpha + \beta$ titanium alloys.

### 4.3.4 Summary of Fractographic Analysis

In this section, three distinct types of fatigue crack initiation sites have been identified: surface, subsurface with isolated facets, and subsurface with contiguous facets. The fractographic analyses described here found that fatigue critical microstructural regions cannot be distinguished from nominal microstructural areas based simply on clustering of the $\alpha_p$

**Table 4.2:** Spatial Orientation of Facet Normals for Surface Initiated Failures

| Facet Number | 1 | 2 | 3 | 4 | 5a | 5b | 6 | 7 | 8 | 9 |
|---|---|---|---|---|---|---|---|---|---|---|
| Spatial Orientation (w.r.t. tensile axis) | 46 | 45 | 39 | 19 | 26 | 35 | 33 | 31 | 32 | 21 |

The values in this table are presented in degrees and the measurements correspond to the facets illustrated in the fractograph shown in Figure 4.16.

**Table 4.3:** Spatial Orientation of Facet Normals for Subsurface Initiated Failures

| Facet Number | 1 | 2 | 4 | 6 | 7 | 9 | 10 | 11 | 12 | 13 | 14 | 15 | 16 |
|---|---|---|---|---|---|---|---|---|---|---|---|---|---|
| Spatial Orientation (w.r.t. tensile axis) | 37 | 45 | 41 | 38 | 44 | 36 | 14 | 38 | 31 | 31 | 50 | 11 | 32 |

The values in this table are presented in degrees and the measurements correspond to the facets illustrated in the fractograph shown in Figure 4.17.

**Table 4.4:** Spatial Orientation of Facet Normals for Subsurface Initiated Failures with Contiguous Facets

| Facet Number | 1 | 2 | 3 | 4 | 5 | 6 |
|---|---|---|---|---|---|---|
| Spatial Orientation (w.r.t. tensile axis) | 34 | 40 | 59 | 40 | 30 | 38 |

The values in this table are presented in degrees and the measurements correspond to the facets illustrated in the fractograph shown in Figure 4.18.

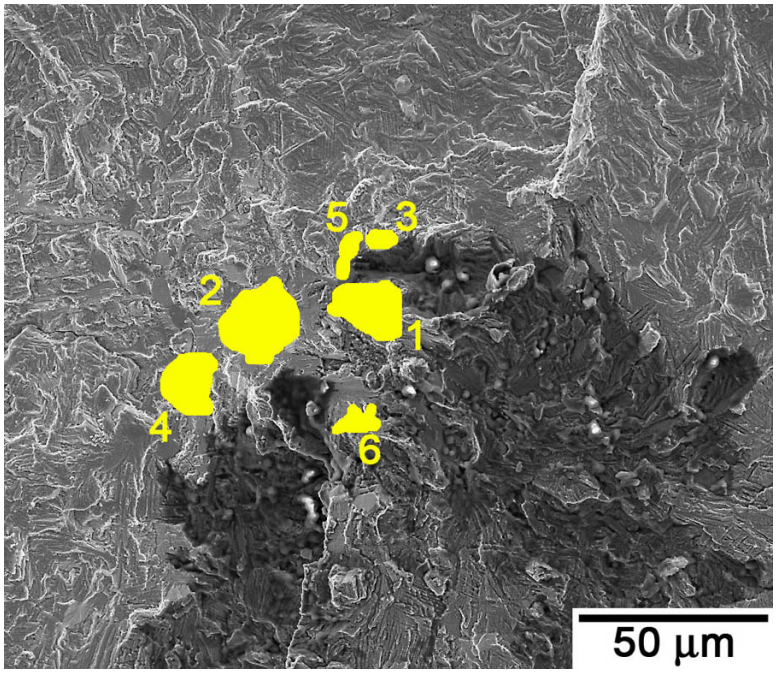


**Figure 4.18:** A fractograph of a subsurface initiated failure with contiguous facets indicating the facets that have been measured with MeX. $N_f$=4.12 x $10^7$ cycles, $\sigma_{max}$=700MPa.

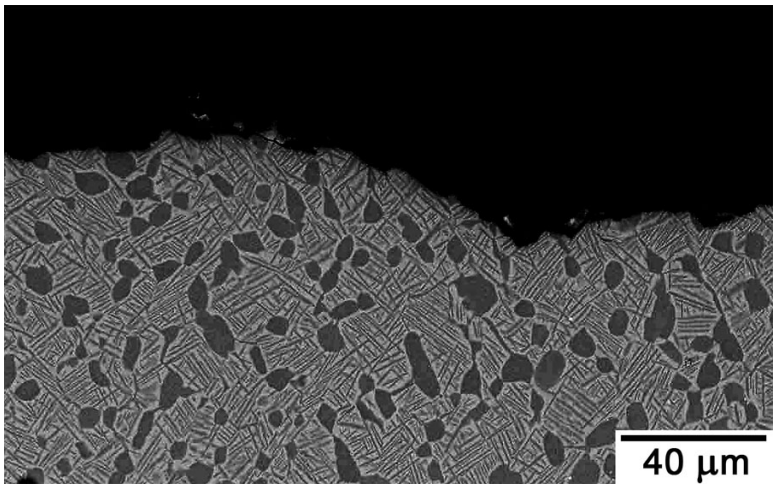


**Figure 4.19:** Subsurface crack initiation site after sectioning to expose a plane just below the crack initiation site.

grains near the initiation sites and the fatigue lifetimes do not appear to correlate with the distance between the initiation site and the specimen surface. In other words, specimens failing by surface fatigue crack initiation exhibit scatter over two orders of magnitude and this scatter overlaps with the scatter in subsurface fatigue crack initiation sites. Using stereo pairs, the facets on the fracture surface appear to form by slip rather than by cleavage. The next few sections will discuss the importance of crystallographic texture in the fatigue crack initiation process.

## *4.4 Crystallographic Orientation of Crack Initiating Region*

As noted by Hall [31] among other researchers, the deformation of $\alpha + \beta$ titanium alloys is attributed primarily to the $\alpha$ phase. Since the hexagonal crystal structure of $\alpha$ phase titanium is highly anisotropic, the crystallographic orientation of these grains with respect to the tensile axis will significantly affect the activation of specific slip systems within $\alpha_p$ grains. Furthermore, the ability of these grains to deform in concert with each other dictates that local textures will have a significant effect on the mechanical properties. It seems reasonable that both the texture orientation and intensity in these microstructural neighborhoods will determine how easily cyclic damage accumulates. The objective of Sections 4.4 and 4.5 is to establish which slip systems are active and the significance of crystallographic texture in these microstructural neighborhoods. Insights gained from this investigation will be used to propose a model of how the damage accumulation process leads to fatigue crack initiation.

### 4.4.1 Crystallographic Orientation of Fracture Facets

Since the spatial orientation of the facets with respect to the tensile axis is known, OIM was used to determine if the facet planes corresponded to a specific crystallographic plane. The facets observed on the fracture surface were determined to be basal planes of the equiaxed

$\alpha_p$ grains, which appear to be highly oriented for slip. The Schmid contours can be plotted on inverse pole figures as an illustration of the value of the Schmid factor for a given crystallographic orientation and slip system. These plots are shown in Figure 4.20 for basal, prism, and first-order pyramidal $\langle a \rangle$-type slip, respectively.

Facets have been examined in surface initiated failures, and a typical IPF map is shown in Figure 4.21. The schematic in Figure 3.8 illustrates the reference frame for this image. RD corresponds to the tensile axis, while ND is normal to the polished surface. Although the micrograph displays the microstructure as viewed from the RD-TD plane, the orientations that these colors represent are shown from the perspective of viewing down the RD axis, or equivalently, the tensile axis. The colors in the IPF map correspond to the colors in the unit triangle shown in Figure 4.20d. The facet in this scan formed along the basal plane in a $\alpha_p$ grain oriented for slip as indicated with a "1" in this IPF map. The grain is highly oriented for basal slip as shown by the marker in the inverse pole figure on the right side of the image. The spatial orientation of the facet that formed in this grain is listed in Table 4.2 as facet 1. The angle between the basal pole and the tensile axis was measured to be 45° using OIM techniques. Additionally, the spatial angle is 46° for the facet angle with respect to the tensile axis and the plane trace of the basal plane in this grain is parallel to the facet plane. These measurements mean that the facet plane forms on the basal plane of the $\alpha_p$ grain.

The inverse pole figure (IPF) map from an OIM scan is shown in Figure 4.22 for a specimen that failed from subsurface isolated faceted fracture. The orientations of the four indicated features are also plotted in the inverse pole figure in the bottom right of Figure 4.22, which displays the Schmid factor iso-curves for basal slip. These grains have high Schmid factors for basal slip, which indicates that the facets formed by slip on the (0001) plane. Table 4.5 lists the spatial orientation of facets with respect to the loading axis (RD) and the crystallographic angle with respect to the basal pole for each of the facets marked

**Table 4.5:** Spatial Orientation of Facet Normals and Crystallographic Orientation of Basal Poles

| Facet Number | 1* | 2 | 3 | 4 |
|---|---|---|---|---|
| Spatial Orientation (w.r.t. tensile axis) | 44 | 42 | 25 | 15 |
| Crystallographic Orientation ([0001]w.r.t. tensile axis) | 51 | 50 | 30 | 13 |

in the micrograph. As shown in Table 4.5, the spatial and crystallographic angles follow the same trend and the facet normal is aligned with the basal pole of these grains. Facet 1 is a unique case, since it is not a facet which formed in a $\alpha_p$ grain. As shown in the IPF map in Figure 4.22, this feature, which appears as a facet on the fracture surface, is in fact a region of transformed $\beta$ material. The crystallographic and spatial measurements still indicate that this failure results in a facet parallel to the basal plane.

The repeatability of the OIM measurements is reliable to within $\pm 3^{\circ}$, which agrees with what Davidson et al. [58] found and the accuracy of the measurements from stereo pairs was found to be roughly the same. Therefore, within the accuracy of the experimental techniques, the facets appear to form within a few degrees of the basal plane. These results indicate that basal slip is operative in a number of grains at the crack initiation site, and this raises the question of whether a critical number of $\alpha_p$ grains oriented for basal slip is necessary to cause fatigue crack initiation in these locations.

### 4.4.2 Characterization of Texture in Crack Initiating Neighborhoods

Observation of the material around the crack initiation site reveals that the majority of alpha phase material, including lath $\alpha$ and equiaxed $\alpha_p$ grains, is oriented for either basal or prism slip. An inverse pole figure (IPF) map of the RD-TD plane for a typical crack initiation site is shown in Figure 4.23. LeBiavant and coworkers [48] argue that the texture of these regions promotes plastic deformation in the crack initiating grains. The likelihood

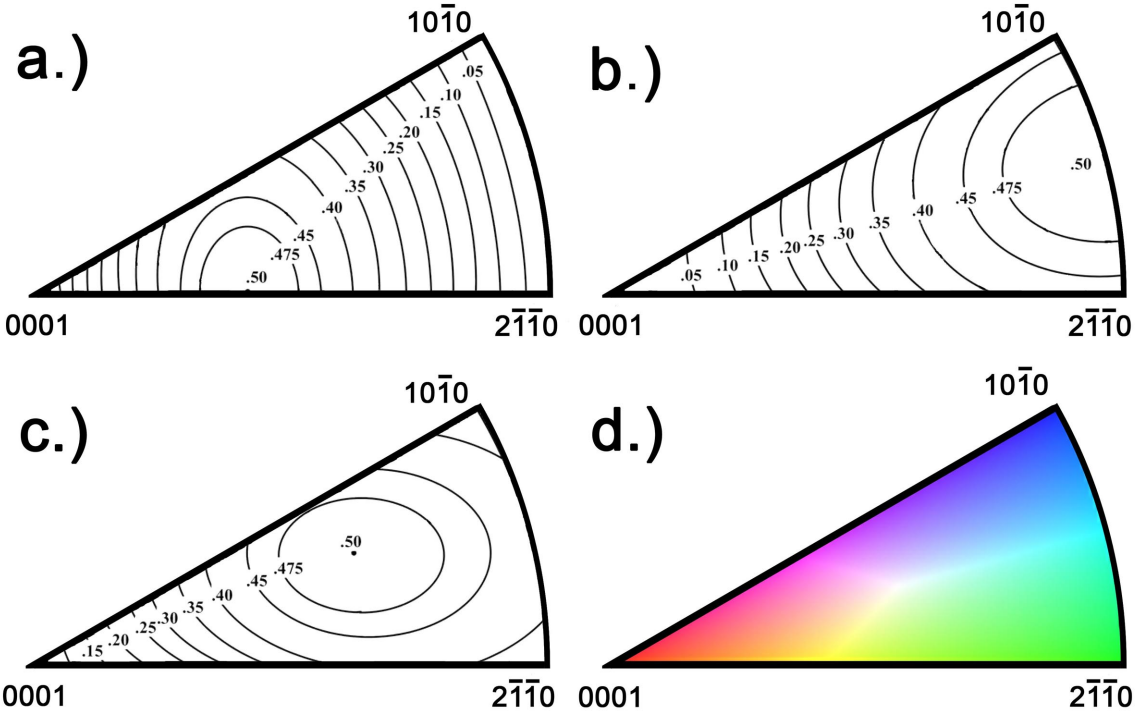


**Figure 4.20:** The Schmid factor contours are superimposed on the inverse pole figures corresponding to (*a.*) basal, (*b.*) prism, and (*c.*) pyramidal slip. (d.) shows the legend for the inverse pole figure maps. The inverse pole figures in this figure have been orieted such that the basal pole is parallel to the tensile axis.

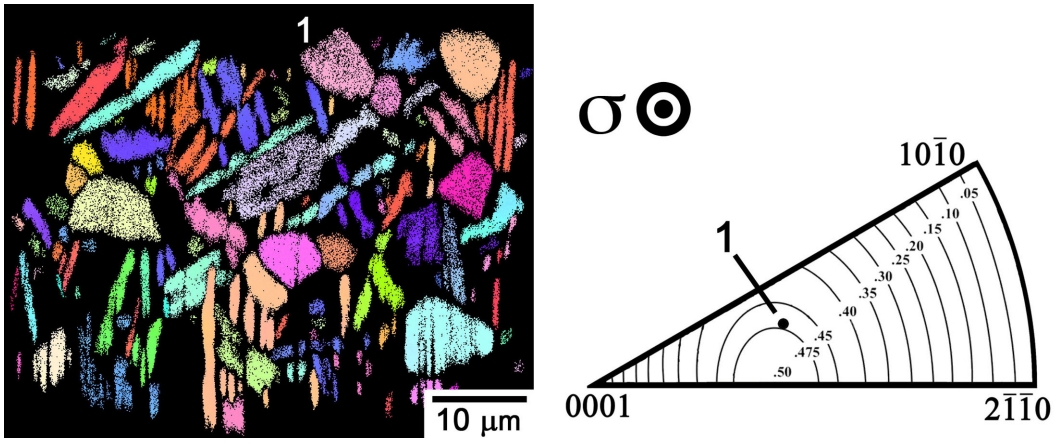


**Figure 4.21:** The IPF map for a specimen that failed from a surface initiated crack, which illustrates that slip along a basal plane is also active in surface crack initiation.

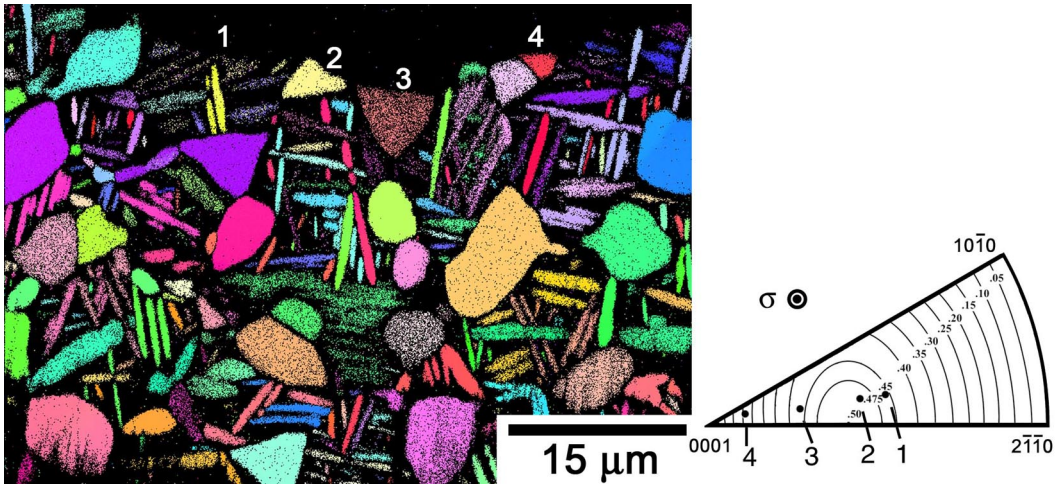


**Figure 4.22:** This figure illustrates the crystallographic orientation of $\alpha_p$ grains that have failed by faceted fracture. The spatial orientation of the facet poles have been plotted in the inverse pole figure, which also shows the contour lines of the Schmid factor for basal slip.

of finding a group of $\alpha_p$ grains with similar crystallographic orientations suitable for basal slip is believed to be higher in these textured regions, as opposed to a random area with no preferred (i.e., random) crystallographic texture [48, 49]. As shown in Figure 4.23a the textured regions are as large as 300-500 $\mu$m in size, which is the approximate dimension of the initial $\beta$ grain size. Figure 4.23b displays only the $\alpha$ phase material that is highly oriented for basal slip, and most of these grains are concentrated near the fatigue crack initiation site. The texture of the $\beta$ phase is shown in Figure 4.23c, and this image shows that one large region of $\beta$ phase material exists near the crack initiation site. Thus, the observed $\alpha$ phase texture near fatigue crack initiation sites clearly results from the texture of the $\beta$ phase developed during thermomechanical processing. Each of the initiation types observed in this study exhibit different preferred textures.

Figure 4.24 displays representative inverse pole figures for each of these initiation types. Table 4.6 summarizes the typical observations at the three different fatigue crack initiation sites. An inverse pole figure of a surface initiated failure is shown in Figure 4.24a. This IPF corresponds to the IPF map shown in Figure 4.21 and the texture is suitable for basal

slip, but there is no peak in the inverse pole figure corresponding to prism slip. Also, the texture in these surface initiated failures is relatively weak compared with the other initiation mechanisms. The texture near sites of subsurface crack initiation with isolated facets is illustrated with the inverse pole figure in Figure 4.24b, and the texture in these regions is clearly suited for both basal and prism slip. This IPF was generated from the IPF map shown in Figure 4.23 using just the grain orientations observed in the top portion of the scan near the site of fatigue crack initiation. The legend for this IPF indicates that the texture is quite strong compared to the other initiation types observed being on the order of 6 times random. A typical IPF of the third characteristic crack initiation type is shown in Figure 4.24c, and it is apparent that the texture in this microstructural neighborhood is weaker, as evidenced by the lower intensity values shown in the legend and the presence of multiple intensity peaks within the inverse pole figure.

It should be noted that the size of the microstructural areas used to generate the inverse pole figures shown in Figure 4.24 varies, and thus it is difficult to make a clear comparison of the textures from one mechanism to the next. Only small areas can be analyzed in surface failures, since the OIM scan is being performed on a curved surface and the successful indexing of Kikuchi patterns is very sensitive to surface orientation. Despite these limitations, the fact remains that only textures suitable for basal slip are observed in surface initiated failures, while textures suitable for basal and prism slip are found in subsurface initiation with isolated facets, and no preferred texture is observed in subsurface crack initiation with contiguous facets. These microstructural configurations can be ranked in order of increasing resistance to fatigue crack initiation when examining these inverse pole figures and Figure 4.11. At the highest stress levels of 650 and 700 MPa, the subsurface contiguous faceted initiation sites are associated with the longest fatigue lifetimes. This is reasonable in light of the texture measured in these regions, since the texture does not appear to be highly oriented for activation of either of the easy slip systems (prism and

basal) in hcp titanium. Thus, a longer fatigue lifetime is expected since these regions are not as favorably oriented for the accumulation of irreversible cyclic slip. At 600 MPa, they are observed to have roughly the same fatigue lifetimes as subsurface isolated faceted initiation sites. This may indicate slower cyclic strain accumulation in the subsurface isolated facets at lower stress amplitudes, or it may be an artifact of the number of samples that have been tested. As observed at higher stresses, subsurface crack initiation with isolated facets exhibits shorter fatigue lifetimes relative to contiguous faceted failures. This failure type would be expected to have a shorter lifetime than subsurface contiguous faceting, since the texture in these regions is strongly suited for both basal and prism slip, thereby making it easier for irreversible cyclic slip to accumulate in these regions of microstructure. Surface fatigue failures exhibit the shortest lifetimes, which is physcially reasonable since they typically have a large grain or a few grains on the specimen surface oriented for basal slip. Since slip is not constrained at a free surface, irreversible cyclic slip will accumulate more easily in these grains and lead to earlier fatigue crack initiation. These findings agree with published reports stating that surface initiated fatigue cracks are associated with the shortest fatigue lifetimes, while subsurface initiated failures typically exhibit longer fatigue lifetimes [60,125]. This is consistent with the findings in this research, that overall a shorter lifetime will result from a surface initiated failure.

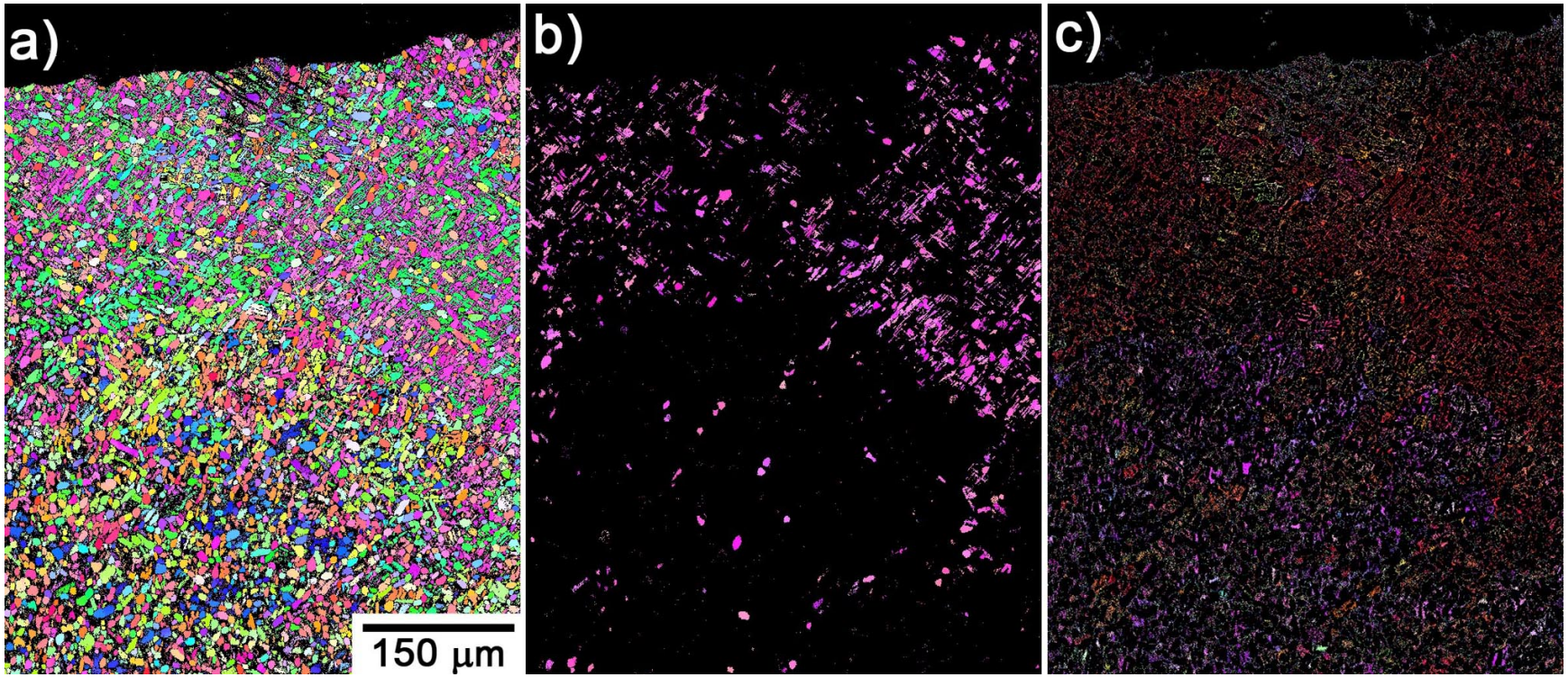


**Figure 4.23:** Example inverse pole figure (IPF) map from an OIM scan near the crack initiation site displaying (a.) the texture of the $\alpha$ phase, (b.) the $\alpha$ grains oriented for easy basal slip, and (c.) the orientation of the $\beta$ phase material.

**Table 4.6:** Texture Intensity as a Function of the Initiation Type.

| | **Surface** | **Subsurface Isolated** | **Subsurface Contiguous** |
|---|---|---|---|
| *Preferred Texture* | Basal Slip | Basal & Prism Slip | None |
| *Texture Intensity* | Medium | Strong | Weak |

### 4.4.3 Comparison of Crack Initiation Regions with Nominal Microstructures

It has been established that regions of material with preferred texture for basal and prism slip are found at the crack initiation site. Random areas far from the crack initiation sites were sectioned to expose the RD-TD plane, as described earlier, and they have been examined using OIM to determine if a preferred crystallographic texture also exists in general microstructural areas. Figure 4.25 illustrates the texture in a randomly selected region of material for a much larger area. In this image, areas with a high degree of preferred texture suitable for basal and prism slip are observed in the nominal microstructure. These regions of preferred texture correspond to the $\beta$ grain texture and morphology. The length scale of these textured regions appears to be 300-500 $\mu$m in size, and this is approximately the size of the $\beta$ grains, which indicates that these textured regions formed in the initial $\beta$ processing steps.

Additionally, the grains oriented for (0001) slip can be plotted separately. It is possible to see that the distribution of $\alpha_p$ grains varies as a function of the original prior $\beta$ grain as shown in Figure 4.25b. Thus, it appears that the presence of a preferred texture suitable for basal and prism slip is a necessary, but not sufficient, condition for crack initiation. In these regions of preferred texture, it is clear that the majority of the $\alpha$ phase material shares the same crystallographic orientation. However, the strength of the preferred texture will affect the resistance to fatigue crack initiation. In other words, a weakly textured region of material might not promote crack initiation and propagation as successfully as a suitably oriented region in which nearly all $\alpha_p$ grains and laths are oriented for easy slip.

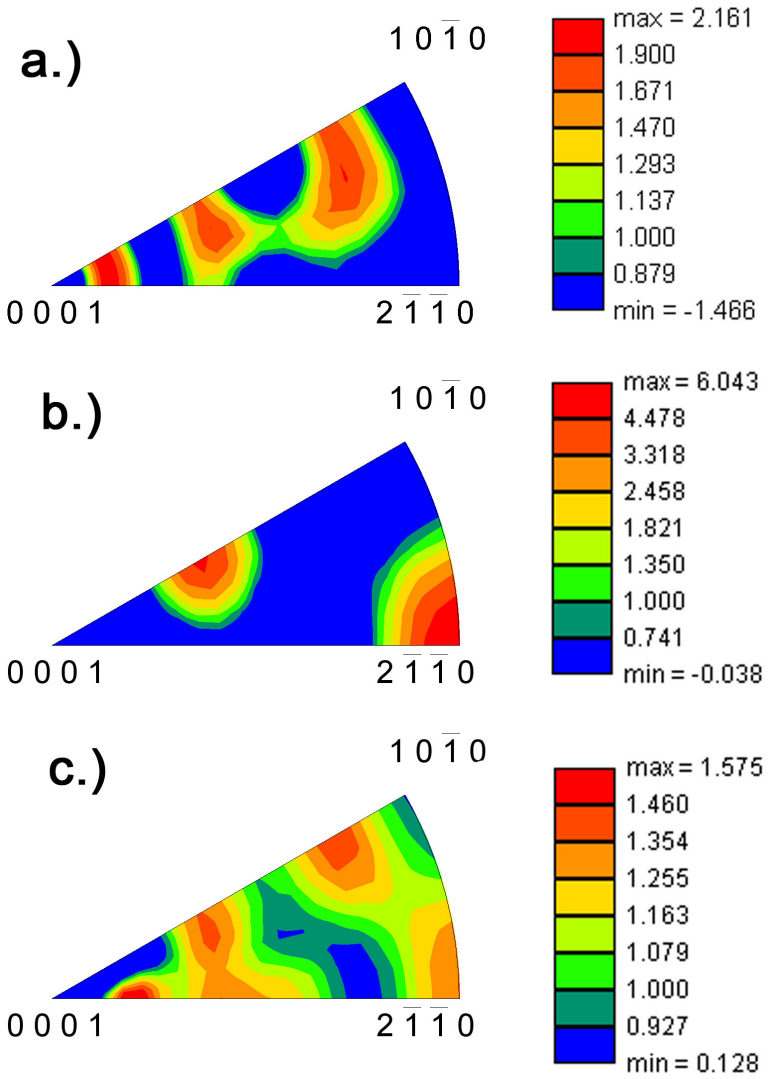


**Figure 4.24:** Inverse pole figures for each of the initiation types; a.) surface initiation, b.) subsurface isolated faceting initiation, c.) subsurface contiguous facet initiation.

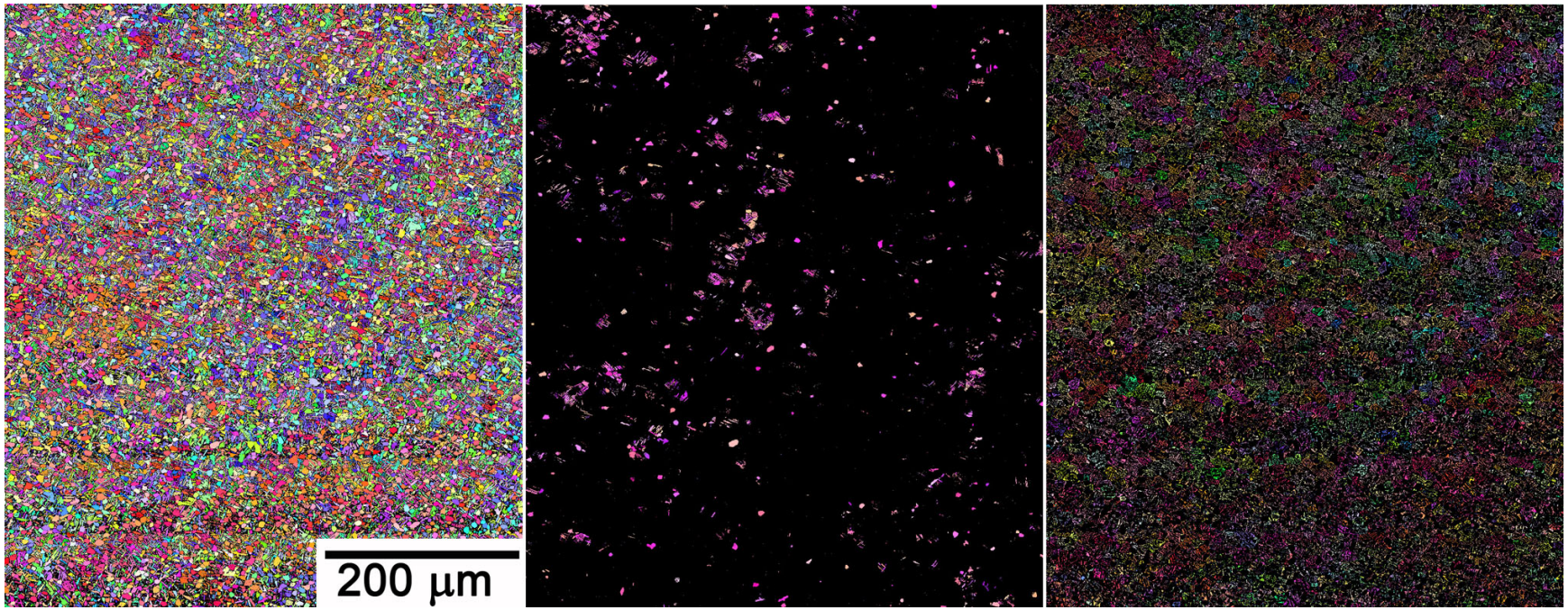


**Figure 4.25:** A typical IPF map from an OIM scan that illustrates large regions of similarly oriented material are commonly found in the general microstructure. (a.) $\alpha$ phase material, (b.) $\alpha$ phase material oriented for easy basal slip, and (c.) $\beta$ phase material illustrating that this texture is inherited from the prior $\beta$ phase.

Thus far, the texture of the $\alpha$ phase, that is the lath $\alpha$ and the $\alpha_p$ grains, has not been considered separately. However, the texture of the lath $\alpha$ and equiaxed $\alpha_p$ phases should be considered separately, since the correlation in the textures of these phases may affect the ease of slip transmission between grains. Figure 4.26 illustrates a fatigue crack initiation site in which the $\alpha_p$ phase has been separated from the lath $\alpha$ phase in the IPF maps, along with their corresponding pole figures. The $\alpha$ phase IPF map and the $\beta$ phase IPF maps are also shown for reference. The lath $\alpha$, as shown in Figure 4.26c, maintain a Burgers orientation relationship with the $\beta$ phase (Figure 4.26b), whereby the basal (0001) plane of the $\alpha$ phase is parallel to the (110) plane of the $\beta$ phase [25], and this is evidenced by the similarity in the pole figures corresponding to these phases. Due to the recrystallization and spherodization processes which form the $\alpha_p$ grains, it is generally assumed that equiaxed $\alpha_p$ are not crystallographically related to the prior $\beta$ grain orientation [32]. Woodfield et al. [30] note that strains on the order of $\epsilon = 1$ are required to dynamically spheroidize the $\alpha$ laths and form $\alpha_p$ grains. Local heterogeneities in the accomodation of the macroscopically imposed strain will result in variations such that a macroscopic strain of $\epsilon = 1$ may still not be high enough to uniformily recrystallize all of the $\alpha$ laths as they spherodize [30, 128]. As suggested by Woodfield et al., the $\alpha_p$ grains may in fact share a crystallographic orientation relationship with the prior $\beta$ phase and hence the lath $\alpha$. As the work of Suri [20] illustrated, for specific orientations, it is observed that slip transmission across phase boundaries may not be hindered due to the Burgers orientation relationship. Some of the $\alpha_p$ grains do maintain a Burgers orientation relationship with the $\beta$ phase, and this fact is exhibited by the similarity of some intenstiy peaks in the pole figures for these two phases in Figure 4.26b and d. The pole figures in Figure 4.26b and d exhibit similar intensity peaks, however these peaks are much sharper in the (110) $\beta$ phase pole figure. The fact that the intensity peaks are spread over a larger area in the (0001) $\alpha_p$ phase pole figure is evidence that this material shared the same original orientation, but the forging and heat treatment processes

have caused rotation/recrystallization of these $\alpha_p$ grains relative to the prior $\beta$ phase. The significance of whether $\alpha_p$ grains maintain the Burgers orientation relationship with the $\beta$ phase in fatigue crack initiation is the subject of the next section.

## *4.5 Analysis of Texture at Fatigue Crack Initiation Sites*

The results presented in Figures 4.22 and 4.23 clearly depict the presence of microtextured regions suited for easy basal and prism slip throughout the microstructure at the site of fatigue crack initiation, however regions of microtexture similar to this are commonly found in random sections of material as illustrated in Figure 4.25. Thus, as the presence of microtexturing is not a distinctive characteristic of the fatigue crack initiation sites, it appears that subtler aspects of these textured regions must exist that enhance the susceptibility of these regions to cyclic damage accumulation and fatigue crack formation. Therefore, the remainder of this section details experimental work that attempts to quantify numerous aspects of these fatigue crack initiation sites. Specifically, the area fraction of lath and $\alpha_p$ phases, the presence of $\alpha$ phase material concentrated within each of these phases, and the prevalence of the $\alpha_p$ grains in these regions sharing a Burgers orientation relationship with the parent prior $\beta$ phase have been measured. Measurements of these features observed at fatigue crack initiation sites is intended to yield insight regarding the mechanism of damage accumulation and the significance of slip transfer between the lath and equiaxed $\alpha$ phases leading to fatigue crack initiation. The following analyses have been completed as an assessment of the degree of microstructural heterogeneity observed across various fatigue crack initiation sites. The measurement of these features will be examined to determine if any of these features correlate with lifetime. These data will also be integrated into the development of a model of fatigue damage accumulation in these microstructural neighborhoods.

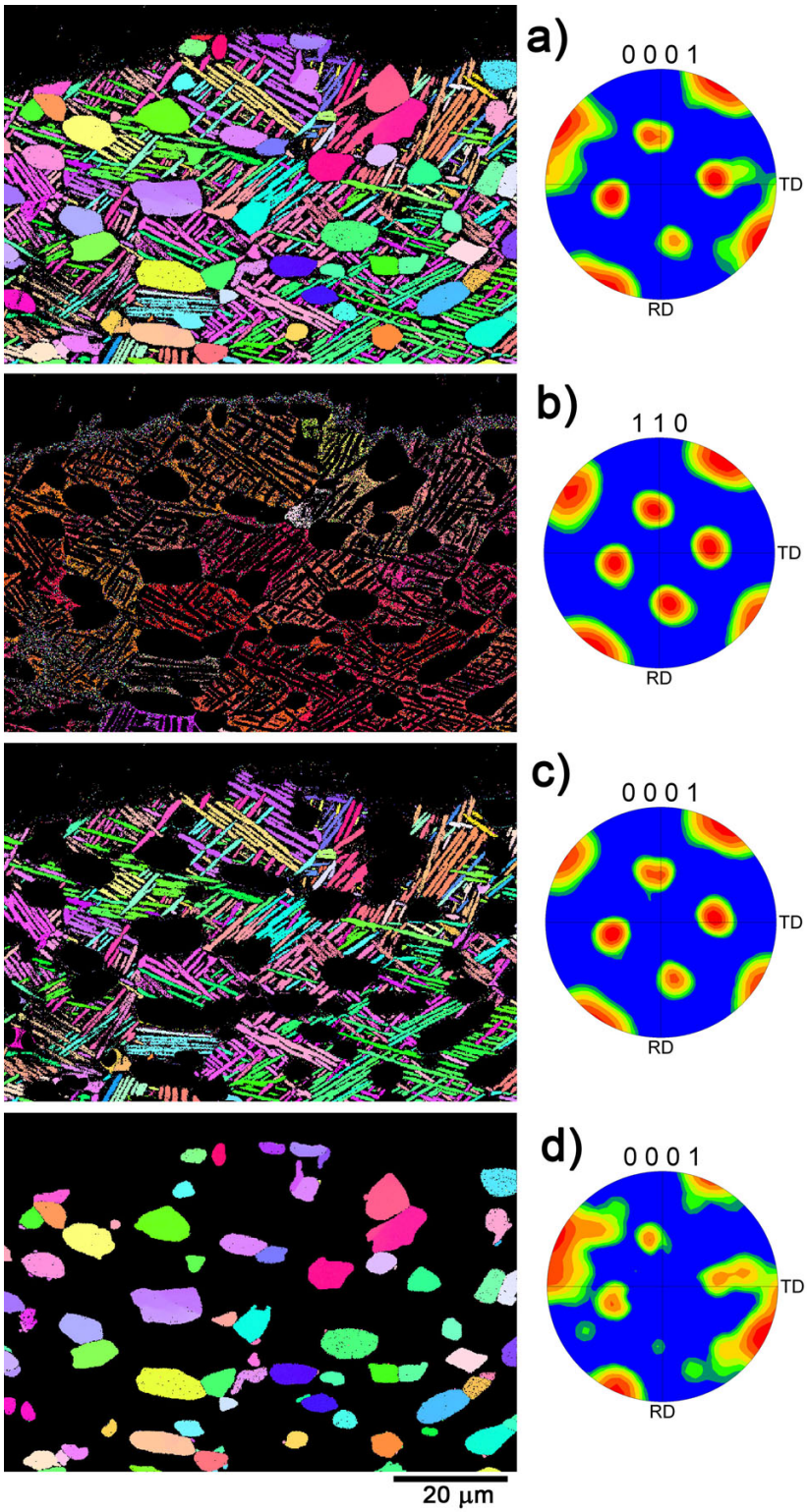


**Figure 4.26:** The (a)$\alpha$ phase, (b)$\beta$ phase, (c)lath $\alpha$, and (d)$\alpha_p$ phase IPF maps and corresponding pole figures are displayed for an OIM scan acquired near a fatigue crack initiation site.

### 4.5.1 Variation in Texture within Lath and Equiaxed Alpha Phases

The data from OIM scans has been segmented by particle morphology, as described in Section 3.4.6, to separate the lath and equiaxed $\alpha$ phases for characterization. In an effort to distinguish the crack initiation sites from the general microstructure, a number of features have been quantified.

First, the area fractions of the lath $\alpha$ and $\alpha_p$ were measured to determine how the distribution of these phases compares with the distribution of these phases within nominal microstructural areas. Figure 4.27 is a plot of the area fraction of these two phases for a number of fatigue crack initiation sites and for nominal microstructural areas. This data is plotted against lifetime to failure to ascertain whether these features could be used as a metric for susceptibility to fatigue crack initiation as well as a means for distinguishing initiation sites from nominal areas. As the plot illustrates, the material at the fatigue crack initiation sites is not much different than the material observed in random microstructural areas. Namely, the area fractions of lath and $\alpha_p$ material overlap with the measurements taken from random microstructural areas. This observation offers additional evidence for the conclusions from Section 4.3.2 that clusters of $\alpha_p$ grains are not necessary for fatigue cracks to initiate.

In addition to quantifying the area fraction of the individual $\alpha$ phases, the presence of textures suitable for basal and prism slip has been quantified to determine if the majority of the $\alpha$ phase material is oriented for either of these slip systems as found in Section 4.4.2. Basal slip is operative in facet formation, however as the inverse pole figures in Figure 4.24 illustrate, these regions also have some grains favorably oriented for prism slip. A plot illustrating these measurements is shown in Figure 4.28 and it is clear from this plot that the amount of material preferentially oriented for activation of basal and prism slip

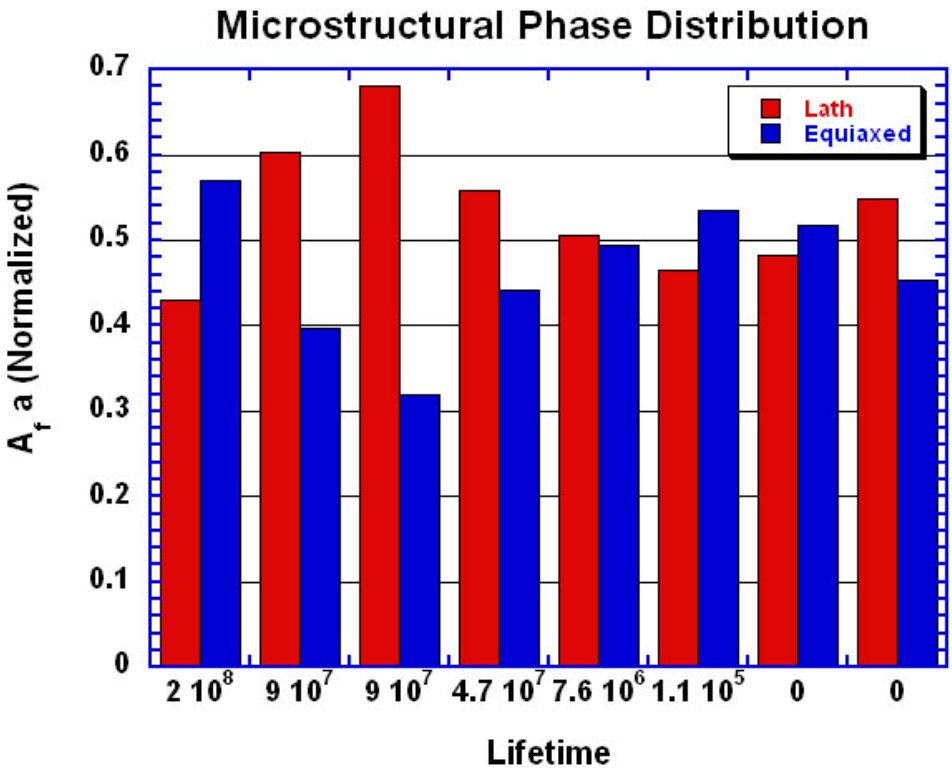


**Figure 4.27:** A plot of the area fraction of lath $\alpha$ and $\alpha_p$ at the crack initiation sites compared with that in two nominal microstructural areas.

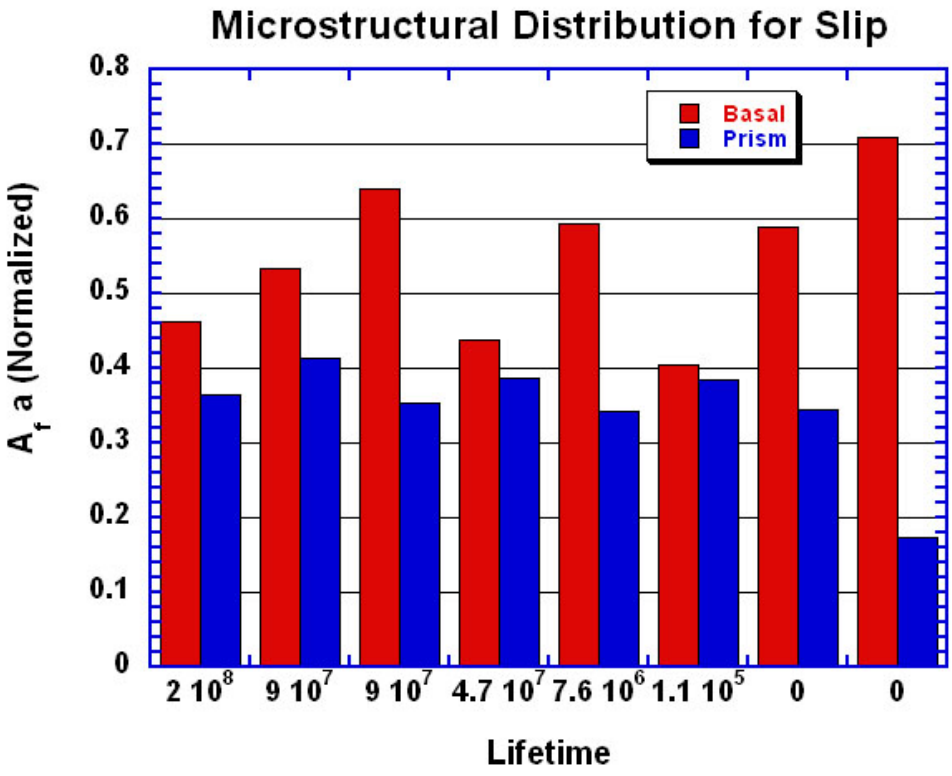


**Figure 4.28:** A plot of the area fraction of material oriented for basal and prism slip at the crack initiation sites compared with that in two nominal microstructural areas.

is essentially equal for the initiation sites. Additionally, in comparison with nominal microstructural areas it is clear that fatigue crack initiation sites are not distinguishable based on these metrics. There is a higher likelihood of finding material oriented for basal slip, but as the measurements for the nominal microstructure illustrate, this is also found to be true throughout the microstructure. Furthermore, the area fraction of these textural components does not vary in any meaningful way as a function of fatigue lifetime. Therefore, it is not possible to say that the presence of material oriented for basal or prism slip is more significant in terms of driving fatigue crack initiation.

Figure 4.29 illustrates the probability that material is lath or equiaxed $\alpha$ given that it is oriented for a specific type of slip. For example, the red bars depict the area fraction of material that is lath $\alpha$ given that it is oriented for basal slip. Thus, for the specimen

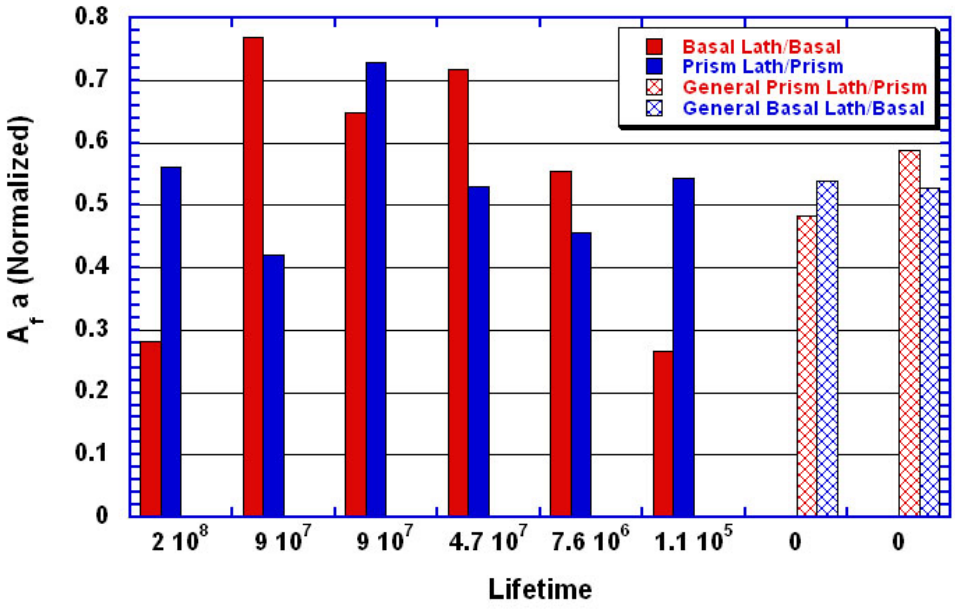


**Figure 4.29:** A plot of the area fraction of phase given that material is oriented for a specific type of slip at the crack initiation sites compared with that in two nominal microstructural areas.

with a lifetime of 2 x $10^8$ cycles, approximately 29% of the material oriented for basal slip is found in the lath $\alpha$ phase and conversely this implies that of the material oriented for basal slip, 71% is found in the equiaxed $\alpha_p$ phase. The only trend observed in this plot is that fatigue crack initiation sites with shorter fatigue lifetimes display a smaller percentage of lath $\alpha$. There is an obvious outlier; the specimen that failed after 2 x $10^8$ cycles had a very low area fraction of material oriented for basal slip in the lath $\alpha$ phase. Allowing that this data point is anomolous and that the trend is real, these measurements would suggest that if the material oriented for basal slip is found in the $\alpha_p$ phase, a shorter fatigue lifetime can be expected. This observation appears to agree with the findings of other researchers [51,54], since it would suggest that larger $\alpha_p$ grains are more susceptible to fatigue damage accumulation and crack formation due to their longer slip length.

### 4.5.2 Significance of Burgers Orientation Relationship in Fatigue Damage Accumulation

Others have shown in monotonic deformation experiments [20] that in some cases, the $\alpha/\beta$ phase boundary does not provide an effective barrier to slip transfer between the $\alpha$ and $\beta$ phases as a result of the alignment of slip planes in the hexagonal and cubic phases described by the Burgers orientation relationship. Specifically, Suri and coworkers observed that this interface was susceptible to slip transfer when grains were favorably oriented for the activation of slip on the $a_1$ and $b_1$ directions. This is reflected in the difference of CRSS values presented for $a_1$- and $a_2$-type prism slip in Table 2.1. To investigate whether slip transfer between $\alpha$ and $\beta$ grains is a critical factor in the fatigue damage accumulation process, the procedure described in Section 3.4.7 has been used to calculate the misorientation between the predicted $\alpha_p$ grain orientation and the adjacent parent $\beta$ grain. The results of this investigation are shown in Figure 4.30. Since most $\alpha_p$ grains are surrounded by a number of prior $\beta$ grains, the data points in this plot reflect the misorientation between a given $\alpha_p$ grain and the adjacent $\beta$ grain that represents the minimum deviation from the Burgers orientation relationship. Open data points correspond to $\alpha_p$ grains within the initiation volume and closed data points represent the orientations of the grains in which $\alpha_p$ facets have formed. This plot illustrates that a majority of the $\alpha_p$ grains within the initiation volume are not related to the prior $\beta$ grain orientation by the Burgers orientation relationship. If these grains did maintain the Burgers orientation relationship, the measured minimum possible misorientation would be on the order $1^\circ$ as observed in the work of Mills et al. [28]. Furthermore, and of more interest, is the observation that the $\alpha_p$ grains that form facets do not maintain the Burgers orientation relationship with the prior $\beta$ phase. The observation that the Burgers orientation relationship is not maintained suggests that slip transfer across the $\alpha/\beta$ phase interface is effectively inactive as a mechanism of damage accumulation.

This data also provides insight into the processing conditions in these localized regions.

Clearly, the loss of the orientation relationship between the $\alpha_p$ phase and the parent $\beta$ grains indicates that the local forging strains were at least as high as $\epsilon$ =1 and that these grains formed through a process of dynamic spherodization. For further insight into the local processing coniditions, the same misorientation data is plotted as a function of the grain size measured from the OIM scan of this section in Figure 4.31. This was investigated since it stands to reason that the larger $\alpha_p$ grains would have begun to spherodize earlier in the forging process than the smaller $\alpha_p$ grains. As a result, these large grains would have accumulated more deformation during the forging process and are therfore more likely to have recrystallized during the thermomechanical processing steps. However, this relationship is not observed in the data. This demonstrates that $\alpha_p$ grains which formed late in the thermomechanical processing are no more likely to maintain the Burgers orientation relationship than the $\alpha_p$ grains, which formed later in the forging process.

For comparative purposes, the deviation of the $\alpha_p$ and $\beta$ grains from the Burgers orientation relationship was investigated in nominal microstructural areas as well. These results are shown in Figure 4.32, which is a plot of the misorientations of the $\alpha_p$ grains with respect to the closest predicted beta phase orientation for random microstructural areas. As indicated, the measured misorientations of the $\alpha_p$ grains in the general microstructure are randomly distributed across a range of values, which is similar to what has been observed at fatigue crack initiation sites. Furthermore, the misorientation measurements do not exhibit an observable trend with respect to the $\alpha_p$ grain size. This is illustrated in Figure 4.33, which is a plot of the misorientation against the $\alpha_p$ grain size. Since the misorientation measurements at fatigue crack initiation sites and within the general microstructure exhibit the same characteristics, this metric is not capable of distinguishing initiation sites from general microstructural areas.

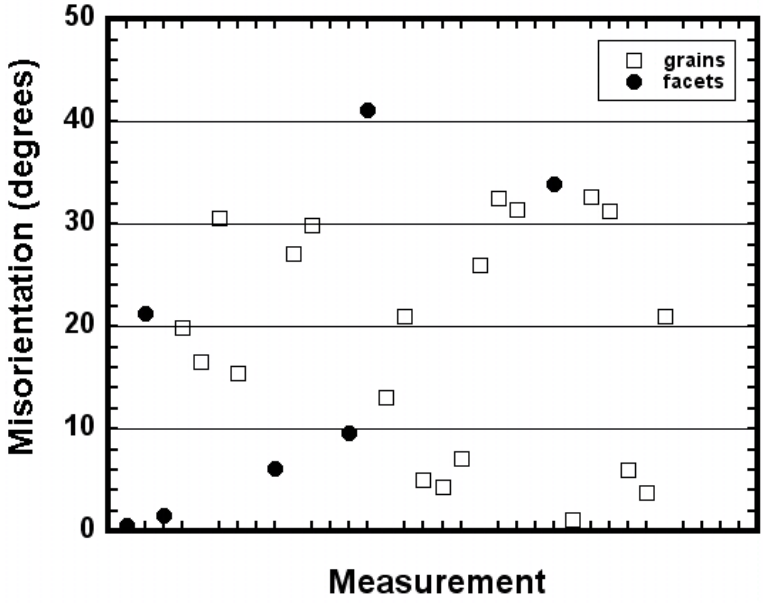


**Figure 4.30:** Measurements of $\alpha_p$ grain misorientations relative to initial $\beta$ phase orientation near fatigue crack initiation sites.

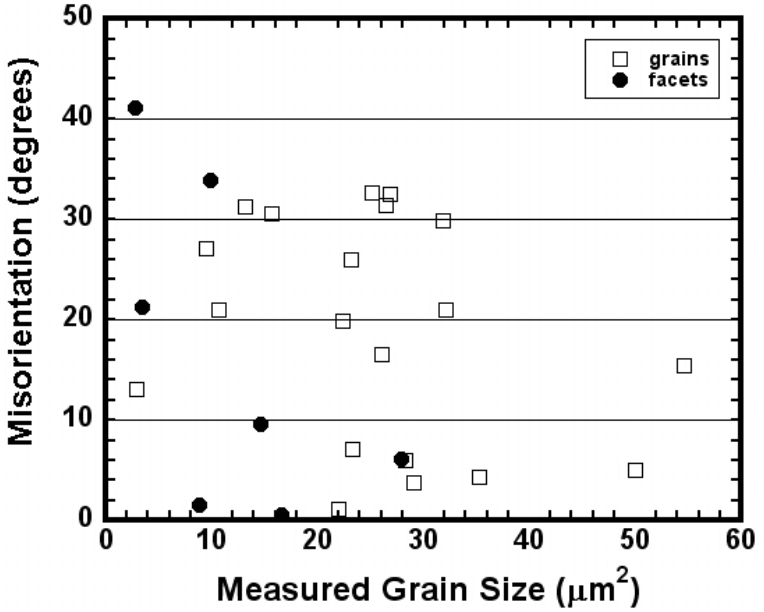


**Figure 4.31:** Measurements of $\alpha_p$ grain misorientations relative to initial $\beta$ phase orientation near fatigue crack initiation sites. These measurements are plotted against the grain size measured from this section.

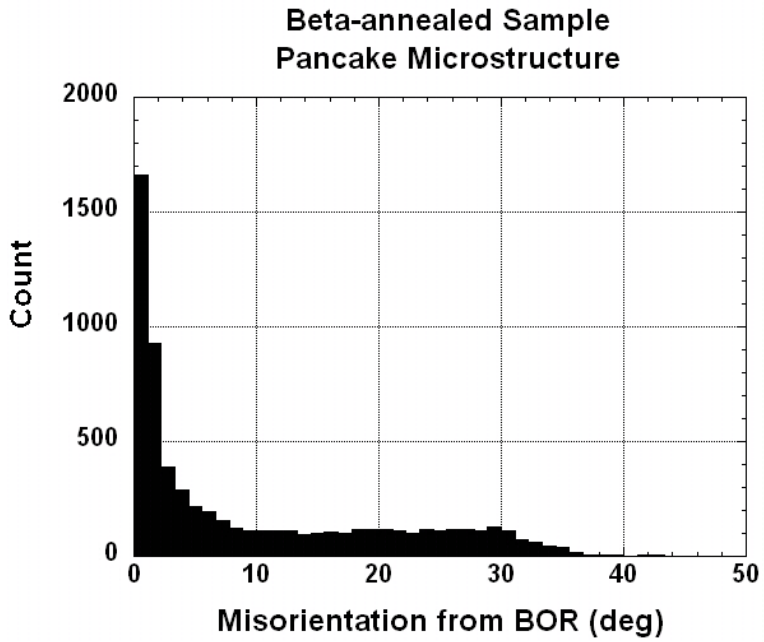


**Figure 4.32:** Measurements of $\alpha_p$ grain misorientations relative to initial $\beta$ phase orientation in general microstructural regions.

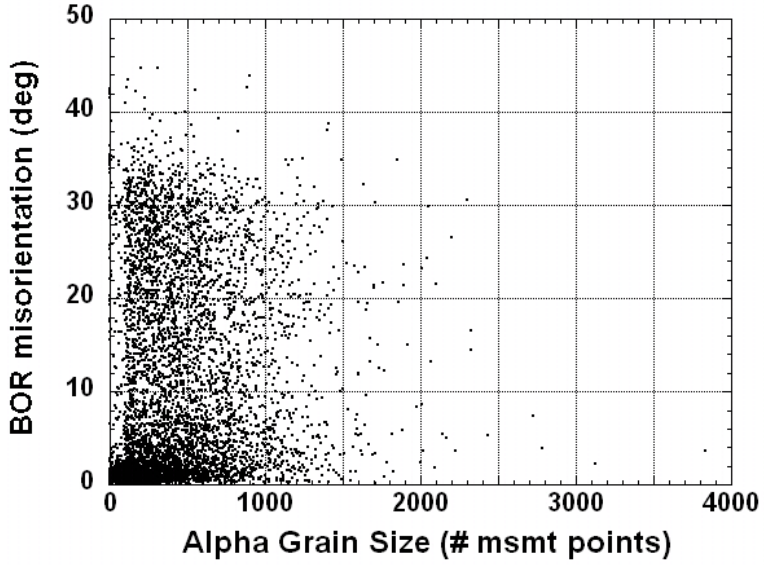


**Figure 4.33:** Measurements of $\alpha_p$ grain misorientations relative to initial $\beta$ phase orientation in nominal microstructural areas. These measurements are plotted against the grain size measured from this section.

## *4.6 Mechanism of Fatigue Crack Initiation*

Figure 4.34 is a schematic that depicts the proposed mechanism of subsurface fatigue crack initiation that is consistent with the observations in this study. The $\alpha_p$ grains are shown in the schematic, while the lath $\alpha$ is not drawn, but assumed to have crystallographic orientations as predicted by the Burgers orientation relationship. The larger grayscale regions are drawn to illustrate the $\beta$ grains. Each of the images depict the stages of fatigue damage accumulation in microstructural neighborhoods which ultimately leads to fatigue crack initiation. Figure 4.34 (a) illustrates the general microstructure, which is free of deformation and slip accumulation, while (b) depicts the accumulation of slip in a few $\alpha_p$ grains. Figure 4.34 (c) shows the intensification of slip in those initial grains and the initiation of slip deformation in a few adjacent $\alpha_p$ grains. The last stage, as shown in Figure 4.34 (d) indicates that a crack has initiated from the linkup of these related slip events. This proposed mechanism is based on the fractographic evidence that crack initiation takes place across a number of $\alpha_p$ grains, typically over a region of 40-70 $\mu$m in diameter. The facets that form on the fracture surface result from slip deformation on and eventual separation of the basal plane in $\alpha_p$ grains. Additionally, as shown in Figure 4.23, it appears that these $\alpha_p$ grains are contained within one large $\beta$ grain and that many of them have similar crystallographic orientations. Since a majority of $\alpha_p$ grains within these regions have similar crystallographic orientations, it is presumed that if slip can accumulate in one of these grains, it will likely be able to accumulate in a number of $\alpha_p$ grains within the $\beta$ grain. Likewise, the lath $\alpha$ are known to be oriented for slip deformation in these regions and are presumed to accumulate slip and contribute to the general fatigue damage accumulation in these microstructural regions.

The proposed mechanism can be generalized to explain the process of fatigue crack initiation for the three types of crack initiation sites that were observed. In the case of

surface crack initiation, faceted fracture of $\alpha_p$ grains is still observed, and the mechanism is essentially the same. However, the size of the faceted region is smaller for surface failures than it is for subsurface crack initiation sites. Therefore, the same mechanism is believed to be applicable, but fewer $\alpha_p$ grains are required to accumulate cyclic strain, since surface connected cracks can be smaller than subsurface cracks and still propagate at the same rate due to differences in stress intensity and environmental contributions at these sites. In subsurface macroscopically planar failures, the whole faceted region has the same spatial orientation with respect to the loading axis. This indicates that the $\alpha_p$ grains and lath $\alpha$ colonies within the crack initiation region all have a similar crystallographic orientation. The noticeable feature of these initiation sites is that they appear to form from the faceted fracture of transformed $\beta$ regions of material. There are clearly $\alpha_p$ grains in that area, however, the slip planes of $\alpha_p$ grains and transformed $\beta$ regions of material must be aligned such that the grain boundaries between these phases are not distinguishable on the fracture surface. For these types of failures, it is still thought that slip must accumulate in a number of $\alpha_p$ grains or transformed $\beta$ regions in order to initiate a fatigue crack.

A similar explanation for crack initiation has been postulated in the work of LeBiavant et al. [48] on the microstructural influences of bending fatigue in Ti-6Al-4V. They observed that cracks initiate in macrozones, which are defined as regions of material in which the majority of $\alpha_p$ grains have a similar orientation. In the macrozone that initiated the dominant fatigue crack, multiple microcracks were observed. They postulated that the dominant fatigue crack grew out of these macrozones due to microcrack coalescence. In the current work, there is no evidence of slip offsets or microcracks in $\alpha_p$ grains aside from those on the fracture surface. Fatigue damage is believed to accumulate throughout these similarly oriented regions of material and slip activity in neighboring grains may facilitate crack initiation and growth. However, no evidence of other cracks is observed and thus crack coalescence is not believed to significantly affect crack growth rates. This difference

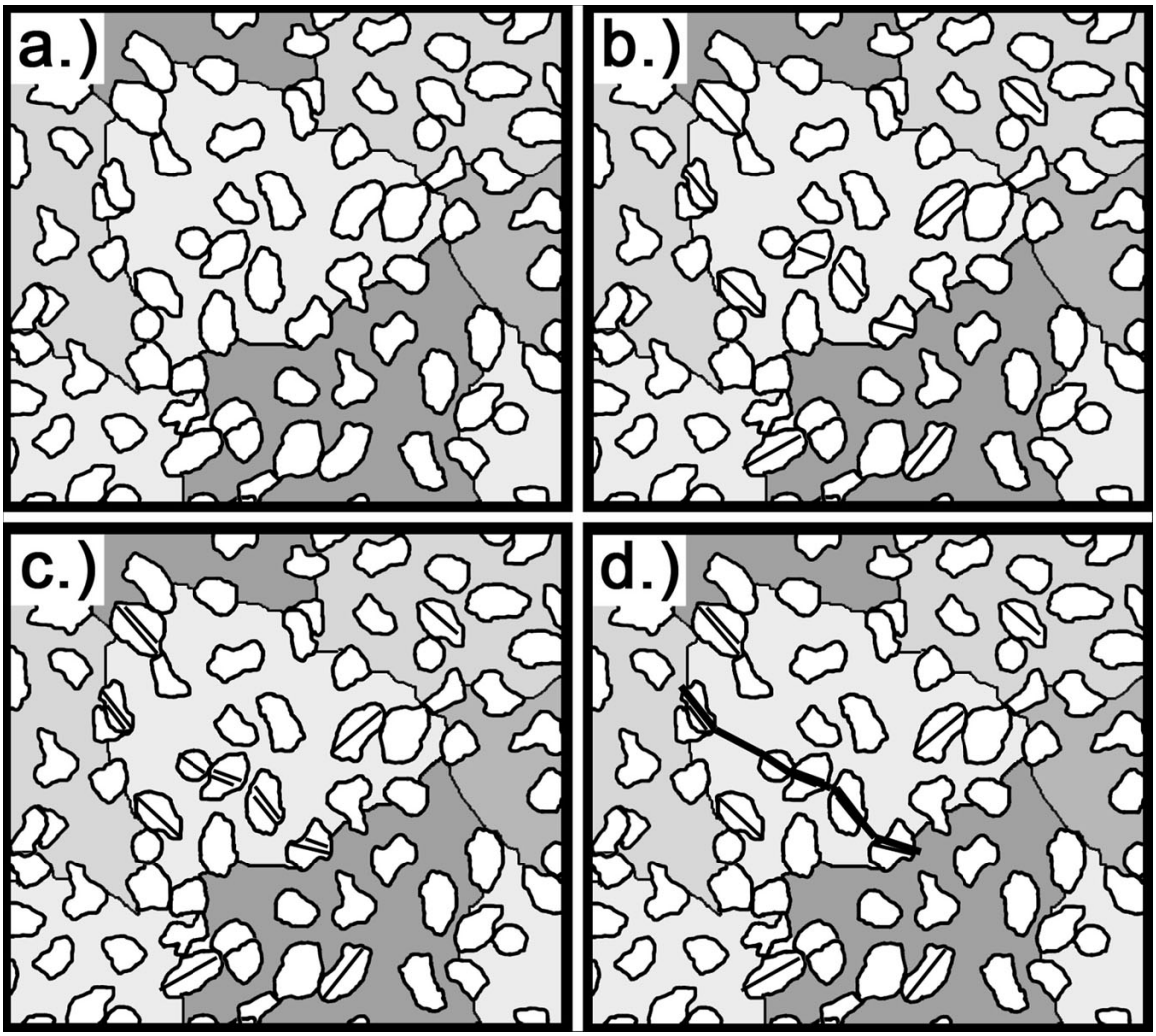


**Figure 4.34:** A schematic depiction of the crack initiation process. a.) illustrates the microstructure before any fatigue cycles have been applied. b.) depicts slip accumulation in a few favorably oriented $\alpha_p$ grains. c.) demonstrates the intensification of slip within ceratin $\alpha_p$ grains and slip accumulation within neighboring grains as well. d.) illustrates the formation of a crack within the microstructure.

may be due to the fact that LeBiavant et al. [48] performed their tests at 800 MPa in a material with a yield strength of 850 MPa, while the current investigation focused on the fatigue behavior at much lower stresses in the range of 0.4-0.6 of $\sigma_{YS}$, where it is unlikely that slip activity would intensify to such an extent that fatigue cracks would initiate in other $\alpha_p$ grains.

## *4.7 Summary and Conclusions*

Ultrasonic fatigue at a load ratio of 0.05 and stresses ($\sigma_{max}$) in the range of 500-700 MPa has been shown to produce failures that display similar trends in lifetime and fractographic appearance with respect to conventional frequency fatigue. Three characteristic types of fatigue crack initiation sites have been identified; surface, subsurface with isolated faceting, and subsurface with contiguous facets. Surface initiated failures exhibit the shortest lifetimes, while subsurface failures tend to have slightly longer lifetimes. Cracks initiate in larger than average sized $\alpha_p$ grains, however these grains do not fall in the extreme tails of the $\alpha_p$ grain size distribution. Strain localization within these grains appears to activate basal slip. The initiation process leads to microcrack formation in the $\alpha_p$ grains parallel to the basal plane. Pseudo-cleavage is not operative, since facets are oriented for slip on rational crystallographic planes. Cracks typically form in $\alpha_p$ grains that are oriented for slip on basal planes which are located within neighborhoods where other $\alpha_p$ grains are also oriented for slip. These microstructural configurations appear to be found more often in textured regions. It is believed that the crystallographic orientations of the $\alpha_p$ grains within these microstructural regions encourages the accumulation of deformation in these neighborhoods. However, spatial clustering of $\alpha_p$ grains has been proven not to be the distinguishing microstructural feature at crack initiation sites. Crack initiation sites have a preferred texture, and it is observed that a majority of the grains near the site are oriented for easy basal or prism <a> type slip.

# Chapter 5

# Fatigue crack growth in Ti-6246

In Chapter 4 it was shown that local microstructure plays an important role in the crack initiation process. However, these studies did not allow the determination of the influence of microstructure on the propagation of fatigue cracks after initiation. It is reasonable to expect that local microstructure may influence fatigue crack propagation behavior, especially in the small fatigue crack regime [24, 69–72, 75]. This chapter addresses the small fatigue crack growth behavior of duplex Ti-6246 by using acetate replication to document fatigue crack growth from small artificially produced notches subjected to ultrasonic fatigue.

The main objective of this portion of the study is to determine if certain local microstructures are more susceptible to crack propagation than the nominal microstructure. To investigate this, the microstructural regions at the notch tips have been examined to determine if certain neighborhoods typically encourage fatigue crack initiation. Secondary objectives are to determine the variability in small crack growth rates as a function of both microstructure and cyclic frequency. Finally, fatigue crack growth behavior will be used to predict fatigue life for comparison with measured fatigue lifetimes from the S-N experiments. Since small fatigue cracks often propagate at faster rates than long fatigue cracks for equivalent stress intensity values [69–71], accurate predictions of damage tolerant fatigue lifetimes require consideration of small fatigue crack growth rates. The key experimental approach involves characterizing the microstructure at the tips of numerous artificial notches and relating both lifetime and fatigue crack growth rates to variations in

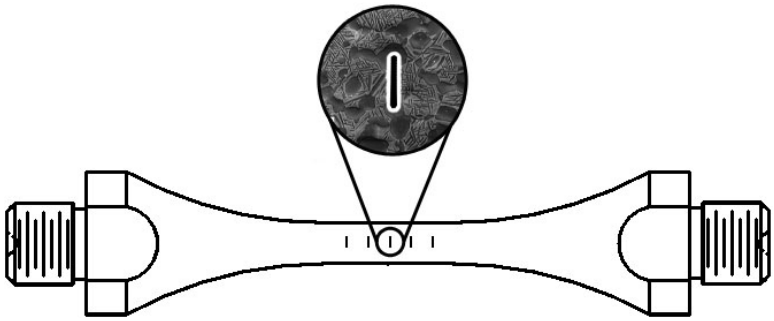

**Figure 5.1:** Specimens used for fatigue crack growth studies; 5 micronotches were machined on each side of the specimen. Not drawn to scale.

microstructure.

Fatigue crack growth rates have been measured from smooth bar fatigue samples that had flat regions machined on opposing sides, as shown in Figure 5.1. To localize fatigue crack initiation, micronotches were machined on the flats of specimens using a femtosecond laser and a focused ion beam microscope (FIB), as described in Section 3.2.3. The laser machined micronotches were larger, with a surface length (2c) on the order of 100 $\mu$m, which was the smallest dimension that could be reproducibly achieved. Much smaller surface notches were produced using the FIB, and these micronotches range in size from 15-40 $\mu$m. Thus, the laser machined defects are appropriate for studying long crack growth behavior at ultrasonic frequencies, while the FIB machined notches were used to examine the role of notch length and microstructural variability at the notch tips on the fatigue crack initiation and small fatigue crack growth behavior.

All fatigue crack growth data collected are shown in Figure 5.2. This plot includes data acquired at 20 Hz from naturally initiated fatigue cracks and at 20 kHz from cracks initiated by FIB and laser-machined micronotches. The red curve in this plot represents a prediction by Larsen et al [116] of the long crack growth rates for R=0.05 based on crack growh rates measured from fatigue testing at other stress ratios from a C(T) specimen. In their work, they fit the experimental data from other stress ratios using Equation 5.1. There

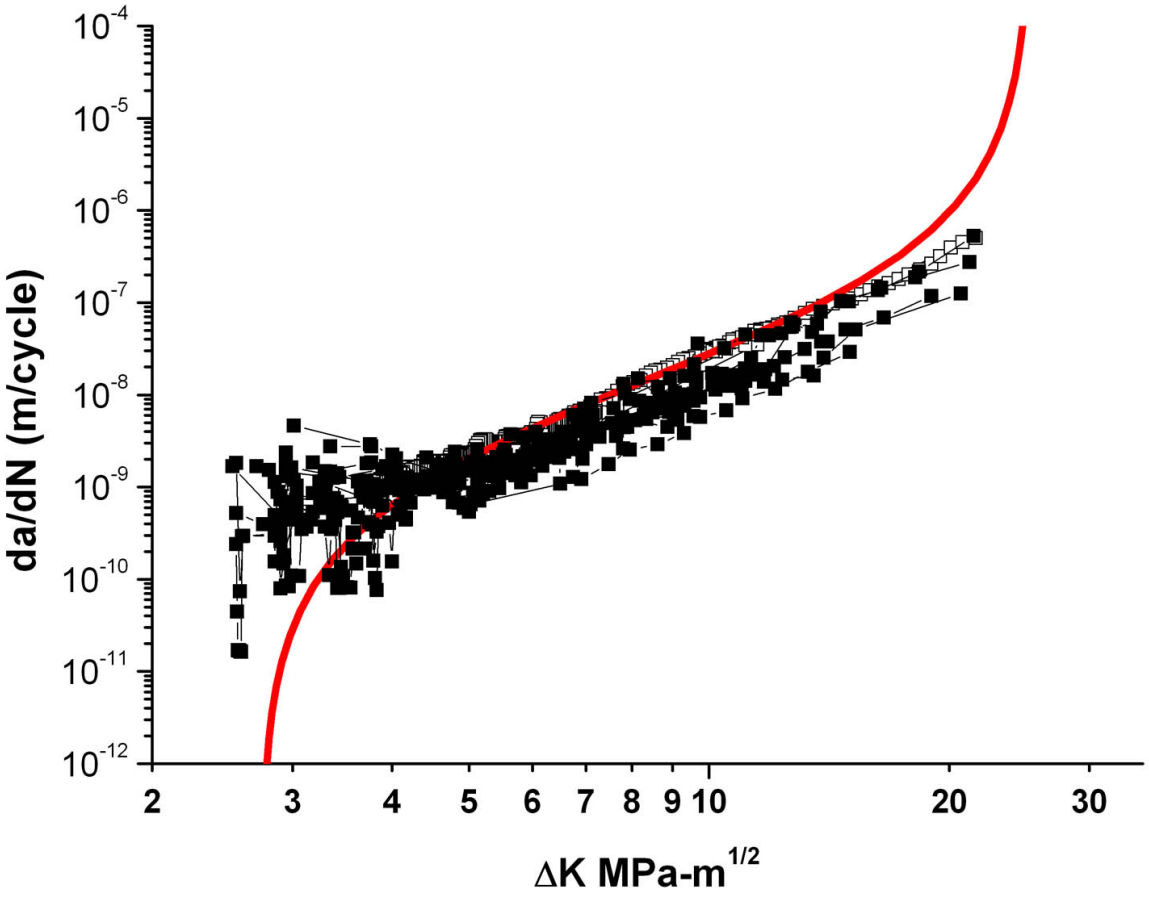


**Figure 5.2:** Fatigue crack growth data acquired at 20 Hz and 20 kHz for both microstructures at room temperature in laboratory air.

is variability in fatigue crack growth rates in the small crack regime, but significantly less in the long crack regime.

$$log(da/dN) = C_1(arctanh(C_2[log(\Delta K) + C_3])) + C_4 \tag{5.1}$$

## *5.1 Long Fatigue Crack Growth*

Long fatigue cracks, or cracks that propagate as predicted by LEFM, were studied using femtosecond laser machined micronotches. In this case, the initial notch surface length was typically on the order of 100 $\mu$m (2c). Figure 5.3 displays a plot of the fatigue crack growth

data as measured from these specimens. All tests were run at R=0.05 in laboratory air. The growth rate of these cracks is very close to the predicted long crack growth rates as shown with the solid red line. The closed data points represent data from fatigue specimens tested at conventional frequencies of 20 Hz. Fatigue crack growth data from ultrasonic frequency tests is illustrated with open data points and these data have similar growth rates as the conventional frequency data and the long crack growth predictions. The 20 Hz tests were run at a stress level ($\sigma_{max}$) of 860 MPa, while the 20 kHz tests were run at stresses ranging from 550-700 MPa. As the data exhibit the same behavior, it is clear that the replication technique can be successfully applied under ultrasonic fatigue loading conditions. There is very little scatter in the fatigue crack growth rates of long cracks and that there is no frequency effect observable between 20 Hz and 20 kHz.

## *5.2 Small Fatigue Crack Growth*

A summary of all fatigue tests for which da/dN data were obtained is shown in Table 5.1. The FIB machined notches enable the observation of small fatigue crack growth behavior and the interaction of these small fatigue cracks with local microstructure. No effect of testing frequency was observed on small fatigue crack growth rates. As expected, the small fatigue crack growth behavior exhibited much more variability than long crack growth rates. This portion of the investigation focused on the interaction of small fatigue cracks with local microstructure. As Table 5.1 illustrates, FIB notches with a surface length of less than approximately 20-25 $\mu$m are unlikely to initiate life-limiting fatigue cracks. The use of multiple FIB notches in every fatigue specimen enabled a direct comparison of the influence of specific microstructural neighborhoods on the cycles required to initiate a crack and the subsequent growth rates. The morphology of the microstructure at the notch tips did not correlate with the lifetime to fatigue crack initiation or subsequent growth rates. However, the earliest notches to initiate a crack exhibited a texture in which there was

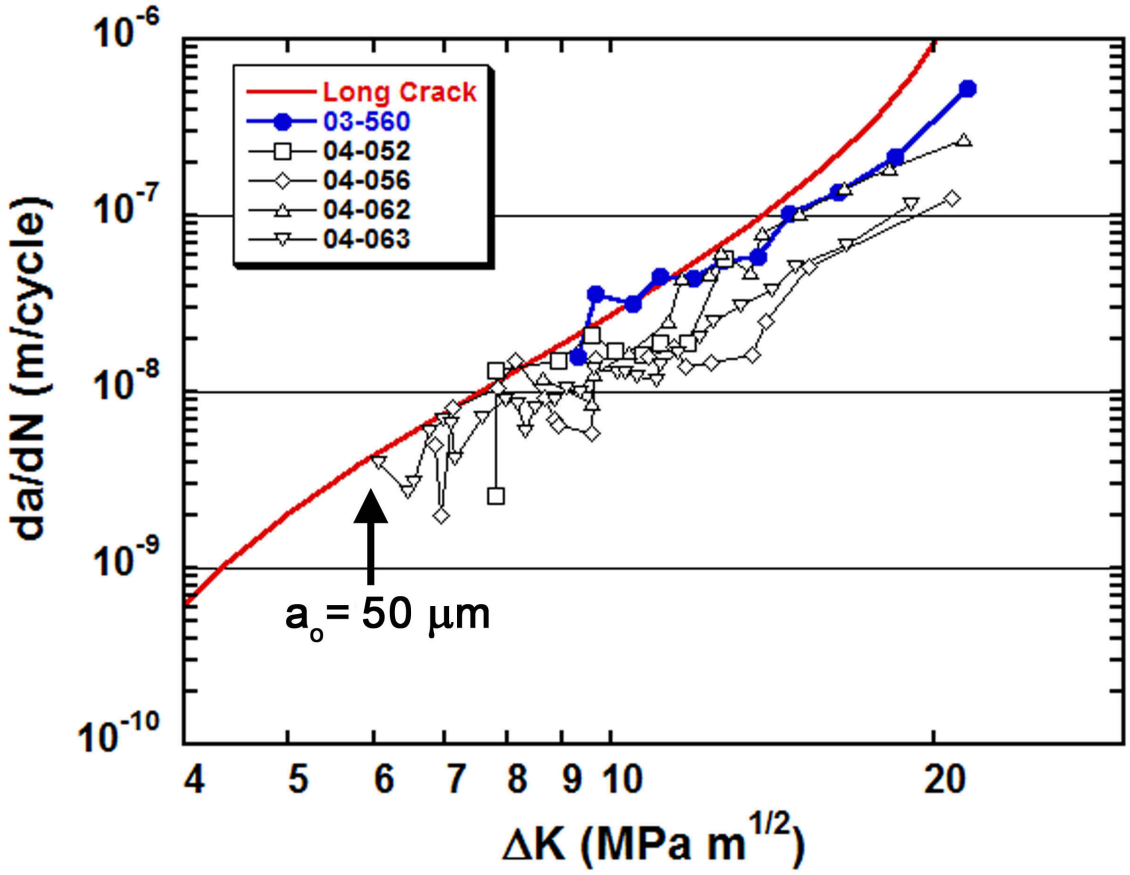


**Figure 5.3:** Fatigue crack growth curves as measured from specimens with femtosecond laser machined micronotches. Closed data points were acquired at 20 Hz, while open data points were measured at 20 kHz. R=0.05, RT.

**Table 5.1:** Notch Size and Initiation Location

| Microstructure | Notch Size (2c) $\mu$m | Failure Location |
|---|---|---|
| Disk | 14 | Subsurface |
| Disk | 18 | Subsurface |
| Disk | 20 | Notch |
| Disk | 20 | Notch |
| Disk | 21 | Notch |
| Disk | 22 | Notch |
| Disk | 35 | Notch |
| Disk | 37 | Notch |
| Pancake | 20 | Runout |
| Pancake | 20 | Runout |
| Pancake | 25 | Notch |

Each entry in this table represents 1 specimen which has 10 notches in it.

a slight preference for the $\alpha$ phase material to be favorably oriented for basal slip. The microstructures that were most resistant to fatigue crack initiation from notches had their basal poles oriented parallel to the tensile axis. In cases where this is the predominant intensity peak, cracks did not initiate from these notches. However, even in cases where this is not the dominant texture, crack initiation was still delayed. These results will be presented and discussed in the remainder of Section 5.2.

### 5.2.1 Effect of Frequency on Small Fatigue Crack Growth Rates

Fatigue crack growth data is plotted in Figure 5.7. This plot includes data from both naturally initiated cracks propagated at conventional frequencies [129], shown in open triangles, and FIB-initiated small fatigue cracks grown at ultrasonic frequencies, as shown with closed circles and open squares. As this plot shows, the growth rates are similar at each of the frequencies, that is, they do not exhibit a frequency effect. This is consistent with observations by Boyce et al. [86] in an investigation of frequencies ranging from 50 Hz through 1 kHz in duplex Ti-6Al-4V, and data from others [83, 84, 109] indicates no frequency effect from 20 Hz through 20 kHz.

Analysis of the fatigue crack growth paths observed at both frequencies indicates that the fracture paths between the two materials are essentially the same. Figure 5.4 illustrates the fatigue crack growth path observed in a pancake specimen cycled at conventional frequencies in which the fatigue crack initiated naturally. The crack initiated from the $\alpha$ grain indicated with the arrow. Figure 5.5 illustrates the crack growth path of a fatigue crack that has initiated from a FIB notch and propagated at ultrasonic frequencies. Figure 5.6 is a micrograph of a sample in which a fatigue crack has initiated from a FIB notch in the disk microstructure and has propagated at ultrasonic frequencies. In each of these micrographs, some of the $\alpha_p$ grains appear to deflect advancing fatigue cracks, while in other cases fatigue cracks propagate directly through $\alpha_p$ grains.

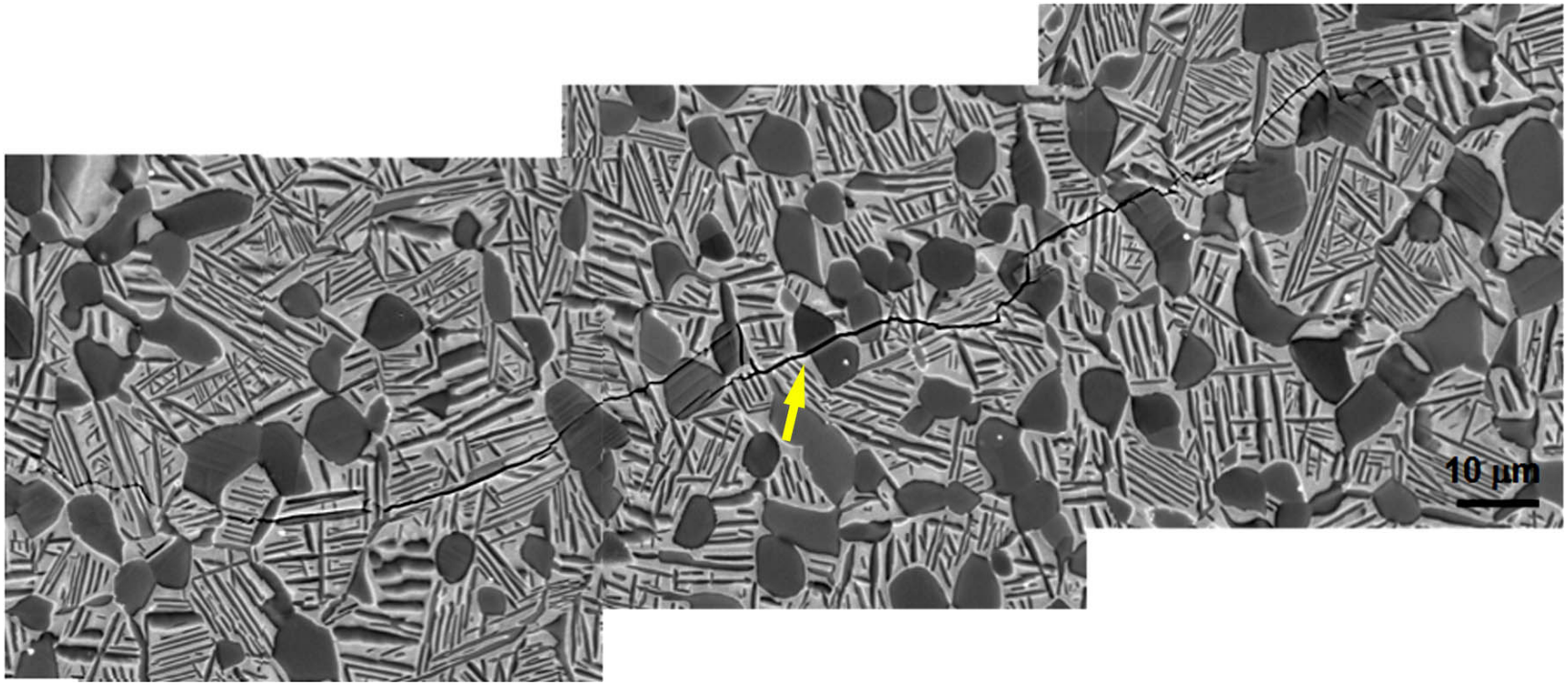


**Figure 5.4:** A SEM surface micrograph of a fatigue crack that was observed to initiate naturally. This specimen was tested at a stress ($\sigma_{max}$) of 860 MPa at a load ratio of 0.05 at 20 Hz. At this point the specimen has experienced 52,000 cycles, and the crack has grown to a length of 168 $\mu$m.

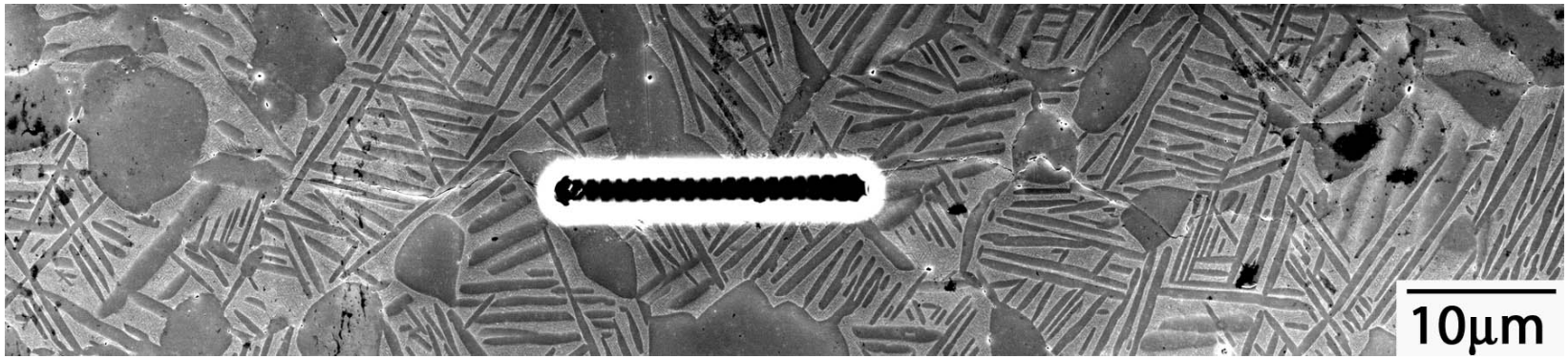


**Figure 5.5:** An SEM micrograph of a fatigue crack that initiated from a FIB notch in the pancake microstructure and propagated at ultrasonic frequencies. This specimen was tested at a stress ($\sigma_{max}$) of 600 MPa at a load ratio of 0.05 at 20 kHz. The tensile axis is vertical.

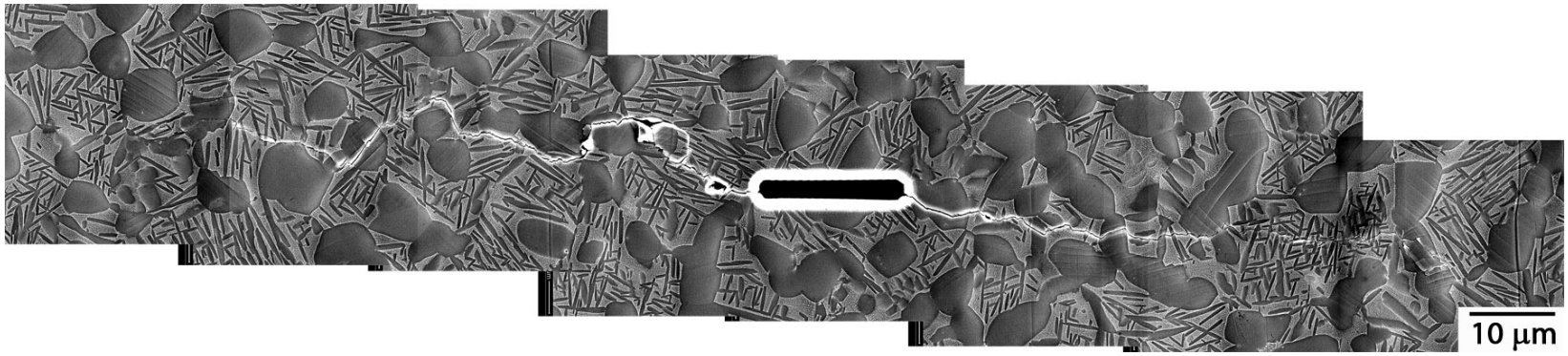


**Figure 5.6:** An SEM surface micrograph of a fatigue crack that initiated from a FIB notch in the disk microstructure and propagated at ultrasonic frequencies. This specimen was tested at a stress ($\sigma_{max}$) of 600 MPa at a load ratio of 0.05 at 20 kHz. The tensile axis is vertical.

### 5.2.2 Variability in Small Fatigue Crack Growth Rates

Figure 5.8 displays the small fatigue crack growth data collected at ultrasonic frequencies. The small crack growth rates converge with the long crack growth rates at a stress intensity of about 5 MPa $m^{1/2}$, which corresponds to a crack size (2c) of approximately 60 $\mu$m at these stress levels. At this size, the crack is approximately 15 times larger than the average $\alpha_p$ grain size, so it seems reasonable that microstructural similitude has been achieved, and it is expected that these growth rates will fall on top of the predicted long crack growth rates. As Figure 5.7 illustrates, small fatigue cracks can propagate well below the long crack growth threshold. Furthermore, variability is observed in the growth rate, and the range of growth rates can be quantified in the near threshold regime by using a power law fit of these portions of the crack growth curves. The constants extracted from a power law fit for the slowest and fastest cracks observed are displayed in Table 5.2.

### 5.2.3 Role of Microstructure in Small Fatigue Crack Growth Rates

The effect of microstructure on small fatigue crack growth rates is addressed in three subsections. The small fatigue crack growth results are divided to analyze the effect of bulk microstructure, the controlling microstructural dimension in fatigue crack initiation, and the effect of local microstructural neighborhoods at notch tips on fatigue crack initiation and early propagation behavior. These sections will focus on the fatigue crack growth behavior at ultrasonic frequencies.

**Table 5.2:** Constants from a Power Law Fit of Small Fatigue Crack Growth Rates

| | **C*** | **m** |
|---|---|---|
| Fastest Crack | 1.34 x $10^{-11}$ | 3.12 |
| Slowest Crack | 1.65 x $10^{-12}$ | 3.50 |

*Units in m/cycle

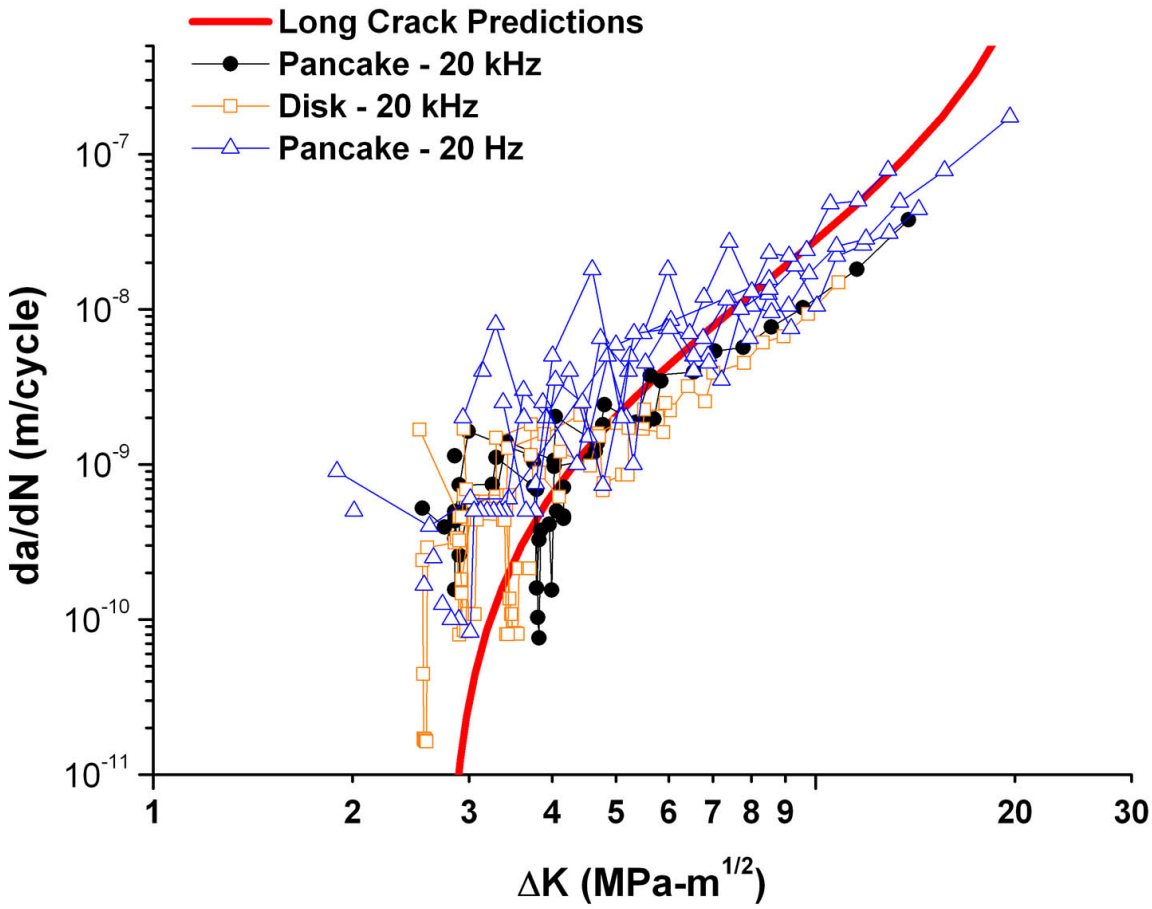


**Figure 5.7:** Small fatigue crack growth data for cracks initiated from FIB-implanted micronotches (20 kHz) and naturally initiated cracks (20 Hz).

#### 5.2.3.1 *Effect of Bulk Microstructural Morphology on Small Crack Growth*

As Figure 5.8 illustrates, there is little difference in the small crack growth rates between the pancake and disk microstructures, despite the higher volume fraction of $\alpha_p$ grains in the disk as compared to the pancake. This fact is also illustrated in the micrographs shown in Figures 5.5-5.6, where the tortuosity of the fracture path is similar. From these micrographs, it would appear that the fatigue crack avoids cutting through the $\alpha_p$ grains, but this is not strictly true. In some cases, the orientation of the active slip systems within the $\alpha_p$ grains with respect to the approaching fatigue crack can be determined by the slip lines within those $\alpha_p$ grains. A few observations can be made about the likelihood of fatigue crack propagation through $\alpha_p$ grains or deflection of the crack around these grains, based on post-mortem analysis of the surface. Slip steps are observed within the majority of $\alpha_p$ grains and these highlight the active slip planes in the advancing plastic zone at the fatigue crack tip.

Generally, the crack path is observed to follow the interface between the lath $\alpha$ and the retained $\beta$ phase. This behavior is accentuated in cases where large $\alpha$ laths are present. Thus, the orientation of the lath and retained $\beta$ phases appears to determine the fatigue crack propagation path. The $\alpha_p$ grains, despite being the minority phase, will also affect the fracture path of these advancing microcracks. The majority of the $\alpha_p$ grains near the fracture path exhibit the formation of slip lines. As the data in Section 4.5.2 show, it is clear that many of the $\alpha_p$ grains do not maintain the Burgers orientation relationship with the transformed $\beta$ phase, which indicates that the crack propagation direction will not be continuous across these phase interfaces. In the relatively rare cases ($< 10\%$) where the $\alpha_p$ grains do not form slip lines observable with SEM examination of the specimen surface, the advancing microcrack is typically deflected by the $\alpha_p$ grain. Within the class of $\alpha_p$ grains that form slip lines, two subdivisions of $\alpha_p$ grains can be constructed. These

subcategories are determined by the orientation of slip lines with respect to the advancing fatigue crack. In some cases, the slip lines within the $\alpha_p$ grains are oriented parallel to the overall fatigue crack growth direction, while in other cases the slip lines are highly misoriented with respect to the advancing microcrack. If the slip lines are misoriented (> 30°) with respect to the overall crack growth direction, the advancing crack is typically deflected by the $\alpha_p$ grain. In the case where slip lines are aligned with the advancing fatigue crack, it is typically observed that the crack will propagate through the $\alpha_p$ grain. However, it should be noted that there are naturally exceptions to all of these observations. These exceptions illustrate some of the difficulties associated with trying to interpret the 3 dimensional nature of fatigue crack growth from 2 dimensional surface observations. With this approach, it is not possible to determine the microstructural configurations present in the specimen interior that are influencing the overall fatigue crack growth rates and fracture path.

#### *5.2.3.2 Effect of Initial Notch Size*

A range of micronotch sizes was used to investigate the competition between microstructure and different notch sizes. As the notch size decreases, microstructural features are expected to control the process of fatigue crack initiation. Notches ranging from 2c ≈ 15-40 $\mu$m were investigated in this study, and Figure 5.9 displays the number fraction of notches that initiated cracks as a function of the initial notch size for both pancake and disk specimens. Each column in this plot represents a specimen with 10 FIB-machined micronotches. In two specimens from the pancake microstructure, fatigue cracks did not initiate from notch sizes (2c) of 20 $\mu$m did not initiate any cracks, which is indicated by the absence of data above these 20 $\mu$m markers. Micronotches on the order of 25 $\mu$m were the smallest notches observed to initiate fatigue cracks in the pancake microstructure. However, notches on the order of 20 $\mu$m commonly cause fatigue failures in the disk material.

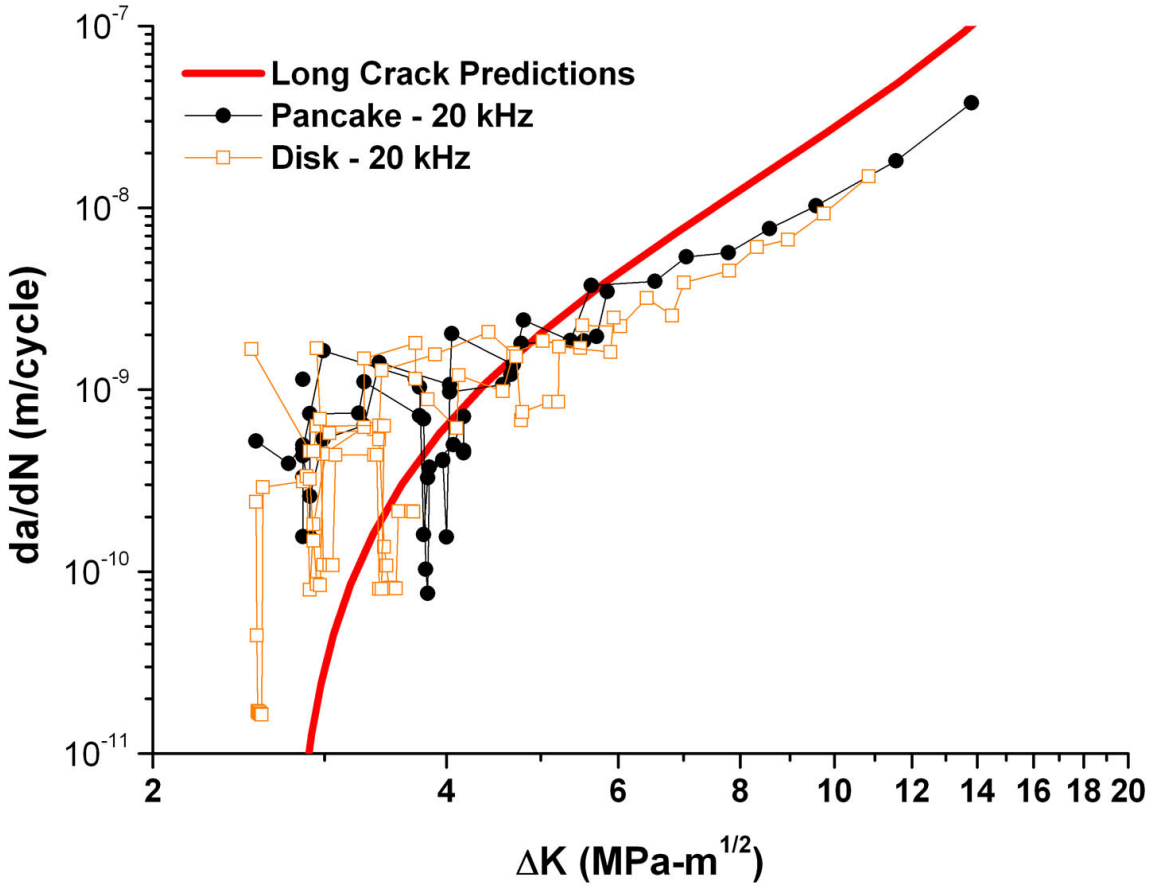


**Figure 5.8:** Growth rates are shown for just the disk and pancake material collected at 20 kHz, room temperature, R=0.05, $\sigma_{max}$=600 MPa, in laboratory air.

These results are summarized in Table 5.1, which indicates some subtle differences exist between microstructures. As a result, most of the fatigue crack growth tests completed in this study have focused on cracks initiating from notches in this size regime to investigate the competition between initiation from microstructural features and initiation from FIB micronotches.

The apparent difference in critical initiation sizes between the pancake and the disk can be rationalized since the disk has a higher volume fraction of $\alpha_p$ grains. As $\alpha_p$ grains are observed to be instrumental in the formation of fatigue cracks, it is intuitive that the greater inherent connectivity of these grains results in a smaller critical defect size controlling fatigue crack initiation.

While crack initiation ocurred for a few notches with a dimension 2c = 14 $\mu$m, these cracks did not propagate beyond one grain diameter. Rather, in this specimen the fatal crack initiated from a microstructural feature in the specimen interior. In fact, one of the specimens, with 14 $\mu$m FIB notches as shown in Figure 5.10, initiated from a subsurface location. Thus, this microstructural region is more susceptible to fatigue damage accumulation than the microstructural neighborhood near the micronotch on the specimen surface. As shown in the fractograph in Figure 5.10b, the major diameter of the facet at the fatigue crack initiation site is approximately 15 $\mu$m, which is equivalent to the micronotch size. Since these length scales are equivalent, it indicates that the differences in damage accumulation between microstructural neighborhoods is significant and has a measureable effect on fatigue lifetimes. This observation indicates that there is a substantial initiation lifetime in this specimen. Additionally, using the measured fatigue crack growth rates at these stresses, a lifetime on the order of $10^6$ cycles is expected if the fatigue crack had initiated in the first cycle. The actual lifetime to failure is 2.94 x $10^8$ cycles, indicating that a substantial portion of the lifetime was consumed with the fatigue crack initiation process.

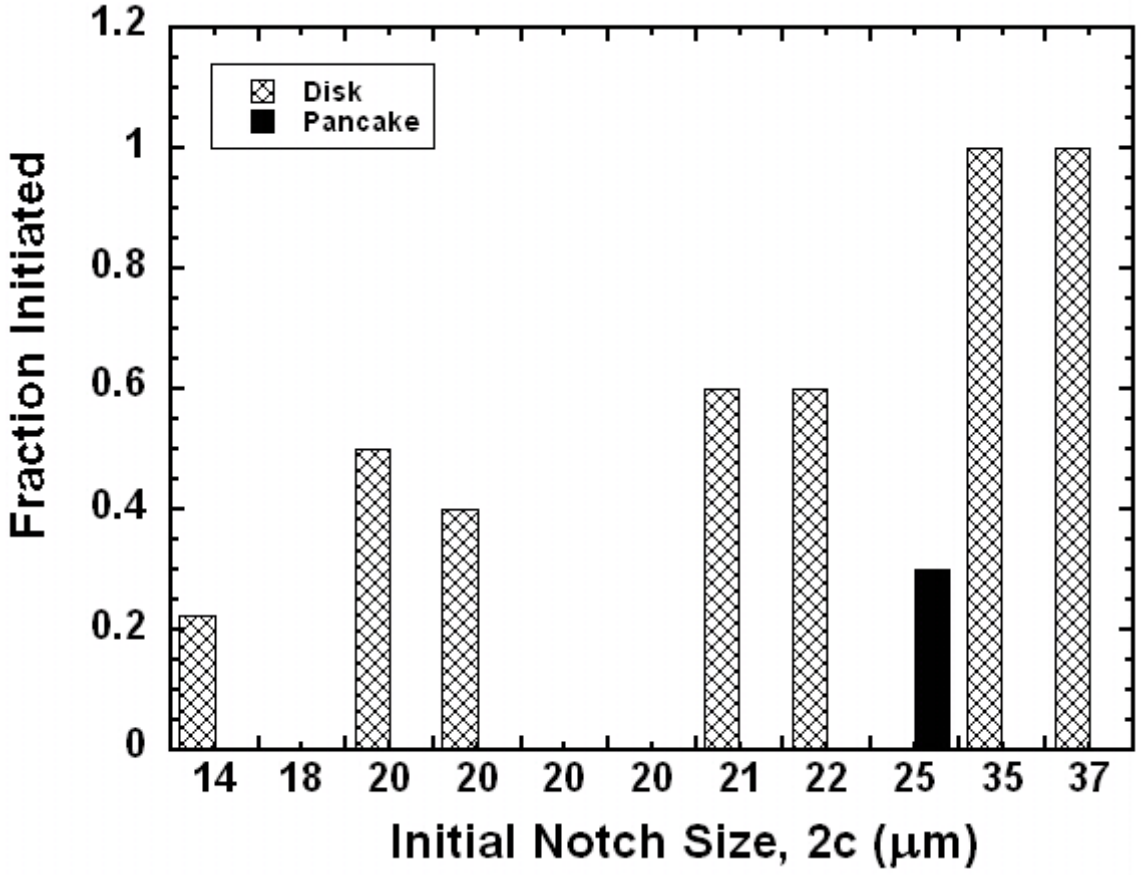


**Figure 5.9:** The fraction of fatigue cracks that have initiated as a function of the initial notch size(2c). All data shown here is for specimens that were tested at 600 MPa, 20 kHz, RT, R=0.05.

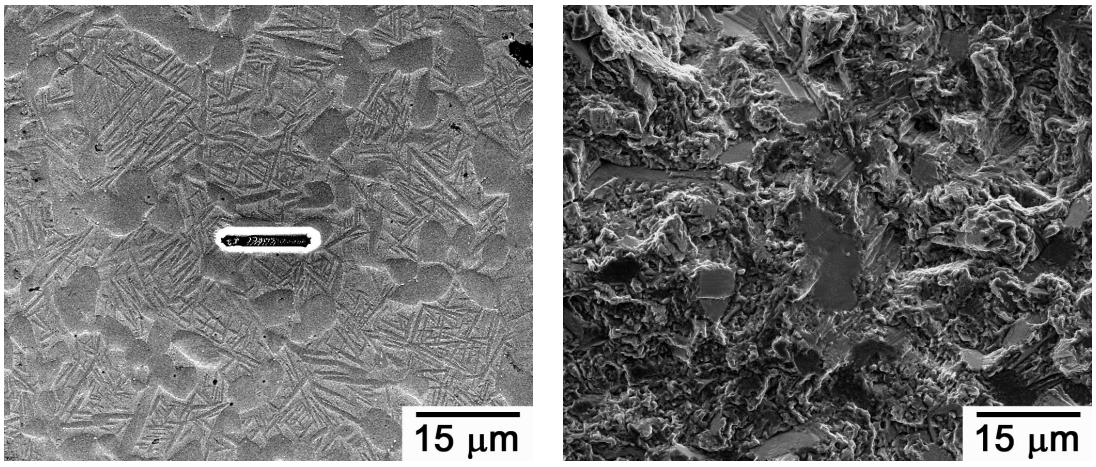


**(a)** **(b)**

**Figure 5.10:** A specimen with FIB-implanted micronotches that failed from subsurface fatigue crack initiation: (a.) A micrograph of the of the micronotch (2c=14$\mu$m), (b.) a fractograph of the subsurface fatigue crack initiation site illustrating the presence of a 15 $\mu$m facet at the crack initiation site. $\sigma_{max}$=600 MPa, R=0.05, 20 kHz, room temperature, $N_f$=2.94 x $10^8$ cycles.

#### *5.2.3.3 Effect of Local Microstructural Neighborhoods*

Since 10 notches were machined in each specimen, a direct comparison of microstructures was possible. Microstructural regions were compared in terms of both ease of initiation and ease of fatigue crack growth.

The use of multiple notches in any given specimen allowed for the direct comparison of growth rates with microstructural neighborhoods. Assuming that a crack propagates as a semi-circle, the crack front is interacting with much more of the microstructure than is observable at the specimen surface. Thus, while the grains just at the tip of the crack on the specimen surface may be unfavorably oriented for slip, the grains at the crack tip in the specimen interior may be favorably oriented for slip and enable this crack to continue propagating. In this study, comparisons of the microstructural regions around the micronotches are limited to discussions of local texture of the $\alpha$ phase and the parent $\beta$ grains, since the notch size falls well within the dimensions of the microtextured regions, allowing for a

measureable effect of texture to be observed.

For each specimen, the first notch to initiate a fatigue crack was identified from the replicas. This is shown in Figure 5.11, which is a plot of a vs. N for all the cracks in one specimen. These cracks all appear to propagate at similar rates, and differences in crack sizes can be related to the lifetime at which they initiated, i.e. there are no crossovers in the crack sizes once the crack has initiated. These data differ from the observations of Sinha et al. [62] in Ti-6242, where they observed that the cracks that led to final fracture were not necessarily the first to initiate, but they did initiate from the largest microtextured regions. This observation is more surprising since Sinha and co-workers were working at approximately 90-95% of the yield strength of this alloy, and for crack sizes would continue to propagate once they have initiated.

The local textures, as measured from a 100 x 150 $\mu$m area near the notches that were the first to initiate, are shown in Figure 5.12, and the inverse pole figures are displayed with a reference frame such that [0001] is parallel to the tensile axis. Each part of this Figure displays the texture measured in different specimens, and only specimens with a microstructurally sensitive notch size (2c $\approx$ 20-25 $\mu$m) are shown. Near each of these notches, there is a slight preferred texture where the material is favorably oriented for basal slip. For every specimen that was tested, 9 notches were identified as propagating slowly or not initiating. A representative sampling of the notches that exhibited delayed initiation is shown in Figure 5.13, and these notches are shown for the same 4 specimens that are displayed in Figure 5.12. The texture in these microstructural regions is still favorable for fatigue crack initiation. However, the damage accumulation process near these notches is sluggish, compared to the regions characterized in Figure 5.12. The intensity of the texture, indicated by the scale in the pole figures, near these 4 notches is generally not as strong as that observed near the early-initiating notches. Figure 5.14 displays the texture surrounding notches that did not initiate fatigue cracks. All of these pole figures exhibit a preferred

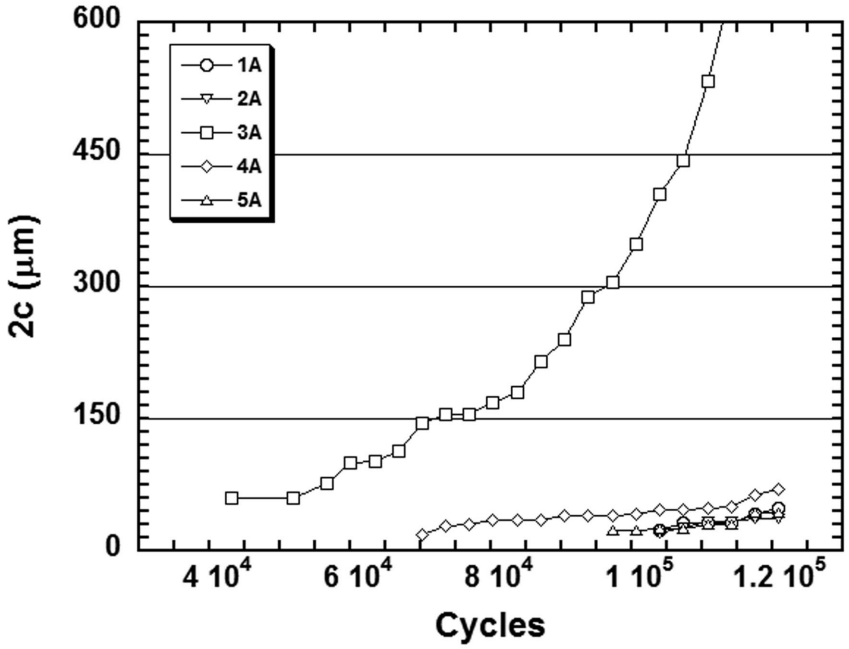


**Figure 5.11:** A typical a vs. N plot, which shows that the first crack to initiate is also the crack that grows to the largest size, i.e. no significant crack arrest was observed.

texture where the basal pole is parallel to the loading direction. Another observation of these textures is that the intensity of the texture continually decreases from the fatigue crack initiating notches to notches with delayed initiation and ultimately to non-initiating notches. These results indicate that the ability of the microstructure to accomodate basal slip is an important factor in fatigue crack growth. If the local texture is not favorable for the activation of basal slip, then fatigue crack initiation and growth is likely to be delayed or prevented.

### 5.2.4 Summary of Small Fatigue Crack Growth in Ti-6246

Fatigue cracks have been initiated from FIB-implanted micronotches and fatigue crack growth rates have been measured at 20 kHz. The growth rates of these fatigue cracks do not exhibit any frequency dependence between 20 Hz and 20 kHz. For the pancake microstructure, notches with a surface length (2c) of 20 $\mu$m or less were never observed

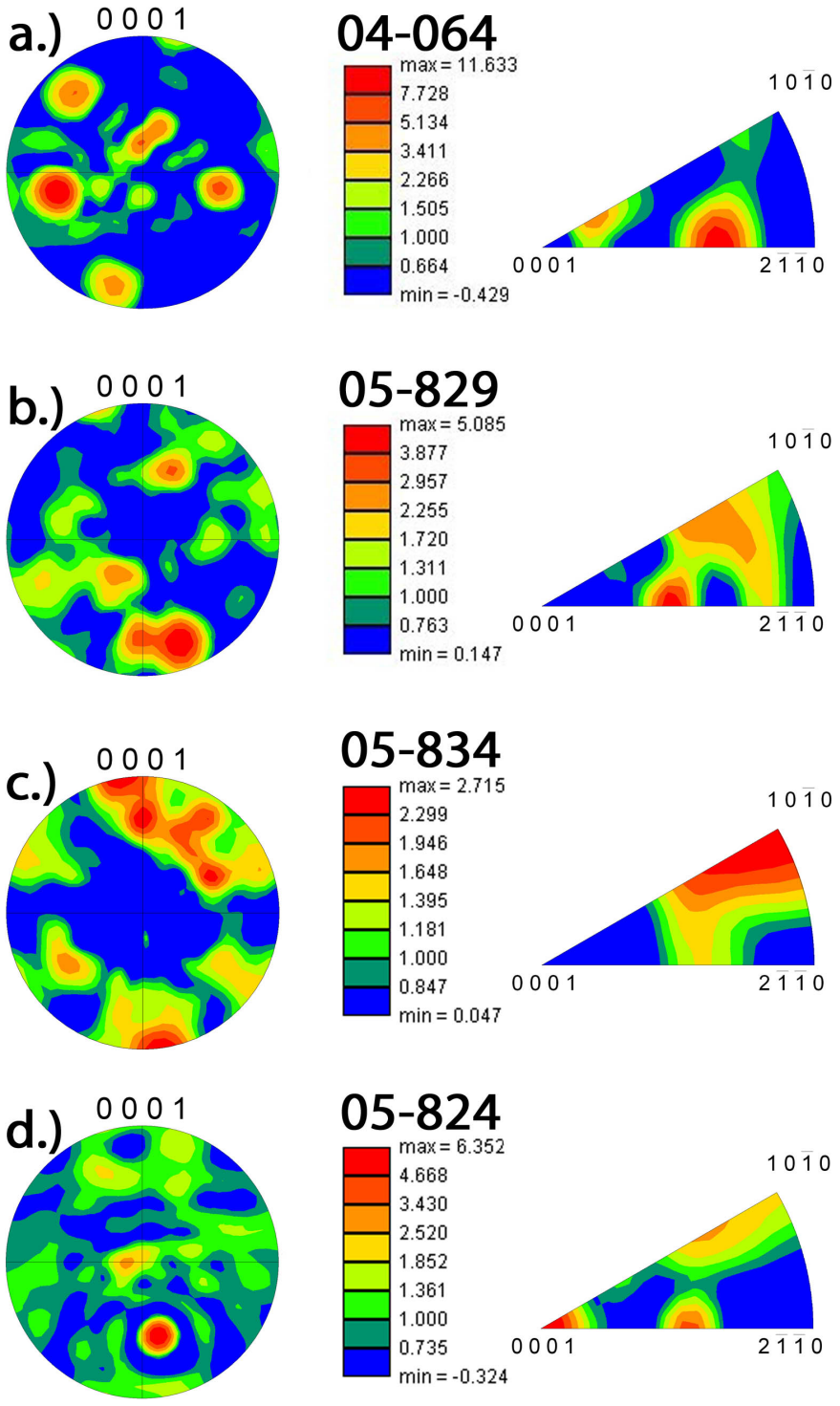


**Figure 5.12:** The local texture as measured from the area near the FIB-implanted notches for notches that were observed to initiate first within a given specimen. The textures were measured from a number of different samples: a.) pancake specimen, 2c=25 $\mu$m, b.) disk specimen, 2c=22 $\mu$m, c.) disk specimen, 2c=20 $\mu$m, d.) disk specimen, 2c=21 $\mu$m.

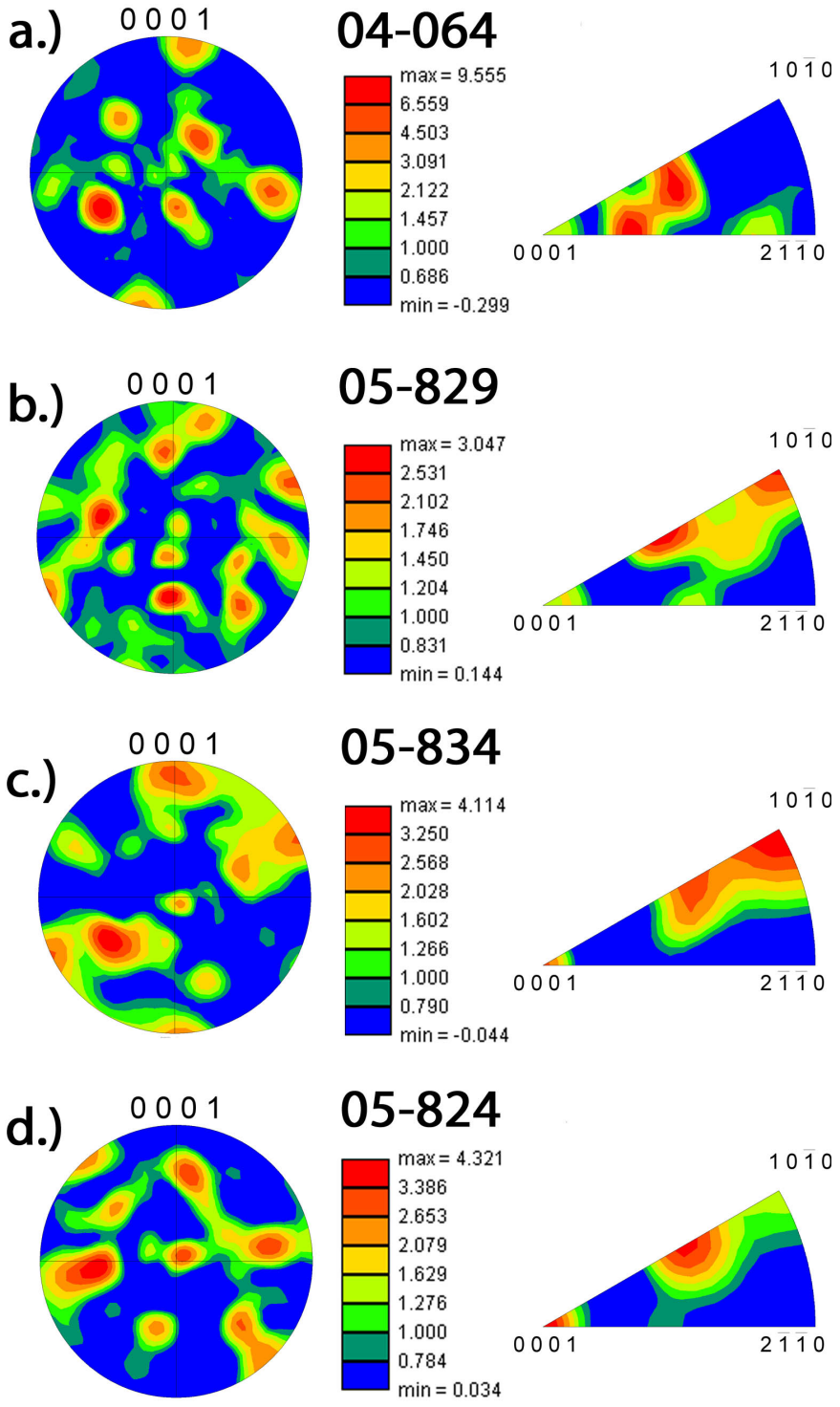


**Figure 5.13:** The local texture as measured from the area near the FIB-implanted notches for notches with delayed initiation within a given specimen. The textures were measured from a number of different samples: a.) pancake specimen, 2c=25 $\mu$m, b.) disk specimen, 2c=22 $\mu$m, c.) disk specimen, 2c=20 $\mu$m, d.) disk specimen, 2c=21 $\mu$m.

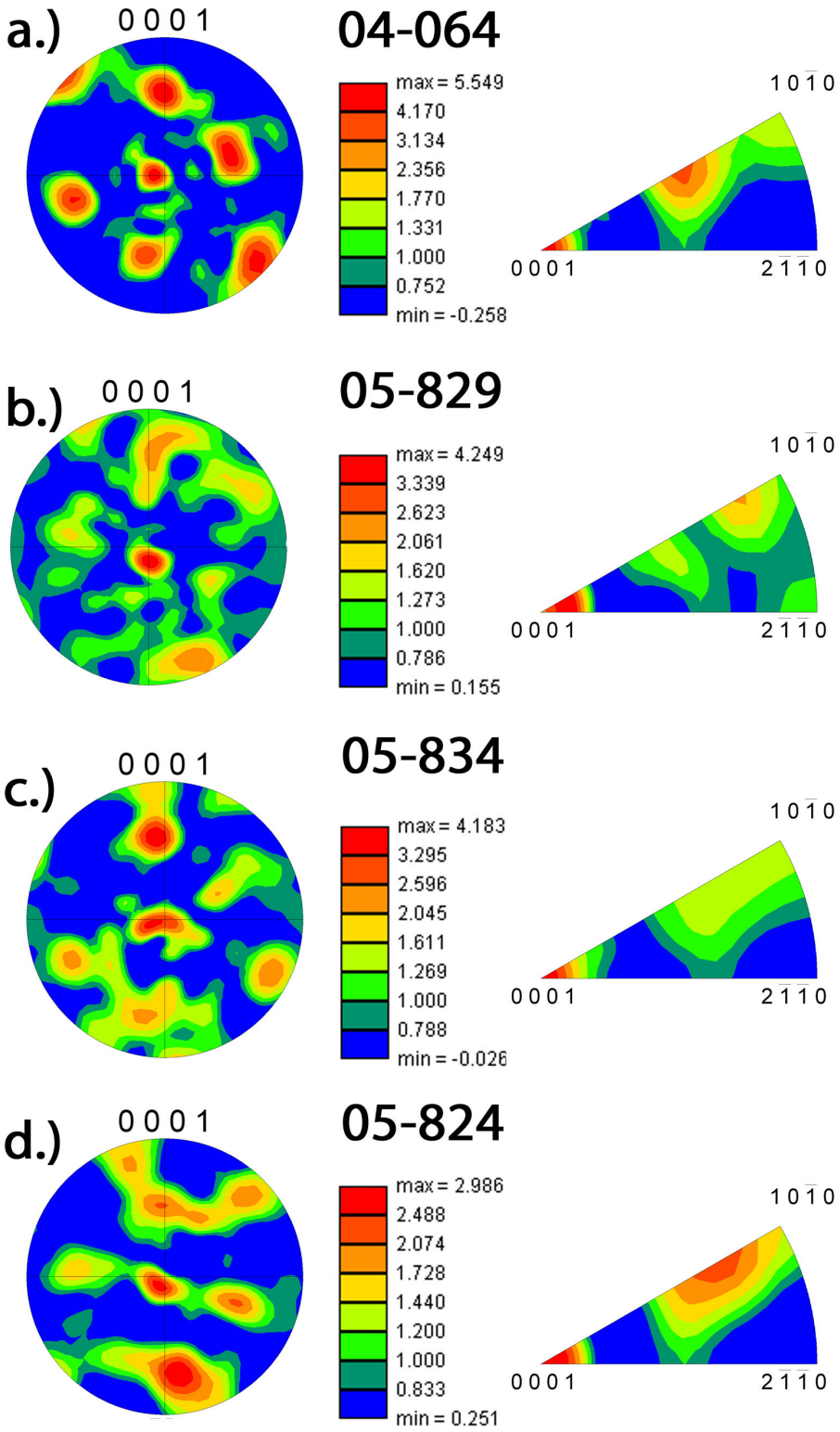


**Figure 5.14:** The local texture as measured from the area near the FIB-implanted notches that did not initiate fatigue cracks. The textures were measured from a number of different samples: a.) pancake specimen, 2c=25 $\mu$m, b.) disk specimen, 2c=22 $\mu$m, c.) disk specimen, 2c=20 $\mu$m, d.) disk specimen, 2c=21 $\mu$m.

to initiate the fatal fatigue crack. In the disk, with notch sizes larger than 20 $\mu$m, notches always initiated fatigue cracks, and these were the dominant cracks leading to specimen failure. Thus, a range of 20-25 $\mu$m has been identified as the controlling microstructural dimension in the process of fatigue crack initiation, which agrees well with the size of the initiation region observed in SN-type tests.

Analysis of the specimen surface indicates that the advancing fatigue cracks sometimes are deflected at $\alpha_p$ grain boundaries, while in other cases, they appear to propagate through these grains. If slip lines are not observable in the $\alpha_p$ grain with SEM analysis of the specimen surface, then the crack will likely be deflected by this grain. In the case where slip lines do develop, the crack propagates through the $\alpha_p$ grain if the slip lines are not significantly misoriented with respect to the overall fatigue crack growth direction. For the case of $\alpha_p$ grains that form slip lines misoriented by more than about 30° with respect to the crack growth direction, the $\alpha_p$ grain would be expected to deflect the approaching microcrack.

The texture observed in these regions adjacent to the micronotches influences the fatigue crack initiation, with regions favorably oriented for basal slip promoting early fatigue crack formation. Conversely, when a preferred texture of grains are oriented with their basal plane normals parallel to the tensile axis, crack initiation from micronotches is suppressed. This suggests that in the absence of material favorably oriented for basal slip, it may be more difficult for fatigue cracks to initiate from micronotches and grow. Thus, the fact that material favorably oriented for basal slip is associated with the earliest cracks to initiate and the absence of these textures is observed in notches that fail to initiate cracks both point to the fact that basal slip is an important deformation mode in this alloy and under these loading conditions.

## *5.3 Lifetime Predictions*

The small fatigue crack growth rates measured from FIB-implanted micronotches were fit to the power law equation, as described in Section 3.3.3. The constants, C and m, were used in Equation 3.7 to predict the small fatigue crack growth portion of the fatigue lifetimes by fitting the small crack growth rates up until the stress intensity at the crack tip was approximately 5 MPa $m^{1/2}$. Beyond this point, cracks were observed to propagate according to the long fatigue crack growth rates with insignificant variability. The portion of lifetime attributed to long fatigue crack growth was predicted using constants measured from fitting data in the regime of > 5 MPa $m^{1/2}$. The constants, c and m, representing the bounds of long fatigue crack growth behavior have been extracted from the long crack growth data and are displayed in Table 5.3. Using this approach, the worst lifetime predicted was achieved by the combination of using the largest predicted initiation size, the fastest small crack growth rate, and the fastest long crack growth rate. Conversely, the longest fatigue lifetime was predicted by using the smallest starting crack size and the slowest fatigue crack propagation rates measured for both small and long fatigue cracks. The range in lifetimes predicted from this approach is illustrated by the curves overlaid on the SN-plot in Figure 5.15. This approach to predicting lifetimes does accurately predict the minimum observed lifetimes. As expected, this plot illustrates that the range of fatigue lifetimes predicted from the observed variability in fatigue crack growth rates does not account for the amount of scatter observed in fatigue lifetimes in the regime of VHCF. This finding indicates that scatter in the regime of VHCF is primarily attributable to the variability in the process of fatigue crack initiation.

**Table 5.3:** Constants from a Power Law Fit of Measured Long Fatigue Crack Growth Rates

| | C* | m |
|---|---|---|
| Fastest Crack | 3.4 x $10^{-12}$ | 3.68 |
| Slowest Crack | 2.44 x $10^{-11}$ | 2.60 |

* Units in m/cycle

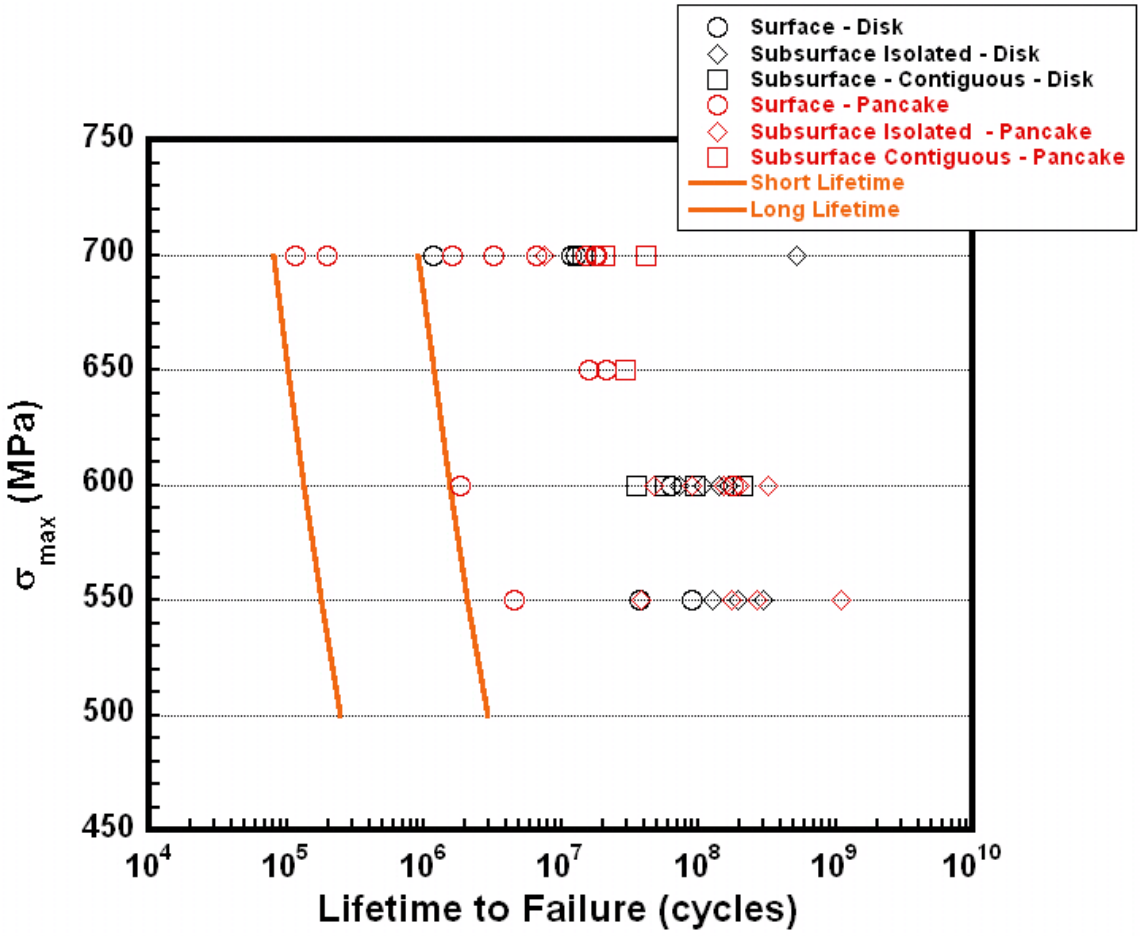


**Figure 5.15:** The predicted scatter in fatigue lifetimes is displayed on an SN plot resulting from the range of fatigue crack growth rates observed in ultrasonic frequency fatigue crack growth experiments.

## *5.4 Summary and Conclusions*

This chapter presented results from fatigue crack growth experiments designed to identify the effect of microstructure on fatigue crack growth behavior in these alloys. The fatigue crack growth rates measured using ultrasonic fatigue techniques are not observed to exhibit any frequency effect with respect to the fatigue crack growth rates measured at conventional frequencies of 20 Hz. Also, there is very little variability in long fatigue crack growth rates, but substantially more scatter in short fatigue crack growth rates. There is no difference in the initial short fatigue crack growth rates measured from naturally initiated fatigue cracks and those growth rates measured from FIB-implanted micronotches. Micronotches with a surface length (2c) of approximately20-25 $\mu$m exhibited a sensitivity to local microstructure at the notch tips. For all notches of this size, approximately 1/2 of them were observed to initiate fatigue cracks. For larger, 35 $\mu$m, notches these features were always observed to initiate fatigue cracks. In the case of small notches on the order of 15 $\mu$m, other microstructural neighborhoods are observed to initiate fatigue cracks.

It was shown that the effect of texture is more substantial in terms of inhibiting fatigue crack initiation from micronotches than encouraging microcrack initiation. In cracks that were the first to initiate, there is no common texture observed across all initiation sites. However, a sampling of the notches that did not initiate displayed a trend where the texture was oriented such that the basal planes are oriented normal to the overall fatigue crack growth direction. The observed fatigue crack growth rates have been modelled with a power law fit. The constants from this fit (c + m) have been used to make predictions of the worst case fatigue lifetime observed in $\alpha + \beta$ processed Ti-6246 under ultrasonic fatigue loading conditions.

# Chapter 6

# Discussion

The experimental characterization results presented in Chapters 4 and 5 identify fatigue critical microstructural neighborhoods that are more susceptible to fatigue crack initiation and propagation than nominal microstructures. The goal of this chapter is to provide context for the interpretation of these results. Furthemore, the objective of this chapter is to elucidate the significance of some experimental results that address topics which are open questions in the literature.

## *6.1 Surface vs. Subsurface Fatigue Crack Initiation*

Cracks have been observed to initiate at both surface and subsurface locations and this is often related to loading conditions and testing environment [44,52,95,99]. At high stresses, fatigue crack initiation at slip bands is the preferred initiation location and slip bands are typically observed at the surface. However, at lower stresses, the mechanism of fatigue crack intiation has been observed to shift to the specimen interior. In the regime of VHCF, researchers have noted the increased likelihood of subsurface fatigue crack initiation in fatigue specimens. This has been attributed to a number of different factors, such as the presence of compressive surface residual stresses, the likelihood of finding a crack initiating defect in the specimen interior compared with the specimen surface, and the effect of environment. Current thinking and approaches in fatigue work indicate that the presence of microstructural regions capable of initiating fatigue damage determines where the fatigue

crack will initiate.

Interpretation of the transition from surface to subsurface fatigue crack initiation may be analogous to the transition in crack initiation mechanisms as the applied stress is decreased. As mentioned in Section 2.2.1.2, cracks are observed to initiate from within a given microstructural component (grain, colony) at high stresses, while at lower stress levels, initiation is typically observed at grain or phase boundaries and attributed to strain incompatibility between these two grains or colonies. As suggested in the literature review, it seems likely that higher stresses lead to the development of slip activity within individual grains. By extension, if it is easier to initiate slip activity within individual grains at higher stresses, this should be true for both potential crack initiation sites in both surface and subsurface locations. However, fatigue critical neighborhoods located at the specimen surface may be more susceptible to fatigue damage accumulation in the form of slip bands since the surface grains are less constrained. In the specimen interior, the grains will be constrained from forming slip bands, and as a result, strain incompatibility at grain boundaries and phase interfaces will be the operative mechanism of fatigue crack initiation. As Section 4.5.2 discussed, since the majority of $\alpha_p$ grains do not maintain the Burgers orientation relationship, the implication is that strain incompatibility at $\alpha_p$ grain and phase boundaries will be the mechanism of fatigue damage accumulation. This mechanism of strain incompatibility may also be operative in surface initiated fatigue cracks, however if there is a surface-connected region where damage may accumulate by a mechanism of slip band formation, this mechanism of damage accumulation will preempt the strain incompatibility mechanism. In some cases, it is observed that surface initiated failures exhibit similar lifetimes to subsurface initiated failures. This observation may be due to the fact that the surface initiated fatigue cracks initiated by a mechanism of strain incompatibility, rather than by a mechanism of slip band formation.

To summarize, the earliest cracks to initiate will form by a mechanism of slip band

formation in surface grains. Longer lifetimes will be exhibited by specimens that initiate fatigue cracks at interfaces where the accumulation of strain incompatibility is operative. This mechanism of strain incompatibility can operate in the specimen interior and at the specimen surface, however this mechanism will only be responsible for fatigue damage accumulation if there are no surface regions capable of forming slip bands.

## *6.2 Proposed Model of Fatigue Crack Initiation*

As discussed in Section 2.2.1, fatigue crack initiation is often attributed to the presence of microstructural features that promote the localization of cyclic damage. All of the analyses discussed thus far have indicated that the features observed at the fatigue crack initiation site are also commonly observed in the nominal microstructure. These include $\alpha_p$ grain size, $\alpha_p$ grain clustering, crystallographic orientation, and the presence of microtextured regions. It appears that all of these features are common in nominal microstructural sections and thus, the limiting criteria for fatigue crack initiation is the presence of microtextured regions with grains favorably oriented for basal slip. Since this is believed to drive the fatigue behavior of this alloy in the VHCF regime, it is important to develop a quantitative description of probability of occurence of these microtextured regions to determine the number density of these fatigue critical microstructural regions in a given sample volume.

Figures 4.25, 6.1, and 6.2 illustrate that regions of microtexture are commonly found in nominal sections of the microstructure. None of the microtextured regions observed in the random sections exhibit the same intensity of texture observed at the fatigue crack initiation site, as shown in Figure 4.23. It is implausible to say that such a large region of microtexture is required to form a fatigue crack. More likely, the size of the microtextured region simply increases the potential number of sites from which a fatigue crack may initiate. As the fatigue crack growth studies illustrated, notches on the size of 20 $\mu$m are capable of overcoming nominal microstructures in the process of fatigue crack initiation. To quantify

the number of potential initiation sites within a given sample, it will be necessary to make a few assumptions. To err on the side of safety, it will be assumed that an aggregate of lath and equiaxed $\alpha_p$ grains on the order of 50 $\mu$m must be present in order for a fatigue crack to initiate. This is 2.5 times larger than the size observed to be important in the fatigue crack growth studies. Additionally, to convert the scans from a measure of area to a volumetric measurement, it will be assumed that these scans actually characterize a thickness of 10 $\mu$m both above and below the section plane. In other words, if there is a fatigue critical neighborhood with its center displaced 10 $\mu$m above or below these section planes, it is expected that these features would be identifiable in these IPF maps.

Upon examination of these figures, it is clear that fatigue critical regions on the order of 50 $\mu$m can be found in both OIM scans and these regions are indicated with arrows. The total area of material characterized between these three regions is 4.8 mm$^2$. Assuming that the thickness of material that has been characterized is approximately 20 $\mu$m, the total volume of material characterized would then be 0.096 mm$^3$. In Figure 4.25, two potential initiation sites can be identified and within the other two scans, three additional potential fatigue crack initiation sites can been identified and these are indicated with arrows. Therefore, a total of five occurences have been identified in a sample volume of approximately 0.1 mm$^3$. Thus, if this occurence rate is scaled up to the size of the specimen gage volume of 48 mm$^3$ (12 mm in length with a 4 mm diameter), it is predicted that there would be on the order of 2,400 potential fatigue crack initiation locations. With this many potential initiation sites, it would appear that fatigue crack initiation is nearly certain for any given specimen. However, some specimens are observed to runout to $10^9$ cycles without failure. This observation would seem to indicate that the fatigue process is highly stochastic and that despite the presence of fatigue critical microstructural neighborhoods, crack initiation is by no means assured.

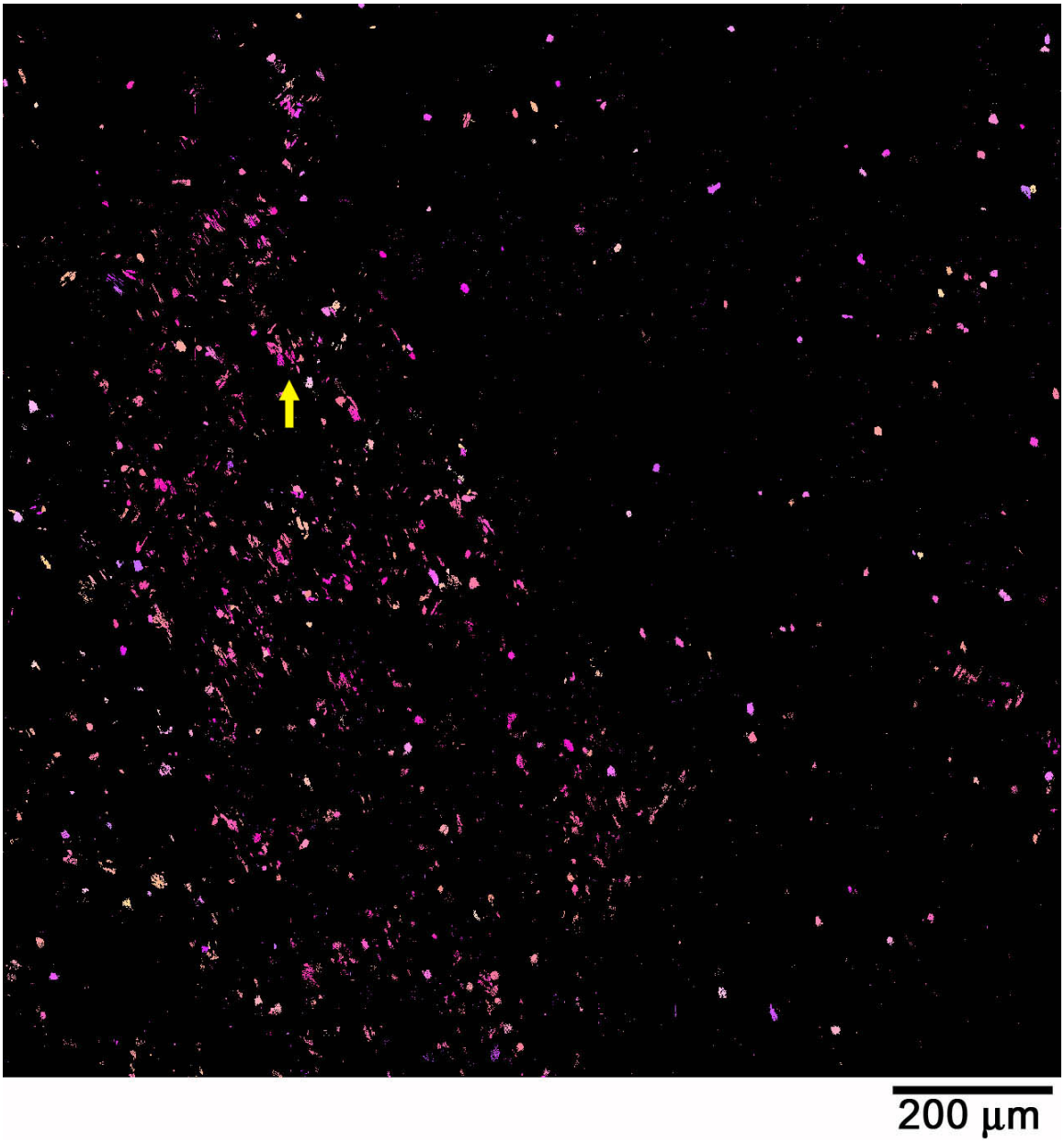


**Figure 6.1:** An example OIM IPF map where just the material that is favorably oriented for basal slip has been selected to illustrate the heterogeneous distribution of these regions within the microstructure and the number of potential factigue crack initiation sites within these regions. The total area of this scan is 1.8 $mm^2$.

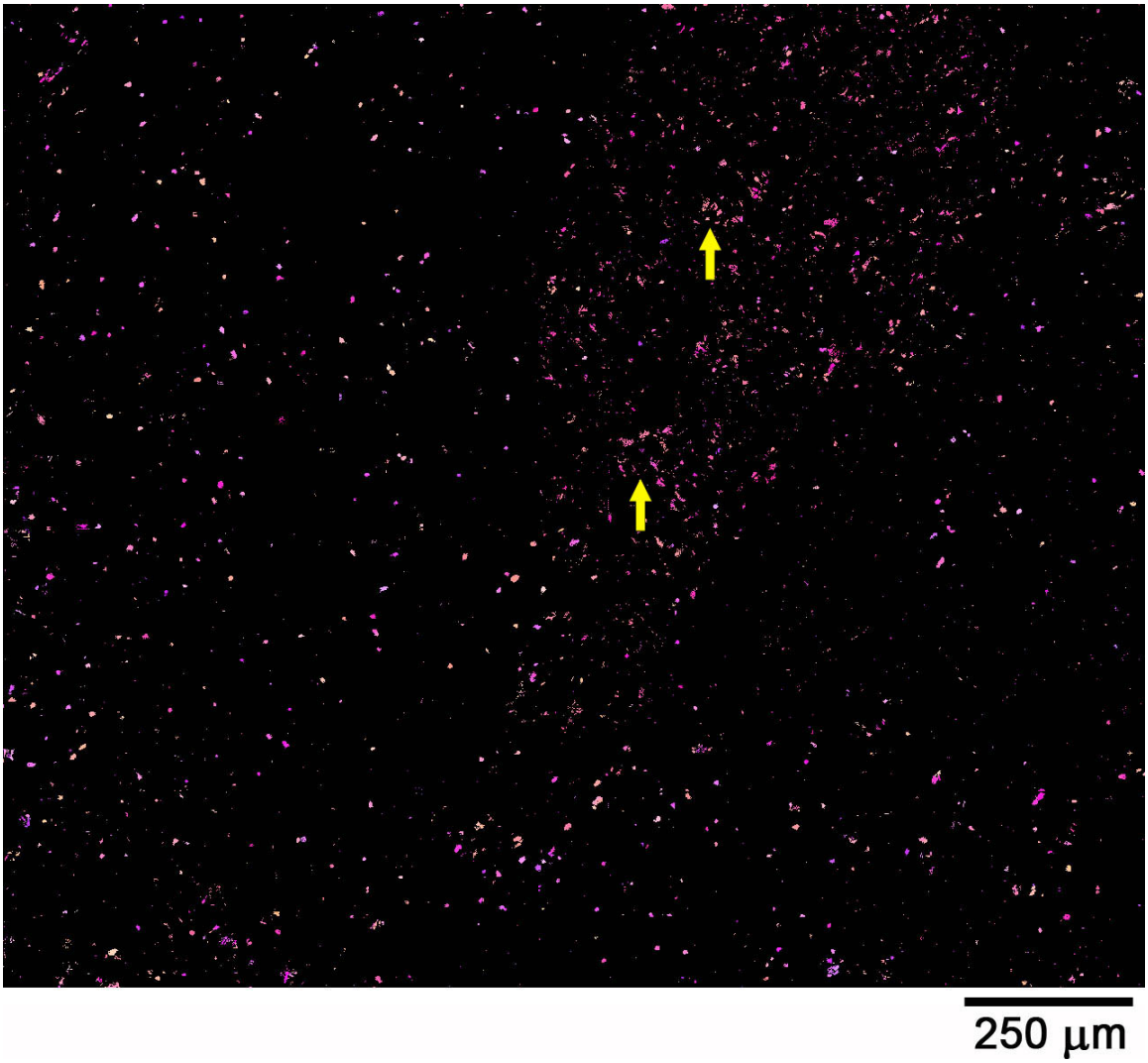


**Figure 6.2:** An example OIM IPF map similar to that shown in Figure 6.1. The total area of this scan is 2.5 $mm^2$.

# Chapter 7

# Conclusions and Future Work

## *7.1 Summary and Conclusions*

### 7.1.1 Fatigue Behavior and Fractographic Analysis

Ultrasonic frequency fatigue has been completed at 0.4-0.6 $\sigma_{YS}$ on Ti-6246, and lifetimes in the range of $10^6 - 10^9$ have been observed. Two different microstructural conditions have been investigated, and similar average fatigue lifetimes are observed for both batches of material. Three characteristic crack initiation sites have been identified, and they can be ranked in order of severity based on the average observed lifetime to failure. Surface initiated cracks exhibit the shortest lifetimes, while subsurface cracks with isolated faceting display longer lifetimes, and subsurface initiation from contiguous facets offer the highest fatigue crack initiation resistance. Aside from this general trend, there is scatter of approximately 2-3 orders of magnitude associated with each of the characteristic fatigue crack initiation sites, and it is not possible to directly relate the observed lifetimes to distance of the crack initiation site from the specimen surface. The implication of this is that scatter in fatigue lifetimes cannot be accounted for as an environmental effect on the fatigue crack growth process, but rather that this scatter results from variability in the fatigue crack initiation process.

Crack initiation is associated with facet formation in $\alpha_p$ grains. Furthermore, the $\alpha_p$ grains that form facets do not fall into the tails of the $\alpha_p$ grain size distribution, i.e. they are common within the microstructure. In other words, they are commonly found throughout

the sample gage volume. The facets do not exhibit any specific spatial distribution. That is, the spatial distribution of facets is similar to the distribution of $\alpha$ grains in the nominal microstructure. Thus, the critical microstructural features responsible for fatigue crack initiation cannot be identified based on $\alpha_p$ grain size or spatial distribution. Using stereology, the orientation of these $\alpha_p$ facets indicates that they form due to a slip-type process, i.e. facet poles are commonly oriented 30-60° away from with respect to the tensile axis.

### 7.1.2 Crystallographic Orientation and Texture Analysis

The facet plane of the $\alpha_p$ facets was determined to be the basal plane of the hcp lattice from the combination of OIM and stereological measurements. As the stereological measurements indicated, these facets are oriented for a high resolved shear stress indicating that basal slip is the operative deformation mechanism. In surface initiated failures, 1-2 large grains are observed to be oriented for basal slip. In subsurface initiated failures with isolated facetting, the microstructural regions near the site of fatigue crack initiation are observed to have a strong preferential orientation for basal and prism slip. In subsurface initiated failures with contiguous facetting, the texture does not appear to be very strong. These results are summarized in Table 4.6. The presence of these regions of material that are favorably oriented for basal slip are derived from the parent $\beta$ grain orientation through the Burgers orientation relationship. These so-called microtextured regions are commonly observed in the general microstructure as well. Observations of nominal microstructural regions with OIM techniques indicate that these fatigue critical regions are commonly observed in the average specimen gage section. This suggests that many of these fatigue critical regions remain inactive in each specimen. Thus, as the presence of microtexturing is not a distinctive characteristic of the fatigue crack initiation sites, it appears that subtler aspects of these textured regions must exist that enhance the susceptibility of these regions to cyclic damage accumulation and fatigue crack formation.

Additional measurements of the fatigue crack initiation sites have been made to quantify the microstructural configurations at those sites. These measurements were taken to determine the effect of $\alpha_p$ vs. lath $\alpha$ on the resulting fatigue lifetimes. In both cases, only the $\alpha$ phase material oriented for basal slip was considered. The results indicate that for a given volume fraction of material favorably oriented for basal slip, longer fatigue lifetimes are observed in specimens that have a lower percentage of the material oriented for basal slip concentrated in the $\alpha_p$ grains. This suggests that if the material oriented for slip exists in the phase with a finer scale, it will take longer for fatigue damage to accumulate and form a fatigue crack. In other words, fatigue resistance is improved as the microstructural phases are refined. This observation appears to agree with the findings of other researchers [51, 54], since it would suggest that larger $\alpha_p$ grains are more susceptible to fatigue damage accumulation and crack formation due to their longer slip length.

The orientation of these $\alpha_p$ grains near the fatigue crack initiation sites has been measured to determine if their crystallographic orientation can be predicted by one of the Burgers orientation variants of the parent $\beta$ grain orientations. In general, the $\alpha_p$ grains that form facets are not observed to maintain an orientation that is predicted by the Burgers orientation relationship, which indicates that slip transfer between the $\alpha_p$ grains and the $\alpha$ laths is not an operative fatigue crack initiation mechanism. The measurements of $\alpha_p$ grain misorientations with respect to the parent $\beta$ grain orientations from initiation sites are similar to the misorientation measurements of $\alpha_p$ grains within random microstructural sections. Based on these measurements and the observed texture, a mechanism of fatigue crack initiation has been proposed, which is hypothesized to operate by a mechanism of strain incompatibility.

### 7.1.3 Fatigue crack growth

Fatigue crack growth rates have been characterized for both small and long fatigue cracks. No effect of frequency was observed between the two frequencies investigated: 20 Hz and 20 kHz. Also, bulk microstructure (disk vs. pancake) was not observed to affect the growth rates in these experiments. The fatigue crack growth path was affected by the presence of $\alpha_p$ grains. If $\alpha_p$ grains did not form slip lines, the advancing fatigue crack was typically deflected by these grains. Furthermore, if the slip lines formed a large angle with the direction of microcrack advance, the $\alpha_p$ grains also tended to deflect the fatigue crack. Only when the slip lines in $\alpha_p$ grains were aligned with the approaching crack was the crack observed to propagate through these grains.

Notches ranging in size from (2c) 15-40 $\mu$m have been machined in fatigue samples, with a critical notch size on the order of (2c) 20 $\mu$m being observed to initiate fatigue cracks. For the case of micronotches smaller than these dimensions, cracks were observed to initiate from microstructural features elsewhere within the gage volume. Small fatigue cracks did exhibit variability in their growth rates. The first cracks to initiate always led to specimen failure. These life-controlling notches are associated with microstructural neighborhoods that are more susceptible to accelerated fatigue damage accumulation, as indicated by the texture observed for basal slip. In the case of notches that did not initiate fatigue cracks, it was observed that the texture was oriented such that the basal poles of many grains were parallel to the tensile axis. The difficulty of deformation on the basal planes with these orientations is believed to explain the generally improved fatigue resisatnce in these microstructural regions.

Using the constants, C and m, as measured by a power law fit of the fatigue crack growth data, it was possible to predict the worst case fatigue lifetime observed in SN-type tests.

## *7.2 Recommendations for Future Work*

Based on the findings presented in this thesis, the following recommendations are made for future research in this area.

(1) One of the central ideas in current fatigue variability work is that multiple mechanisms of fatigue failure may be operative at any given stress level. For each of these mechanisms, there is not a deterministic lifetime, but rather a distribution of lifetimes is possible. Thus, to fully explain fatigue variability as a function of microstructural heterogeneity, the statistical distribution of lifetimes as a function of initiation mechanism must be characterized. This approach requires that a substantial number of tests be run to sample each mechanism and fully describe the distribution of lifetimes attributed to each mechanism. Therefore many repeat fatigue tests should be completed at the same stress level to ensure that the full range of initiation mechanisms are represented. As these distributions are more fully characterized, the severity of different microstructural regions and the associated microstructural neighborhoods will be identified. As more testing is completed, a probabilistic analysis of the observed lifetimes will become useful in identifying the specific fatigue crack initiating mechanisms similar to the work of Jha and co-workers [95].

(2) In line with the approach of using multiple repeats, a 3D volume of material should be serial sectioned from a fatigue crack initiation site. The acquisition of a digitized microstructural volume would be useful for a number of purposes. First, it would allow for a full interrogation of this volume and characterization of microstructural features such as distributions of grain size, misorientation, phase distribution and spatial descriptors such as two point statistics. A further step would be to employ this 3D volume in FEM simulations to study the effect of interactions between adjacent grains. Eventually, the distribution of microstructural features measured from this volume could be used to generate sythetic microstructures that would be appropriate for FEM simulations.

(3) TEM dislocation analysis could be conducted on foils extracted from the initiation region to determine how much slip activity is observed throughout the initiation volume. This analysis, while difficult and time consuming, would provide direct observations of the dislocation activity in the initiation site. Further, it would be possible to investigate the effect cyclic strain accumulation and impingement in adjacent grains.

(4) Complete fatigue experiments using coarse grain structures or leaner $\alpha + \beta$ alloys. With coarser microstructures, it would be easier to directly observe the formation of fatigue damage on the specimen surface in properly prepared specimens. Also, coarser microstructures would enhance the observable plasticity within individual grains and highlight the effects of the neighborhood and the interaction between adjacent grains.

(5) Investigate the effects of extreme microstructures. Since the variability in lifetimes is attributed to the presence of fatigue critical microstructural locations, it would be instructive to run experiments on specimens where the presence of extreme fatigue critical defects are a certainty and the distribution of these microstructural locations can be controlled. Since microtexture is observed drive fatigue crack initiation, it would be insightful to produce specimens in which it is known that extreme regions of microtexture (in terms of size and intensity) in which the texture is very strong and these regions are ubiquitously distributed throughout the microstructure to determine the effect of these extreme microstructures on the observed fatigue lifetime variability. Similar to the work of Riedler et al. [130], it is possible to create specific textures and gradients of texture within a given forging. These techniques could be employed to process material with known textures, and specimens could be extracted from this material and be machined into fatigue specimens.

(6) Strain mapping experiments would provide valuable insight into the process of fatigue damage accumulation that would allow modelers and alloy designers to identify the critical processes in the mechanism of fatigue damage accumulation. As described in the thesis, regions of microtexture are observed to initiate fatigue cracks, however the evidence

for the mechanism of damage accumulation within these regions is indirect. As this thesis has illustrates, it is possible to ascertain some of the important microstructural characteristics in the process of damage accumulation, however direct evidence from strain mapping experiments be valuable in informing these models of damage accumulation. Strain mapping experiments could be run in-situ or through interrupted testing. It would be necessary to run these tests at higher stresses to encourage fatigue crack initiation at the specimen surface. Additionally, by using an hourglass specimen design, it would be easier to monitor the evolution of fatigue damage owing to the reduced volume of interest. It might also be necessary to run these experiments on a coarse-grained microstructure to aid in the interpretation of results since the microstructure used in this study is very fine and not necessarily amenable to the resolution limits of most strain mapping techniques.

(7) One of the central ideas of this thesis is that there are a number of microstructural regions capable of initiating a fatigue crack and these regions are heterogeneously distributed throughout sample gage volumes. It seems reasonable that this concept, namely that fatigue critical regions are randomly distributed throughout fatigue specimens, could be scaled up to predict the failure probability of full scale components across an entire fleet. To assess the validity of this approach, experiments designed to investigate the volumetric effect could aid designers and practitioners in applying these concepts to a fleet of components. Therefore, testing of the hypothesis by investigating the volumetric effects in laboratory scale components would be a useful first step towards this goal.

# Appendix A

# PART DRAWING

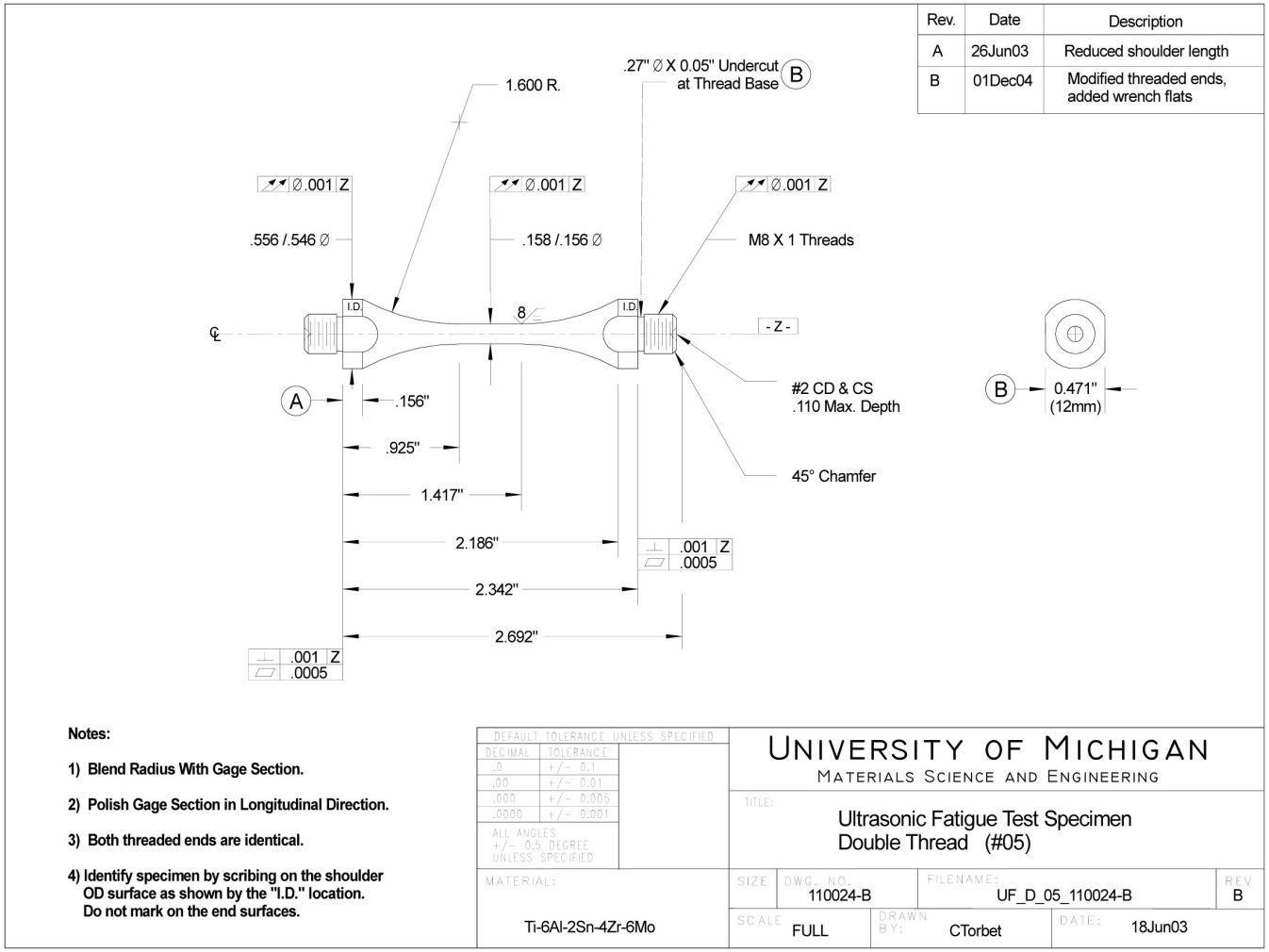


**Figure A.1:** The part drawing for the fatigue specimens used in this study.

# REFERENCES


[1] L. Christodolou and J.M. Larsen. Materials damage prognosis: A revolution in asset management. In J.M. Larsen, L. Christodoulou, J.R. Calcattera, M.L. Dent, M.M. Derriso, W.J. Hardman, J.W. Jones, and S.M. Russ, editors, *Materials Damage Prognosis*, pages 3–10. TMS(The Minerals, Metals, and Materials Society), 2005.

[2] C. Leyens and M. Peters. *Titanium and Titanium Alloys: Fundamentals and Applications*. Wiley-VCH, 2003.

[3] J.L. Murray. *Phase Diagrams of Binary Titanium Alloys*, page 12. ASM International, Metals Park, OH, 1987.

[4] E. W. Collings. *The Physical Metallurgy of Titanium Alloys*. American Society for Metals, Metals Park, OH, 1984.

[5] G. Lutjering. Influence of processing on microstructure and mechanical properties of alpha + beta titanium alloys. *Materials Science and Engineering A*, A243:32–45, 1998.

[6] N. E. Paton, J.C. Williams, and G.P. Rauscher. *The deformation of alpha-phase titanium*, volume 2, pages 1049–1069. Plenum Press, 1973.

[7] M. Peters, A. Gysler, and G. Lutjering. Influence of texture on fatigue properties of Ti–6Al–4V. *Metallurgical Transactions A*, 15A(8):1597–1605, 1984.

[8] J. A. Hall. Fatigue crack initiation in alpha-beta titanium alloys. *International Journal of Fatigue*, 19(1):S23–S37, 1997.

[9] W.J. Evans and M.R. Bache. Dwell and environmental aspects of fatigue in alpha/-beta titanium alloys. In R.R. Boyer, D. Eylon, and G. Lutjering, editors, *Fatigue Behavior of Titanium Alloys*. The Minerals, Metals, and Materials Society, 1999.

[10] E.E. Sackett, L. Germain, and M.R. Bache. Crystal plasticity, fatigue crack initiation and fatigue performance of advanced titanium alloys. *International Journal of Fatigue*, 29:2015–2021, 2007.

[11] J.C. Newman, E.P. Phillips, and M.H. Swain. Fatigue-life prediction methodology using small-crack theory. *International Journal of Fatigue*, 21:109–119, 1999.

[12] Jr. W.N. Sharpe. A 20 kilohertz optical strain gage. In J. E. Allison, J. W. Jones, J. Larsen, and R. O. Ritchie, editors, *Fourth International Conference on Very High Cycle Fatigue (VHCF-4)*, pages 341–346, Warrendale, PA, 2007. TMS(The Minerals, Metals, and Materials Society).

[13] S. K. Jha, J. Larsen, and A. Rosenberger. Source of variability in fatigue life of Ti-6Al-2Sn-4Zr-6Mo. Technical report, AFRL/RXLMN, 2003.

[14] Department of Defense. *Engine Structural Integrity Program (ENSIP) Handbook*, September 2004. http://engineering.wpafb.af.mil/corpusa/handbook/mh1783/mh1783.pdf.

[15] H. Kumar, C.L. Briant, and W.A. Curtin. Using microstructure reconstruction to model mechanical behavior in complex microstructures. *Mechanics of Materials*, 38:818–832, 2006.

[16] S. Suresh. *Fatigue of Materials*. Cambridge University Press, Cambridge, UK, 2001. ET: Second.

[17] G. Lutjering and J. C. Williams. *Titanium*. Springer-Verlag, Berlin, Heidelberg, 2003.

[18] Jr. M.J. Donachie. *Titanium and Titanium Alloys, Source Book*. American Society for Metals, Metals Park, OH, 1982.

[19] M.J. Blackburn and J.C. Williams. Strength, deformation modes and fracture in titanium-aluminum alloys. *ASM Transactions Quarterly*, 2:398–409, 1969.

[20] T. R. Bieler and S. L. Semiatin. The origins of heterogeneous deformation during primary hot working of Ti-6Al-4V. *International Journal of Plasticity (UK)*, 18(9):1165–1189, 2002.

[21] M.J. Blackburn and J.C. Williams. Metallurgical aspects of the stress corrosion cracking of titanium alloys. In D. Van Rooyen R.W. Staehle, A.J. Forty, editor, *Proceedings of the conference on the fundamental aspects of stress corrosion cracking*, 1969.

[22] F. Bridier, P. Villechaise, and J. Mendez. Analysis of the different slip systems activated by tension in a alpha/beta titanium alloy in relation with local crystallographic orientation. *Acta Materialia*, 53(3):555–567, 2005.

[23] J. C. Williams, R. G. Baggerly, and N. E. Paton. Deformation behavior of HCP Ti-Al alloy single crystals. *Metallurgical and Materials Transactions A*, 33A:837–850, 2002.

[24] S. Zaefferer. A study of active deformation systems in titanium alloys: dependence on alloy composition and correlation with deformation texture. *Materials Science and Engineering A*, A344:20–30, 2003.

[25] I.P. Jones and W. B. Hutchinson. Stress-state dependence of slip in Ti – 6Al – 4V and other H.C.P. metals. *Acta Metallurgica*, Vol.29:951–968, 1981.

[26] M.F. Savage, J. Tatalovich, M. Zupan, K.J. Hemker, and M.J. Mills. Deformation mechanisms and microtensile behavior of single colony Ti-6242Si. *Materials Science and Engineering A*, 319-321:398–403, 2001.

[27] S. Suri, G.B. Viswanathan, T. Neeraj, D. Hou, and M.J. Mills. Room temperature deformation and mechanisms of slip transmission in oriented single-colony crystals of an alpha / beta titanium alloy. *Acta Materialia*, 47:1019–1034, 1999.

[28] F.S. Lin, Jr. E.A. Starke, S.B. Chakrabortty, and A. Gysler. The effect of microstructure on the deformation modes and mechanical properties of Ti-6Al-2Nb-1Ta-0.8Mo: Part I. Widmanstatten structures. *Metallurgical Transactions A*, 15A:1229–1246, 1984.

[29] J.C. Williams and M.J. Blackburn. The identification of a non-basal slip vector in titanium and titanium aluminum alloys. *Phys. Status Solidi.*, 25:K1–K3, 1968.

[30] W.R. Tyson. Basal and prismatic slip in h.c.p. crystals. *Acta Metallurgica*, 15:574–577, 1967.

[31] W.G. Burgers. On the process of transition of the cubic-body-centered modification into the hexagonal-close-packed modification of zirconium. *Physica*, 1:561–586, 1934.

[32] N. Stanford and P.S. Bate. Crystallographic variant selection in Ti-6Al-4V. *Acta Materialia*, 52:5215–5224, 2004.

[33] D. Bhattacharyya, G.B. Viswanathan, R. Denkenberger, D. Furrer, and H.L. Fraser. The role of crystallographic and geometrical relationships between alpha and beta phases in an alpha/beta titanium alloy. *Acta Materialia*, 51:4679–4691, 2003.

[34] M.J. Mills, D.H. Hou, S. Suri, and G.B. Viswanathan. Orientation relationship and structure of alpha/beta interfaces in conventional titanium alloys. In R.C. Pond, W.A.T. Clark, A.H. King, and D.B. Williams, editors, *Boundaries and Interfaces in Materials*, page 295. TMS, Warrendale, PA,, 1998.

[35] T. Furuhara, T. Ogawa, and T. Maki. Surface relief effect and atomic site correspondence in the grain boundary alpha precipitation in a beta Ti-Cr alloy. *Scripta Materialia*, 34:381–386, 1996.

[36] A. P. Woodfield, M. D. Gorman, R. R. Corderman, J. A. Sutliff, and B. Yamrom. Effect of microstructure on dwell fatigue behavior of Ti-6242. In *Titanium '95. Vol. II*, pages 1116–1123, Birmingham; UK, 22-26 Oct. 1995 1996. Institute of Materials.

[37] G. Halford. Cumulative fatigue damage modeling-crack nucleation and early growth. *International Journal of Fatigue*, 19:s253–s260, 1997.

[38] H. Margolin, J. C. Williams, J. C. Chesnutt, and G. Luetjering. A review of the fracture and fatigue behavior of titanium alloys. *Titanium '80*, page Science and Technology, Vol. 1; Kyoto; Japan; 19-22 May 1980. pp. 169-216. 1980.

[39] D.K. Benson, J.C. Grosskreutz, and G.G. Shaw. Mechanisms of fatigue in mill-annealed Ti-6Al-4V at room temperature and 600 . *Metallurgical Transactions A*, 3, 1972.

[40] H. Mughrabi. On the life-controlling microstructural fatigue mechanisms in ductile metals and alloys in the gigacycle regime. *Fatigue and Fracture of Engineering Materials and Structures*, 22:633–641, 1999.

[41] Y. Murakami, N.N. Yokoyama, and J. Nagata. Mechanism of fatigue failure in ultralong life regime. *Fatigue and Fracture of Engineering Materials and Structures*, 25(8-9):735–746, 09/24 2002.

[42] D. Eylon and C.M. Pierce. Effect of microstructure on notch fatigue properties of Ti-6Al-4V. *Metallurgical Transactions*, 7A:111, 1976.

[43] M.R. Bache, W.J. Evans, B. Suddell, and F.R.M. Herrouin. The effects of texture in titanium alloys for engineering components under fatigue. *International Journal of Fatigue*, 23:S153–S159, 2001.

[44] D. Eylon. Faceted fracture in beta annealed titanium alloys. *Metallurgical Transactions A*, 10A:311–317, 1979.

[45] A.L. Helbert, X.M. Feaugas, and M. Clavel. Experimental study of damage kinetics in alpha / beta titanium alloys. In *Advances in Fracture Research. ICF9Failure Analysis, Remaining Life Assessment, Life Extension and Repair*, pages 179–187, 1997.

[46] D. Rugg, M. Dixon, and F.P.E. Dunne. Effective structural unit size in titanium alloys. *Journal of Strain Analysis*, 42:269–279, 2007.

[47] G.J. Baxter, W.M. Rainforth, and L. Grabowski. TEM observations of fatigue damage accumulation at the surface of the near-alpha titanium alloy IMI834. *Acta Metallurgica*, 44(9):3453–3463, 1996.

[48] D. L. Davidson and D. Eylon. Titanium alloy fatigue fracture facet investigation by selected area electron channeling. *Metallurgical Transactions*, 11A:837–843, 1980.

[49] D. Neal and P. Blenkinsop. Internal fatigue origins in alpha-beta titanium alloys. *Acta Metallurgica*, 24:59–63, 1976.

[50] A. Beranger, X. Feaugas, and M. Clavel. Low cycle fatigue behavior of an alpha + beta titanium alloy: Ti6246. *Materials Science and Engineering A*, 172:31–41, 1993.

[51] F. Bridier, P. Villechaise, and J. Mendez. Analysis of slip and crack initiation processes activated by fatigue in a alpha/beta titanium alloy in relation with local crystallographic orientation. *Fatigue 2006 (electronic proceedings)*, 2006.

[52] O. Umezawa, K. Nagai, and K. Ishikawa. Transmission electron microscopy study of high cycle fatigue deformation in Ti-5Al-2.5-Sn extra-low interstitial alloy at cryogenic temperatures. *Materials Science and Engineering A*, A129:223–227, 1990.

[53] K. LeBiavant, S. Pommier, and C. Prioul. Local texture and fatigue crack initiation in a Ti-6Al-4V titanium alloy. *Fatigue and Fracture of Engineering Materials and Structures*, 25:527–545, 2002.

[54] V. Sinha, J. E. Spowart, M. J. Mills, and J. C. Williams. Observations on the faceted initiation site in the dwell-fatigue tested Ti-6242 alloy: Crystallographic orientation and size effects. *Metallurgical and Materials Transactions A*, 37A, pp. 1507-1518. May 2006.

[55] Y. Saleh and H. Margolin. Low cycle fatigue of Ti-Mn alloys: microstructural aspects of fatigue crack growth. *Metallurgical Transactions*, 14A:1481–1486, 1983.

[56] Y. Mahajan and H. Margolin. Low cycle fatigue behavior of Ti-6Al-2Sn-4Zr-6Mo: Part 1. the role of microstructure in low cycle crack nucleation and early crack growth. *Metallurgical Transactions A*, 13A:257–268, 1982.

[57] G. Jago, J. Bechet, and C. Bathias. Microstructures/properties relationships in Ti-6.2.4.6 alloy: A microstructural approach to the fatigue damage. In *Titanium '95: Science and Technology*, pages 1203–1210, 1996.

[58] A. Funkenbusch and L. Coffin. Low-cycle fatigue crack nucleation and early growth in Ti-17. *Metallurgical Transactions A*, 9A:1159–1167, 1978.

[59] T. Akahori, M. Niinomi, K. Fukunaga, and I. Inagaki. Effects of microstructure on the short fatigue crack initiation and propagation characteristics of biomedical alpha/beta titanium alloys. *Metallurgical and Materials Transactions A*, 31A(8):1949–1958, 2000.

[60] C. Sauer and G. Lutjering. Influence of alpha layers at beta grain boundaries on mechnaical properties of Ti-alloys. *Materials Science and Engineering A*, A319-321:393–397, 2001.

[61] C.A. Stubbington and A.W. Bowen. Improvements in the fatigue strength of Ti-6Al-4V through microstructure control. *Journal of Materials Science*, 9:941–947, 1974.

[62] J. H. Zuo, Z. G. Wang, and E. H. Han. Effect of microstructure on ultra-high cycle fatigue behavior of Ti-6Al-4V. *Materials Science and Engineering A.*, Vol.473:147–152, 2008.

[63] D. L. Davidson, R. G. Tryon, M. Oja, R. Matthews, and K. S. Ravi Chandran. Fatigue crack initiation in Waspaloy at 20 deg c. *Metallurgical and Materials Transactions A*, 38:2214–2225, 2007.

[64] J. A. Ruppen, D. Eylon, and A. J. McEvily. Subsurface fatigue crack initiation of beta-annealed Ti-6Al-4V. *Metallurgical Transactions A*, 11A:1072–1075, 1980.

[65] K. S. Ravichandran and S. K. Jha. Duality of the S-N fatigue curve caused by competing failure modes in a titanium alloy and the role of poisson defect statistics. *Acta Materialia*, 53:1867, 2005.

[66] J. Gilbert and H. Piehler. On the nature and crystallographic orientation of subsurface cracks in high cycle fatigue of Ti-6Al-4V. *Metallurgical Transactions A*, 24A:669–680, 1993.

[67] V. Sinha, M. J. Mills, and J. C. Williams. Crystallography of fracture facets in a near-alpha titanium alloy. *Metallurgical and Materials Transactions A*, 37A:2015–2026, 2006.

[68] U. Krupp, W. Floer, J. Lei, Y. Hu, H. Christ, A. Schick, and C. Fritzen. Mechanisms of short-fatigue-crack initiation and propagation in a beta-Ti alloy. *Philosophical Magazine A*, 82(17/18):3321–3332, 2002.

[69] X. Feaugas and M. Clavel. Cyclic deformation behavior of an alpha / beta titanium alloy. I. micromechanisms of plasticity under various loading paths. *Acta Materialia*, 45(7):2685–2701, 1997.

[70] A. N. Stroh. A theory of the fracture of metals. *Advances in Physics*, 6(24):418–465, 1957.

[71] W. Evans. Optimising mechanical properties in alpha + beta titanium alloys. *Materials Science and Engineering A*, A243:89–96, 1998.

[72] S. Suresh and R.O. Ritchie. Propagation of short fatigue cracks. *International Materials Reviews*, 29:445–476, 1984.

[73] S. Pearson. Initiation of fatigue cracks in commercial aluminum alloys and the subsequent propagation of very short cracks. *Engineering Fracture Mechanics*, 7:235–247, 1975.

[74] J. Lankford. The growth of small fatigue cracks in 7075-T6 aluminum. *Fatigue of Engineering Materials and Structures*, 5:233–248, 1982.

[75] K.S. Chan and J. Lankford. The role of microstructural dissimilitude in fatigue and fracture of small cracks. *Acta Metallurgica*, 36:193–206, 1988.

[76] I. Bantounas, T.C. Lindley, D. Rugg, and D. Dye. Effect of microtexture on fatigue cracking in Ti-6Al-4V. *Acta Materialia*, 55:5655–5665, 2007.

[77] A.W. Bowen. The influence of crystallographic orientation on fatigue crack growth in strongly textured Ti-6Al-4V. *Acta Metallurgica*, 23:1401–1409, 1975.

[78] G.T. Gray, G. Lutjering, and J.C. Williams. The influence of oxygen on the structure, fracture, and fatigue crack propagation behavior of Ti–8.6 wt.% Al. *Metallurgical Transactions A*, 21A:95–105, 1990.

[79] O. Jin and S. Mall. Effects of microstructure on short crack growth behavior of Ti-6Al-2Sn-4Zr-2Mo-0.1Si alloy. *Materials Science and Engineering A*, 359(1-2):356–367, 2003.

[80] C. Mercer, S. Shademan, and W.O. Soboyejo. An investigation of the micromechanisms of fatigue crack growth in structural gas turbine engine alloys. *Journal of Materials Science*, 38:291–305, 2003.

[81] K. Nakajima, K. Terao, and T. Miyata. The effect of microstructure on fatigue crack propagation of $\alpha + \beta$ titanium alloys. *Materials Science and Engineering A*, A243:176–181, 1998.

[82] G. Schroeder, J. Albrecht, and G. Lutjering. Fatigue crack propagation in titanium alloys with lamellar and bi-lamellar microstructures. *Materials Science and Engineering A*, A319-321:602–606, 2001.

[83] S. Shademan, V. Sinha, A. B. O. Soboyejo, and W. O. Soboyejo. An investigation of the effects of microstructure and stress ratio on fatigue crack growth in Ti-6Al-4V with colony alpha/beta microstructures. *Mechanics of Materials*, 36(1-2):161–175, 2004.

[84] V. Sinha and W.O. Soboyejo. Invesitgation of the effects of colony microstructure on fatigue crack growth in Ti-6Al-4V. *Materials Science and Engineering*, A319-321:607–612, 2001.

[85] D.L. Davidson. Damage mechanisms in high cycle fatigue. Technical report, AFOSR Final Report, Project 06-8243, Southwest Research Institute, 1998.

[86] J. Hines and G. Lutjering. Propagation of microcracks at stress amplitudes below the conventional fatigue limit in Ti-6Al-4V. *Fatigue and Fracture of Engineering Materials and Structures*, 22:657–665, 1999.

[87] R. K. Nalla, B. L. Boyce, J. P. Campbell, J. O. Peters, and R. O. Ritchie. Influence of microstructure on high-cycle fatigue of Ti-6Al-4V: bimodal vs. lamellar structures. *Metallurgical and Materials Transactions A (USA).*, 33A:899–918, 2002.

[88] B.L. Boyce and R.O. Ritchie. Effect of load ratio and maximum stress intensity on the fatigue threshold in Ti-6Al-4V. *Engineering Fracture Mechanics*, 68:129–147, 2001.

[89] Ritchie, D. L. Davidson, B.L. Boyce, J.P. Campbell, and O. Roder. High-cycle fatigue of Ti-6Al-4V. *Fatigue and Fracture of Engineering Materials and Structures*, 22(7):621–631, 1999.

[90] S. Suresh and R.O. Ritchie. A geometric model for fatigue crack closure induced by fracture surface roughness. *Metallugical Transactions*, 13A:1627–1631, 1982.

[91] Jr. C.C. Engler-Pinto, Sr. R.J. Frisch, J. Lasecki, H. Mayer, and J. E. Allison. Effect of frequency and environment on high cycle fatigue of cast aluminum alloys. In *VCHF-4*, pages 421–427, Warrendale, PA, 2007. TMS.

[92] C. Bathias. There is no infinite fatigue life in metallic materials. *Fatigue and Fracture of Engineering Materials and Structures*, 22(7):559–565, 1999.

[93] Nishijima and Kanazawa. Stepwise S-N curve and fish-eye failure in gigacycle fatigue. *Fatigue and Fracture of Engineering Materials and Structures*, 22(7):601–607, 1999.

[94] P. Lukas and L. Kunz. Specific features of high-cycle and ultra-high-cycle fatigue. *Fatigue and Fracture of Engineering Materials and Structures*, 25(8-9):747–753, 2002.

[95] Y. Murakami, T. Nomoto, and T. Ueda. Factors influencing the mechanism of superlong fatigue failure in steels. *Fatigue and Fracture of Engineering Materials and Structures*, 22:581–590, 1999.

[96] G.T. Cashman. A mathematical model for competing failure modes in strain cycle fatigue. *Journal of Engineering Materials and Technology*, 129:293–303, 2007.

[97] S. K. Jha and J. M. Larsen. Random heterogeneity scales and probabilistic descriptions of the long lifetime regime of fatigue. In J. E. Allison, J. W. Jones, J. M. Larsen, and R. O. Ritchie, editors, *Fourth International Conference on Very High Cycle Fatigue(VHCF-4)*, Warrendale, PA, 2007. TMS.

[98] H. Mughrabi. On 'multi-stage' fatigue life diagrams and the relevant life-controlling mechanisms in ultrahigh-cycle fatigue. *Fatigue and Fracture of Engineering Materials and Structures*, 25(8-9):755–764, 2002.

[99] D. Bhattacharyya. *The Development of Textures and Microstructures in alpha/beta titanium alloys*. PhD thesis, The Ohio State University, 2004.

[100] R.K. Nalla, J.P. Campbell, and R.O. Ritchie. Mixed-mode, high-cycle fatigue-crack growth thresholds in Ti-6Al-4V: Role of small cracks. *International Journal of Fatigue*, 24(10):1047–1062, 2002.

[101] L. Willertz. Ultrasonic fatigue. *International Materials Reviews*, 25(2):65–78, 1980.

[102] H. Mayer and C. Laird. Influence of cyclic frequency on the strain localization and cyclic deformation in fatigue. *Materials Science and Engineering A*, A187:23–35, 1994.

[103] L.D. Roth, L.E. Willertz, and T.R. Leax. On the fatigue of copper up to ultrasonic frequencies. In *Proceedings of the First International Conference on Fatigue and Corrosion Fatigue up to Ultrasonic Frequencies*, pages 265–282, 1981.

[104] R.J. Morrissey, D.L. McDowell, and T. Nicholas. Frequency and stress ratio effects in high cycle fatigue of Ti-6Al-4V. *International Journal of Fatigue*, 21:679–685, 1999.

[105] J. Miao, T. M. Pollock, and J. W. Jones. Very high cycle fatigue behavior of nickel-based superalloy René 88DT at 593degC. In *Fourth International Conference on Very High Cycle Fatigue (VHCF-4)*, 2007.

[106] M. Papakyriacou, H. Mayer, U. Fuchs, S. E. Stanzl-Tschegg, and R. R. P. Wei. Influence of atmospheric moisture on slow fatigue crack growth at ultrasonic frequency in aluminium and magnesium alloys. *Fatigue and Fracture of Engineering Materials and Structures*, 25(8-9):795–804, 2002.

[107] B. Holper, H. Mayer, A.K. Vasudevan, and S.E. Stanzl-Tschegg. Near threshold fatigue crack growth in aluminium alloys at low and ultrasonic frequency: Influences of specimen thickness, strain rate, slip behaviour and air humidity. *International Journal of Fatigue*, 25:397–411, 2003.

[108] X. Zhu. *Ultrasonic fatigue of E319 cast aluminum alloy in the long lifetime regime*. PhD thesis, University of Michigan, 2007.

[109] B. Holper, H. Mayer, A.K. Vasudevan, and S.E. Stanzl-Tschegg. Near threshold fatigue crack growth at positive load ratio in aluminium alloys at low and ultrasonic frequency: influences of strain rate, slip behaviour and air humidity. *International Journal of Fatigue*, 26:27–38, 2004.

[110] R.J.H. Wanhill. Environment and frequency effects during fatigue crack propagation in Ti-2.5 Cu (IMI 230) sheet at room temperature. *Corrosion-NACE*, 30:28–35, 1974.

[111] S. Lesterlin, C. Sarrazin-Baudoux, and J. Petit. Temperature-environment interactions on fatigue behavior in Ti-6246 alloy. In *Titanium '95*, 1995.

[112] C. Sarrazin-Baudoux, Y. Chabanne, and J. Petit. Influence of environment and of mean stress on fatigue crack growth at near threshold stress intensities on a Ti-6246 alloy at room temperature and 500°C. *Scripta Materialia*, 40:451–457, British Columbia; Canada; 16-21 May 1999. pp. 346-351. 1999.

[113] C. Sarrazin-Baudoux and J. Petit. Environmental effects on near-threshold fatigue crack propagation on a Ti-6246 alloys at 500°C. In L. Remy and J. Petit, editors, *Temperature-Fatigue Interactions*, pages 227–236. Elsevier, 2002.

[114] M. Bache. A review of dwell sensitive fatigue in titanium alloys: the role microstrcuture, texture, and operating conditions. *International Journal of Fatigue*, 25:1079–1087, 2003.

[115] M. Bache, H. Davies, and W. J. Evans. A model for fatigue crack initiation in titanium alloys. In *Titanium '95: Science and Technology*, 1995.

[116] A. Shyam, C. Torbet, S. K. Jha, J. Larsen, M. Caton, C. Szczepanski, T. M. Pollock, and J. W. Jones. Development of ultrasonic fatigue for rapid, high temperature fatigue studies in turbine engines. In K. Green, T. M. Pollock, H. Harada, T. Howson, R. Reed, J. Schirra, and S. Walston, editors, *Superalloys 2004*, pages 259–268. TMS, 2004.

[117] J. M. Larsen, J. R. Jira, and K. S. Ravichandran. Measurement of small cracks by photomicroscopy: Experiments and analysis. In *STP 1149*, pages 57–80, Philadelphia, Pennsylvania, Nov. 1990 1992. ASTM.

[118] J. Newman and I. Raju. An emprirical stress-intensity factor equation for the surface crack. *Engineering Fracture Mechanics*, 15:185–192, 1981.

[119] Q. Feng, Y. Picard, H. Liu, S. Yalisove, G. Mourou, and T. M. Pollock. Femtosecond laser micromachining of a single-crystal superalloy. *Scripta Materialia*, 53:511–516, 2005.

[120] J. Z. Yi, C. J. Torbet, Q. Feng, T. M. Pollock, and J. W. Jones. Ultrasonic fatigue of a single crystal ni-base superalloy at 1000 deg c. *Materials Science and Engineering A*, 443(1-2):142–149, 2007.

[121] M. G. Glavicic, P. A. Kobryn, T. R. Bieler, and S. L. Semiatin. An automated method to determine the orientation of the high-temperature beta phase from measured ebsd data for the low-temperature alpha-phase in Ti-6Al-4V. *Materials Science and Engineering A*, 351, pp. 258-264. 25 June 2003.

[122] M. Humbert, N. Gey, J. Muller, and C. Esling. Determination of a mean orientation from a cloud of orientations. application to electron back-scattering pattern measurements. *Journal of Applied Crystallography*, 29:662–666, 1996.

[123] V. Randle and O. Engler. *Introduction to Texture Analysis: Macrotexture, Microtexture and Orientation Mapping*. CRC, 2000.

[124] J. Mendez, S. Mailly, and P. Villechaise. In J. Petit L. Remy, editor, *Temperature-Fatigue Interactions*, volume ESIS TTP 29, pages 95–102. Elsevier, 2002.

[125] G. Cashman and J. Gallagher. A statistical methodology for the preparation of a competing modes fatigue design curves. *ASME*, 2004.

[126] Y. Murakami. *Stress Intensity Factors Handbook*. Pergamon, Oxford : New York, 1987.

[127] W. J. Evans and M. R. Bache. Dwell-sensitive fatigue under biaxial loads in the near-alpha titanium alloy IMI685. *International Journal of Fatigue*, 16(7):443–452, 1994.

[128] N. Biery, M. DeGraef, and T. M. Pollock. Influence of microstructure and strain distribution on failure properties in intermetallic TiAl-based alloys. *Materials Science and Engineering A*, A319-321:613–617, 2001.

[129] S.K. Jha, M.J. Caton, and J.M. Larsen. A new paradigm of fatigue variability behavior and implications for life prediction. *Materials Science and Engineering A*, 468-470:23–32, 2007.

[130] M. Riedler, M. Stockinger, M. Stoschka, B. Oberwinkler, and W. Tan. Linking microstructure and fatigue of forged Ti-6Al-4V aerospace parts. In *LCF6*, 2008.